High Resolution Source Reconstruction of Gravitationally Lensed High Redshift Galaxies

Soniya Sharma

A thesis submitted for the degree of

Doctor of Philosophy

of the Australian National University

Research School of Astronomy & Astrophysics

Submitted 1st September 2020

To my life-coach, my Mom…

Declaration

I hereby declare that the work in this thesis is that of the candidate alone, except where indicated below or in the text of the thesis. The work was undertaken between February 2015 and August 2019 at the Australian National University (ANU), Canberra. It has not been submitted in whole or in part for any other degree at this or any other university.

This thesis has been submitted as a standard thesis in accordance with the relevant ANU policies. The chapters that appear in this thesis are modifed forms of three papers. I am the first author on all these papers. The thesis has been an excellent preparation for post-doctoral research, as I have been involved in the full scientific process from planning and undertaking observations to sophisticated modelling and producing peer-reviewed publications. Concretely, my contribution to the thesis can be outlined as follows :

- Prepared and submitted observing proposal for the NIRC2 instrument on the Keck telescope to obtain high resolution imaging data for our source galaxy.
- Carried out and analyzed the observations of NIRC2 by developing my own data reduction routines in IDL.
- Contributed towards the data reduction of IFU observations of the source galaxy.
- Prepared sophisticated mass model for the lensing galaxy group using the lensing modelling software, LENSTOOL.
- Determined the best way to combine multiple observations in the source plane using a unique forward source modelling approach.
- Modified the source code of LENSTOOL to include an automated source reconstruction algorithm.
- Ran simulations to test the algorithm and analyzed their output to quantify the performance of the algorithm.
- Carried out the science case application of the algorithm on the same lensed system and compared the results to traditional methods.
- Interpreted the results and led the efforts in the preparation of papers.

The three papers that form a part of this thesis are :

Chapter 2 & Chapter 3: Sharma, S., Richard, J., Yuan, T., Gupta, A., Kewley, L., Patrício, V., Leethochawalit, N., Jones, T. ~ A., 2018, "High-resolution spatial analysis of a z ~ 2 lensed galaxy using adaptive coadded source-plane reconstruction", MNRAS, 481, 1427

Chapter 4: Sharma, S., Richard, J., Yuan, T., Gupta, A., Kewley, L., Patrício, V., Leethochawalit, N., Jones, T. ~ A., "Pixelated source plane reconstruction in Lenstool", MNRAS, in preparation.

Chapter 5: Sharma, S., Richard, J., Yuan, T., Kewley, L., "Resolving star-forming clumps in a z ~ 2 lensed galaxy: a pixelated Bayesian approach", MNRAS, in preparation.

Soniya Sharma

1st September 2020

Acknowledgments

Foremost, I would like to express my sincere gratitude to my supervisor, Prof. Lisa Kewley, for her continuous support, motivation and encouragement during my PhD, for instilling positivity every time we had a discussion, for making it possible for me to work on a topic that was interesting and challenging in its own ways, and for providing funding for my frequent France visits to gain the needed expertise in lens modelling. Needless to mention, your writing retreats have been extremely crucial in helping me improve my scientific writing and discover my love for writing. A very special gratitude also goes to Dr. Tiantian Yuan for her constant guidance during the thesis and reminding me of the big picture where my thesis was relevant and impactful, whenever I felt low. Your constructive comments, suggestions and critiquing have helped me prepare myself for the next stage in my career.

This thesis would not have been possible without the expertise and insights of my advisor, Prof. Johan Richard. Thank you for your patience with replying to my emails and finding out time for skype meetings from your busy schedule. My visits to CRAL have been the most productive time of my PhD. Talking to other people in your group always gave me the confidence and enthusiasm about my research. I would like to thank Dr. Brent Groves, who was always up for a pleasant chat, be it about research or otherwise. Thanks are also due to all the members of Gears3D for making my stay at Stromlo a great one. I am grateful to all my collaborators Dr. Vera Patrício, Dr. Nicha Leethochawalit and Dr. Tucker Jones for your invaluable inputs.

I'd like to thank my family - Mom, Dad and my sister for their unfailing support throughout the PhD. A special mention to my mom- you have always been encouraging, keen to know more about my research and how I was proceeding. In times of despair, you always had the magic solution for every problem. I owe a thanks to a very special person, my husband, Deepak, for his continued love, support and understanding during my pursuit of the PhD degree. My PhD journey would have been quite stressful without my Canberra friends: Ayan, Amit, Jane, Anshu, Anneshwa, Rajshekhar and Kartik. I will miss chatting, cooking, hiking and playing board games with all of you. And finally, but most importantly, I would like to thank my friends in India : Swagat, Suryans and Prasun for supporting me along the way despite being miles away physically.

Abstract

Spatially resolved studies of high redshift galaxies, particularly in the peak of galaxy formation epoch $1 \lesssim z \lesssim 3$, hold the key for understanding the physics of galaxy formation and evolution. Natural magnification provided by gravitational lensing provides a rare opportunity to obtain magnified views of these galaxies at an enhanced spatial resolution. However, the application of lensing in studying high-redshift galaxies has not reached its full potential with traditional source reconstruction approaches because of an under-appreciated problem: source-plane point spread function (PSF).

In this thesis, I present a forward modelling approach based on a robust lens model to deconvolve the effects of source-plane PSF and achieve a resolution of ~170 pc in the source plane of a $z \sim 2$ lensed galaxy, which would have been otherwise unachievable through traditional image inversion methods. The forward modelling technique takes full advantage of the lensing amplification by assimilating all the available information from different multiple images of the lensed system. This is crucial in order to confidently analyse the dynamics of the lensed target especially in the low signal to noise (SNR) regions of the image plane. The final merged reconstruction allows a significant improvement (by a factor > 5) in SNR of emission line maps in the source plane. Moreover, different components are detected in the velocity profile that are not seen in previous studies of this object, plausibly suggesting an ongoing merger in this system.

I extend the idea of the forward approach to develop an automated source reconstruction algorithm integrated with a popular lens modelling software, LENSTOOL. This technique utilizes constraints from the extended surface-brightness profile of the lensed source for a given lens model and reconstructs its intrinsic distribution on a pixelated grid using a bayesian Monte-Carlo Markov chain optimization algorithm in LENSTOOL. The pixelated source modelling algorithm is validated through the demonstration of different test simulations. Results from my forward approach are compared against the corresponding traditional reconstructions to measure the effects of PSF smearing on physical sizes of star-forming clumps at high redshifts.

As a first case study, I apply the algorithm to reconstruct the morphology of the same lensed system at $z \sim 2$. I obtain a remarkable improvement over traditional ray-tracing, as the technique recovers low surface brightness clumps in the source morphology because of PSF deconvolution in the source-plane. The pixelated approach is sensitive to clump sizes down to 100 pc and allows an improvement in the SNR by almost a factor of ten compared with the traditional ray-tracing approach, especially in the most magnified regions of the source. The results from this case study further motivate the use of pixelized forward modelling technique in future detailed studies of physical properties of lensed galaxies at high resolution using instruments on James Webb Space Telescope (JWST).

Contents

List of Figures ix
List of Tables xv

1 Introduction 1

1.1 Spatially Resolved Observations of Galaxies 2
1.2 Strong Gravitational Lenses as Cosmic Telescopes 3
1.2.1 Lensing Basics 3
1.2.2 Peering into the high-z Universe: Cluster-scale Lensing 5
1.3 Lens Modelling- *Lenstool* 9
1.4 Motivation 11
1.5 Thesis Outline 13

2 Pilot study of $z \sim 2$ lensed galaxy: Lens Model 15

2.1 Introduction 15
2.2 Observations and Data Reduction 16
2.2.1 Previous Data 16
2.2.2 New Data 16
2.3 Lens Modelling Methodology 19
2.4 Conclusions 22

3 Pilot Study of $z \sim 2$ lensed galaxy: Source Reconstruction 23

3.1 Introduction 23
3.2 Traditional Ray Tracing Approach: Direct Image to Source Plane Mapping . 25
3.3 Forward modeling Approach: Source to Image Plane Mapping 25
3.4 Source Properties 28

3.4.1 Source Plane Morphology . . . 28
3.4.2 Kinematics . . . 29
3.4.3 Rest-Frame Emission Line Ratios . . . 30
3.4.4 Spectral Energy Distribution fitting, Stellar Mass and Star formation Rate . . . 32
3.5 Conclusions . . . 32

4 The Pixelated Forward Source Modelling in LENSTOOL 35
4.1 Introduction . . . 35
4.2 Basic Formalism . . . 36
4.2.1 Setting up grids using transformation matrix . . . 36
4.2.2 Bayesian optimization . . . 37
4.3 Implementation in LENSTOOL . . . 39
4.4 Simulations . . . 40
4.4.1 One Gaussian Tests . . . 41
4.4.2 Two Gaussian Tests . . . 42
4.5 Simulation Results . . . 42
4.5.1 Effect of PSF . . . 42
4.5.2 Effect of SNR . . . 44
4.6 Conclusions . . . 48

5 Testing the Pixelated Approach - Resolving star-forming clumps in cswa128 49
5.1 Introduction . . . 49
5.2 Source Reconstruction . . . 50
5.2.1 Hα emission line fitting . . . 51
5.2.2 Kinematics . . . 52
5.3 Clump Measurements . . . 53
5.4 Discussion . . . 54
5.5 Conclusions . . . 55

6 Conclusions 57
6.1 Future Work . . . 58
6.1.1 Theoretical Advances . . . 58
6.1.2 Observational Prospects . . . 59

Appendices 69

Appendix A Source reconstruction through *cleanlens* task in LENSTOOL **71**

Appendix B Simulation Results **79**

List of Figures

1.1 Lensing Geometry. 4
1.2 Examples of lensed high-z arcs as observed by HST. 5
1.3 Compiled metallicity gradient measurements from literature. 6
1.4 Number distribution of star-forming regions in HST B- band image of local galaxy - NGC628. 7
1.5 Star-formation - radius relation in the individual clumps in the lensed galaxy SGAS J111020.0+645950.8 at z = 2.481. 8
1.6 Overview of lens model and multiple-image systems for Abell2744. 10

2.1 SDSS color composite image and NIRC2 observations of cswa128, lensed galaxy behind a galaxy group at z = 0.214. 16
2.2 Examples of 1D spectra and Hα 2D intensity map from emission line fitting of new OSIRIS spectroscopic data on multiple image a2 of the lensed arc. . . 18
2.3 Our lens model of CSWA128 based on NIRC2 data. 20
2.4 Lens model of CSWA128 based on SDSS imaging data. 21

3.1 An example of source reconstructed stellar continuum from NIRC2 observations and Hα brightness distribution from IFU data for each of the magnified images (a1, a2) of the lensed arc and their rendition into a single frame to highlight the disadvantages of source-plane PSF. 24
3.2 Comparing the 2D Hα intensity and SNR maps using (a) our forward coadded source-reconstruction with (b) the traditional ray tracing approach of multiple image a2 of cswa128. 27
3.3 Derived source-plane 2D rotational velocity map and integrated 1D spectra of different source-plane regions using our forward-adaptive co-adding technique. 28
3.4 Derived source plane 2D maps for blue component of emission. 30

3.5 Derived source plane 2D maps for red component of emission. 31

3.6 Derived 2D source-plane [N II]/Hα and metallicity maps for blue and red components of emission. Contours are the same as Figure 3.1. 33

4.1 Illustration of the pixelated algorithm using an example of a Gaussian profile in the source plane. 39

4.2 Double Gaussian source profiles used for testing the pixelated algorithm. . 41

4.3 Pixelated vs direct reconstruction for a double Gaussian source profile with σ's equal to 1.25 and 1.5 $\times$ pixel size in the source plane. 43

4.4 Source-plane RMS error as a function of RBF widths for overlapping double Gaussian source models for a fixed peak SNR of 20 in the image plane. . . . 44

4.5 Source-plane RMS error as a function of RBF widths for overlapping double Gaussian source models for a fixed ratio of PSF FWHM / Image plane sampling = 2.0. 45

4.6 Source-plane RMS error computed on overlapping double Gaussian source profiles reconstructed with pixelated modelling technique as a function of the ratio of PSF FWHM to image plane sampling at the "best" RBF size. . . . 46

4.7 Source-plane RMS error computed on overlapping double Gaussian source profiles reconstructed with direct ray-tracing as a function of the ratio of PSF FWHM to image plane sampling. 47

5.1 (a) Reconstruction of three arbitrary wavelength channels around the Hα emission line using the pixelated (upper panels) and direct (lower panels) methods of source reconstruction from the a1 datacube. Different values of **n** at the top of the panels represent the channel numbers in the corresponding IFU data cubes. The yellow curve shown in the middle panel represents caustics (regions of high magnification in the source plane) using the best fit lens model. The blue ellipses show the FWHM of the effective source plane PSF's at two different locations in the source plane. (b) Derived 2D source plane Hα intensity maps in units of 10^{-16} erg s^{-1} cm^{-2} arcsec^{-2} using the pixelated and direct method of source reconstruction for the a1 lensed image. The cyan ellipses refer to the clumps detected by the ASTRODENDRO in the pixelated reconstruction of the a1 lensed image as described in Section 5.3. (c) and (d) same as (a) and (b) respectively, but for the lensed image a2. . . . 51

5.2 Comparison of derived source-plane 2D rotational velocity maps for a1 and a2 lensed images of cswa128 using the traditional and pixelated methods of source reconstruction in LENSTOOL. Using the pixelated approach, we can easily recover the kinematics of this system in the extended regions of low Hα brightness emission, that had been missed by the direct reconstruction. 52

5.3 Clump SNR and sizes: pixelated vs direct reconstruction. **Left:** SNR comparison for all the clumps detected in the source-plane reconstruction of Hα maps as labelled in Figure 5.1b. SNR estimated for detections in the direct reconstruction (green data points) has been artificially enhanced by a factor of 10 to exemplify the difference in values between the two methods. Only clump IDs 1, 2, 5 and 7 are detected in the direct reconstruction. For the other clumps, we plot the SNR as an upper limit, set at 3. **Right:** PSF corrected clump sizes characterized by Gaussian HWHM for detections in the Hα maps obtained with the two methods of reconstruction. 54

B.1 Source-plane RMS error as a function of RBF widths for single Gaussian source models for a fixed peak SNR of 20 in the image plane. 80

B.2 Source-plane RMS error as a function of RBF widths for non-overlapping double Gaussian source models for a fixed peak SNR of 20 in the image plane. 81

B.3 Source-plane RMS error as a function of RBF widths for single Gaussian source models for a fixed ratio of PSF FWHM / Image plane sampling = 2.0. 82

B.4 Source-plane RMS error as a function of RBF widths for non-overlapping double Gaussian source models for a fixed ratio of PSF FWHM / Image plane sampling = 2.0. 83

B.5 Source-plane RMS error computed on single Gaussian source profiles reconstructed with pixelated modelling technique as a function of the ratio of PSF FWHM to image plane sampling at the "best" RBF size. 84

B.6 Source-plane RMS error computed on single Gaussian source profiles reconstructed with direct ray-tracing as a function of the ratio of PSF FWHM to image plane sampling. 85

B.7 Source-plane RMS error computed on non-overlapping double Gaussian source profiles reconstructed with pixelated modelling technique as a function of the ratio of PSF FWHM to image plane sampling at the "best" RBF size. 86

B.8 Source-plane RMS error computed on non-overlapping double Gaussian source profiles reconstructed with direct ray-tracing as a function of the ratio of PSF FWHM to image plane sampling. 87

List of Tables

2.1 Constraints used in modeling cswa128, most of them are labelled in Figure 2.3. Not all the knots identified in a1 and a2 are resolved in the less magnified images a3 and a4. 22

4.1 Newly added/modified functions committed to the publicly accessible LENSTOOL code to implement the pixelated source reconstruction algorithm. . . 40

CHAPTER 1

Introduction

> The cosmos is all that is or ever was or ever will be. Our feeblest contemplations of the Cosmos stir us - there is a tingling in the spine, a catch in the voice, a faint sensation, as if a distant memory, or falling from a height. We know we are approaching the greatest of mysteries....
>
> – Carl Sagan, Astronomer

Galaxies are the fundamental building blocks of the Universe. They not only trace the underlying matter but are also critical in understanding the chemical evolution of the Universe. Edwin Hubble was the first to classify galaxies on the basis of their visual morphologies - ellipticals, spirals and irregulars (Hubble 1926, 1936). Since then, Hubble's morphological classification has been further extended with more detailed classification schemes such as de Vaucouleurs (1959); Morgan (1958), which indicated that galaxy morphologies were closely related to other properties, e.g., spirals contain young stars with bursts of star-formation supported by rotation. Furthermore, these schemes are also believed to define an evolutionary sequence that galaxies roughly followed, e.g., spirals evolve into ellipticals that appear as large collections of red, old stars supported by random motions. However, in order to fully explain the origin of the observed properties of galaxies and the correlation among them, it is important to understand how they assembled and changed over time.

From a theoretical point of view, the hierarchical model of structure formation is the most accepted method of galaxy formation in the ΛCDM cosmological scenario (e.g. White & Rees 1978; Katz, Hernquist & Weinberg 1992; Navarro & White 1993; Cen & Ostriker 1993). In this model, galaxies form and evolve with a *bottom-up* configuration, i.e., through successive mergers of low-mass gas clouds that clump together and build up the galaxy mass over time. Such collisions of gas clouds result in the formation of stars within progenitors of galaxies also known as proto-galaxies. As new stars are born in the proto-galaxy, they enrich the environment with heavy elements via stellar winds or supernovae explosions. Metal enrichment further drives the evolution of proto-galaxies, which eventually merge to form larger galaxies.

On the observational front, understanding the physical mechanisms that drive galaxy assembly and their evolution into present-day objects remain one of the greatest challenges in the astrophysics. The goal of this thesis is to gain a deeper understanding of galaxy evolution by providing tools to study the physical properties of high redshift galaxies at the highest possible spatial resolution.

1.1. Spatially Resolved Observations of Galaxies

Rapid technological advances in imaging and spectroscopic techniques have made it possible to investigate potential origins of the vast diversity of observed properties of galaxies. Deep multi-wavelength surveys of galaxies (2dFGRS, Folkes et al. 1999; SDSS, York et al. 2000; COSMOS, Scoville 2007) have played a formidable role in constraining the evolution of global properties of galaxy populations such as luminosity, star formation and morphology to early epochs. As a result, a comprehensive picture of the peak era of star-formation activity belonging to $z \sim 1-3$ has emerged (Madau & Dickinson 2014). In the last decade, the development of Integral Field Unit (IFU) spectrographs and Adaptive Optics (AO) imaging techniques have combined the advantages of imaging and spectroscopy to investigate large samples of galaxies in a spatially resolved manner. They have dramatically improved our understanding of galaxy evolution by revealing details about the complex interplay between various physical processes such as gas cooling, star formation and feedback mechanisms.

Some of the first examples of IFU surveys of local galaxies include SAMI[1](Croom et al. 2012), CALIFA[2](Delgado et al. 2013), MANGA[3](Bundy et al. 2015), Atlas3D[4](Cappellari et al. 2011) that have measured the 2D-kinematics, resolved star formation and chemical distribution of galaxies in the local Universe. Furthermore, these surveys have provided an observational baseline for high-z redshift studies of galaxies. Some of the initial high-z surveys include SINS [5](z $\gtrsim$ 2; Förster Schreiber et al. 2006), IMAGES ($0.4 < z < 1$; Yang et al. 2008), MASSIV ($0.9 < z < 1.8$; Contini et al. 2012) and AMAZE [6](z $\gtrsim$ 3; Maiolino et al. 2008).

The general consensus from these surveys is that the physical picture of high-redshift galaxies ($z \geq 1$) is fundamentally different from those locally (see Glazebrook 2013, for a review). While morphologically they appear to be more clumpy, kinematically there is a mix of dispersion-dominated, rotationally supported disks and merging systems. However, a key picture that has emerged from these surveys is the "turbulent clumpy disc" paradigm which means that a large fraction (30%) of galaxies at high redshifts show disc like kinematic signatures with high gas fractions despite the irregular morphology. The star-forming regions in these high-z discs are extreme with masses in the range $\sim 10^{8-10}$ $M_\odot$ (Elmegreen et al. 2005, 2009; Förster Schreiber et al. 2011; Guo et al. 2012) and high values of velocity dispersions ranging between 50-200 km/sec (e.g. Förster Schreiber et al. 2006; van Starkenburg et al. 2008; Genzel et al. 2011; Wisnioski et al. 2011).

[1]http://sami-survey.org
[2]http://califa.caha.es
[3]http://www.sdss.org/surveys/manga/
[4]http://www-astro.physics.ox.ac.uk/atlas3d/
[5]http://www.mpe.mpg.de/~forster/SINS/sins_nmfs.html
[6]http://www.mrao.cam.ac.uk/~rm665/amaze/

While such surveys have made it possible to search for star-forming galaxies at much higher redshifts, one needs to be careful of the possible selection biases in their samples. Samples of galaxies for high-z surveys are usually selected using different colour-selection techniques and so they tend to be biased towards high stellar masses. In particular, differences have been observed in the kinematics between K-band selected and UV- selected star-forming galaxies (Glazebrook 2013). Another possible selection bias might be against dusty star formers without UV or line emission. Additionally, such observations suffer from limited spatial resolution by only covering a few resolution elements in the data. Therefore, it becomes difficult to construct a consistent picture of the high-z Universe using results from IFS surveys of varying resolutions, depths, redshift ranges and mass ranges.

A major revolution came through the surveys of gravitationally lensed galaxies (e.g., Jones et al. 2010b; Yuan, Kewley & Rich 2013; Wuyts 2015) that allowed us to peer further into the Universe at an unprecedented spatial resolution. Furthermore, lensed galaxies for such surveys were selected based on the amount of magnification and thus probed lower-mass galaxies with better spatial sampling. In extreme cases of giant arcs, the magnification achieved through lensing can be as high as few $\times 10$, rendering a physical resolution at scales less than 100 pc. They have uncovered a picture of star-forming regions that largely differs from the observations of unlensed studies of high-z galaxies. For example, lensed studies of high-z galaxies reveal much smaller clumps with sizes down to a few dozen parsecs (e.g. Livermore et al. 2012; Johnson et al. 2017b) and significantly lower masses (e.g. Dessauges-Zavadsky et al. 2017).

1.2. Strong Gravitational Lenses as Cosmic Telescopes

Gravitational lensing is a phenomenon in which light rays are deflected by gravity. Einstein (Einstein 1936) formulated the mathematical theory of lensing due to the potential of massive stars. However he believed that owing to the limited resolution of the telescopes, there was not much hope of observing it directly. Later Zwicky (1937) realized the possibility of gravitational lensing by the potential of the galaxies (nebulae at that time). It took almost half a century to detect the first gravitational lens QSO 0957+561 A, B using optical spectroscopy in 1979 (Walsh, Carswell & Weymann 1979). Einstein rings, a particularly interesting manifestation of gravitational lensing, were first discovered in a radio source MG1131+0456 by Hewitt et al. (1988). They occur when a rare alignment of the source, lens and the observer occurs. Once observations of gravitational lens became routinely possible, focus shifted on using it as a tool. Refsdal (1964) and Liebes (1964) suggested the use of the lensing effect to measure masses of stars (by considering them as point mass lenses). This idea was extended to galaxies (Dyer & Roeder 1980) and clusters of galaxies (Narayan, Blandford & Nityananda 1984). For the first time, Soucail et al. (1988) measured the redshift of a giant arc behind a cluster Abell 370.

1.2.1. Lensing Basics

As we use lensing as a tool rather than studying the effect itself, a detailed discussion of the theoretical aspects is beyond the scope of this work. However, in this section, we discuss some of the background and introduce the terminology that will be used throughout the work. Figure 1.1 demonstrates the overall geometry of a gravitational lens system in which a source lies at a distance D_s from the observer, with an intervening lensing potential at a distance D_d from the observer and D_{ds} from the source. The order of magnitudes of distances between a source and a lens is assumed to be much larger than that of the sizes of either the source or lens. As a result, it is only important to study the defection within a thin zone close to the lens; generally known as the thin screen approximation. In mathematical terms, mass distribution of the lens can then be projected along the line of sight and replaced by a mass sheet (often called the lens plane) orthogonal to the sight line. The net deflection angle due to this mass sheet is then equal to the contributions from all the mass elements in the lens plane and is given as:

$$\vec{\alpha} = \frac{4G\, D_{ds}}{D_s\, c^2} \int \frac{(\vec{\varepsilon} - \vec{\varepsilon'})\Sigma(\vec{\varepsilon'})}{\mid \vec{\varepsilon} - \vec{\varepsilon'} \mid^2} d^2\varepsilon' \tag{1.1}$$

where ε is the two-dimensional vector in the lens plane and $\Sigma(\varepsilon)$ is the surface mass density of the lens. The angular diameter distances between observer and lens, lens and source, and observer and source are D_d, D_{ds} and D_s respectively. As a result of the deflection, the observer receives the light emitted by the source (S) as if it was emitted from the angular position θ (I).

For the focussing effect of the lens to occur, the lens should have a particular density called the critical density Σ_{cr}, where $\Sigma_{cr} = \frac{c^2}{4\pi G} \frac{D_s}{D_d D_{ds}}$ for a circularly symmetric lens.

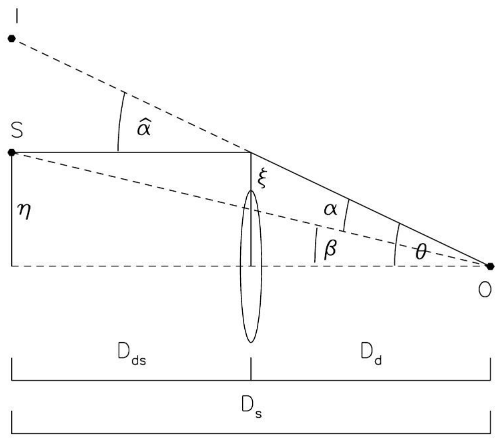

Figure 1.1 Lensing Geometry. The quantities D_d, D_{ds} and D_s represent the angular diameter distances between observer and lens (or deflector), lens and source, and observer and source. The angular position of the source (S) is defined as $\vec{\beta}$, that of the image (I) is $\vec{\theta}$ and the deflection angle is called $\vec{\alpha}$. Figure from Narayan & Bartelmann (1996).

While deflection preserves the surface brightness, its spatial variation as a function of the image position produces a change in the solid angle. An important consequence of the deflection is the magnification as the total flux of the source is changed in proportion to the ratio between the solid angles of the image and the source. More details on the theoretical definition of magnification have been provided in Section 1.3. For extended sources, for example background galaxies, we observe differential deflection of light bundles, thus causing distortion of the shape of these objects.

In general, we observe two types of lensing effects - (a) Strong, which is seen in the form of highly distorted arcs and multiple images and (b) Weak, which involves small distortions in the shapes of the background galaxy images. Whenever a lens has $\Sigma > \Sigma_{cr}$, strong lensing features are usually pronounced and we see multiple images of the source.

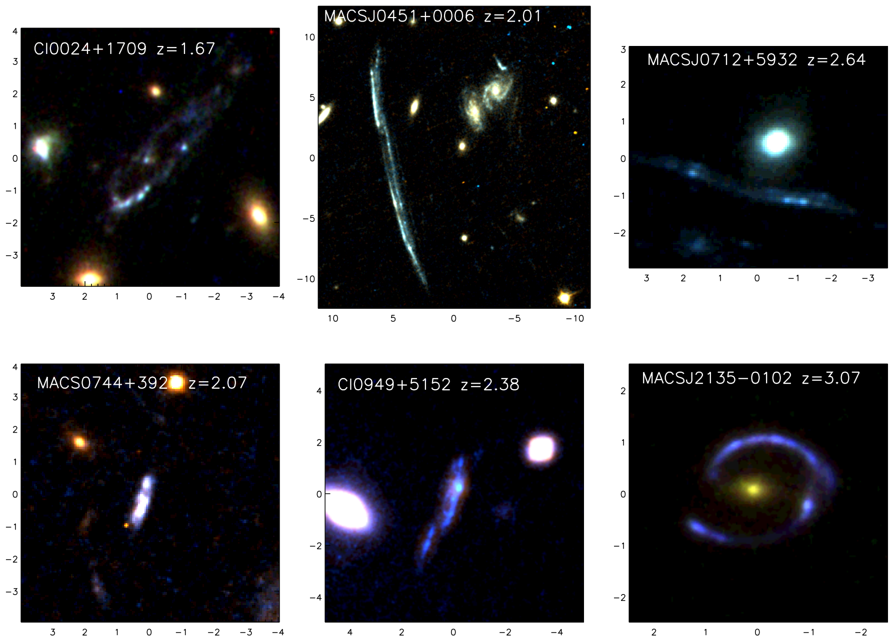

Figure 1.2 Examples of lensed high-z arcs as observed by HST. Figure from Jones et al. (2010b).

1.2.2. Peering into the high-z Universe: Cluster-scale Lensing

Strong lensing by massive galaxy clusters results from most extreme bending of light and is often accompanied by multiple images of background galaxies that appear as giant arcs (Figure 1.2) around central cores of clusters. As a result, these lensed images are highly distorted and magnified therefore enabling high spatial resolution in distant star-forming galaxies which are otherwise beyond the resolution and detection limit of current observations.

Cluster-scale lensing has consistently provided a number of high redshift candidates for detailed studies since the pioneering invention of Hubble Space Telescope (HST) (for e.g., Franx et al. 1997; Stark et al. 2007; Bradley et al. 2008; Bouwens et al. 2012; Zheng et al. 2012). The Hubble Frontier fields initiative (HFF; Lotz et al. 2014; Coe et al. 2014) combined with IFU spectroscopy has made it possible to leverage the magnifying power of strong lensing to achieve unprecedented spatial resolution in studying high-z galaxies (e.g. Patrício et al. 2018). Infact, the second farthest known galaxy up to date has been discovered with the help of Cluster Lensing and Supernova survey with Hubble (CLASH) at a photometric redshift of $z = 10.7^{+0.6}_{-0.4}$ (95% confidence limits; with z < 9.5 galaxies of known types ruled out at 7.2-σ, Coe et al. 2013). As a result, high-z lensing observations are being utilised to establish relevant connections to their local counterparts through underlying gas accretion processes. Chemical abundances (Cresci et al. 2010; Jones et al. 2010a; Yuan et al. 2011; Swinbank et al. 2012; Jones et al. 2013; Stott et al. 2014; Troncoso et al. 2014; Jones et al. 2015), spatial distribution and sizes of star-forming regions (Genzel et al. 2008; Jones et al. 2010a; Livermore et al. 2012) have provided valuable insights into the assembly history, particularly gas-accretion processes responsible for fuelling the star-formation rate of massive galaxies in the early Universe.

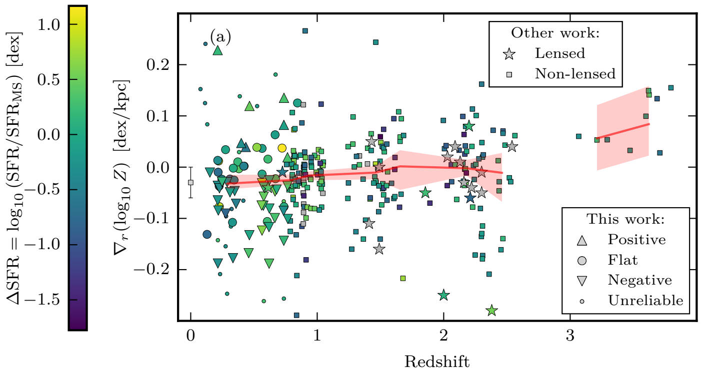

Figure 1.3 Compiled metallicity gradient measurements from literature. These gradients come from studies of galaxies that have been gravitationally lensed (star symbols), and non-lensed galaxies (squares). Where possible, data points are coloured to indicate the SFR relative to the main sequence (ΔSFR). As apparent, there is a considerable scatter in the observed gradients and no significant correlation between ΔSFR and metallicity gradient. Figure from Carton et al. (2018).

Probing Metallicity Gradients in Distant Universe

Metal content in star-forming galaxies is a result of complex interplay between star-formation activity and distribution (accretion or loss) of gas through feedback processes. Therefore metallicity gradients directly characterize the dynamics of ionized gas regulating the processes of star-formation within galaxies. The natural result of a hierarchical Universe is the inside-out formation scenario of galaxy formation, with outer regions of the galaxy being created from the infall of surrounding gas onto the denser central parts of galaxies. As a result, galaxy cores are expected to be more metal-enriched as compared to the outer edges of the galaxies. Observations of a substantial fraction of low redshift galaxies have reported negative metallicity gradients with similar slopes (when normalized to the size of the galaxy Ho et al. 2015). Interestingly, the high-z picture is strikingly far from being similar.

Spatially resolved abundances of both lensed and unlensed galaxies at $z > 0.1$ show a broad distribution of metallicity gradients with slope varying from negative to flat and positive (Jones et al. 2015; Leethochawalit et al. 2016; Wang et al. 2018) with a large amount of scatter in the observed values (Stott et al. 2014; Wuyts et al. 2016; Carton et al. 2018). A possible explanation given in literature for positive (inverted) or flatter metallicity gradients in galaxies is the influx of metal-poor gas into their inner regions through galaxy-galaxy interactions or cold flows thus suppressing the metallicity. Since the inflowing gas is expected to increase the star-formation activity, studies have tried to identify trends between the increased star-formation rates in galaxies with flatter or inverted gradients. While some studies demonstrate this trend (Stott et al. 2014), as shown in Figure 1.3, this might not be the case everywhere. In order to resolve this discrepancy, it has become necessary to thoroughly understand the systematics associated with metallicity gradient measurements.

One of the biggest contributing factors is angular resolution that has been shown to significantly affect the observed gradient of the galaxy. For example, Yuan, Kewley & Rich (2013) demonstrated that seeing-limited observations are likely to produce systematically flatter metallicity gradients. Moreover, there exists a critical angular resolution full width at half maximum (FWHM) range beyond which the measured metallicity is significantly more flattened than the intrinsic metallicity. While this threshold depends on the intrinsic metallicity, it is clear that we need to utlize lensing magnification to reach the maximum possible resolution in the galaxy plane.

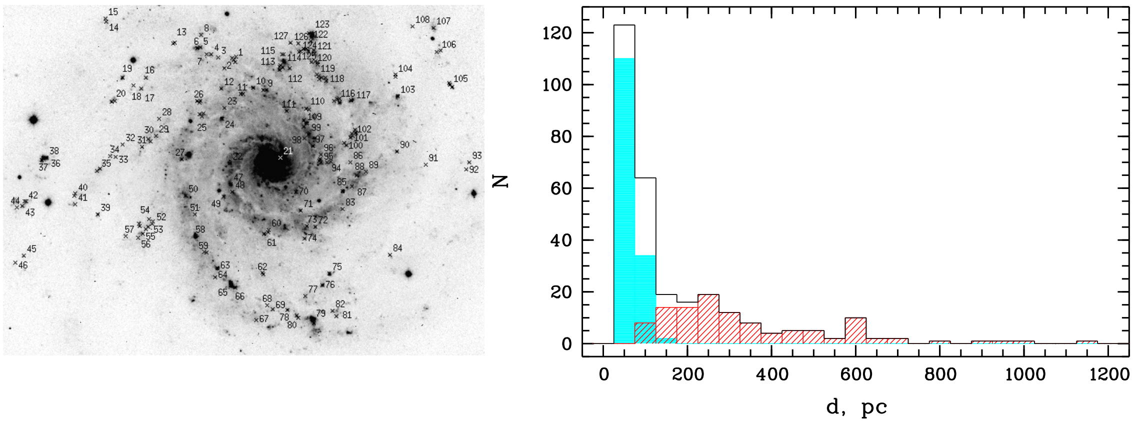

Figure 1.4 *Left:* HST B- band image of local galaxy - NGC628 with the positions of its star-forming regions overlaid on top as black crosses. *Right:* Number distribution of star-forming regions of different levels of hierarchy within the galaxy. Different colored histograms represent the distribution of star formation regions belonging to different hierarchical levels. Figure from Gusev (2014).

Probing Star Forming Clump Sizes in the Distant Universe

H II regions are the sites of star formation that play a critical role in constraining the overall stellar evolution and chemical enrichment in galaxies. The physical scale of star-forming regions contain significant imprints of processes regulating the changing cosmic environment as galaxies build up their stellar mass. Observations in the local Universe have shown that the H II region sizes span at least an order of magnitude, from small OB associates ($\sim$ 60 pc), stellar aggregates ($\sim$ 240 pc) to large star complexes ($\sim$ 600 pc), with a decrease in surface brightness from the smallest to the largest scales (Elmegreen et al. 2006; Gusev 2014, Figure 1.4).

However, the distribution of high-z clump sizes is currently under hot debate. Observations of the most luminous star-forming galaxies at $z > 1$ show that gas rich disks fragment into large kpc scale clumps with high velocity dispersions (e.g. Genzel et al. 2011; Förster Schreiber et al. 2011, 2018). Investigations into the ionized gas kinematics of high-z galaxies state that clumps form mostly in turbulent rotating disks rather than ongoing mergers (e.g.

Genzel et al. 2006; Bouché et al. 2007; Cresci et al. 2009; Wisnioski et al. 2015; Contini et al. 2016) although the latter scenario can't be completely ruled out (Leethochawalit et al. 2016). While turbulence is speculated to largely sustain high velocity dispersions of the clumps, it is unclear exactly how it does so. On the other hand, studies of local analogs of high-z galaxies ($L_H > 10^{42}$ erg/s in DYNAMO galaxies, Green et al. 2014; Fisher et al. 2017) show smaller clumps in disks with similar velocity dispersions and size measurements as the clumps in the local Universe.

High resolution hydrodynamic simulations predict that large star-forming clumps viewed at kpc resolution may fragment into a cluster of smaller clumps (Behrendt, Burkert & Schartmann 2015; Bournaud 2016; Fensch et al. 2016; Tamburello et al. 2017) making the discrepancy in clump sizes a mere result of the systematic effects of resolution in observations. Studies of lensed systems support the simulations and indeed reveal clumps with sizes much smaller than the usual kpc diffraction limit of HST (e.g. Jones et al. 2010b; Swinbank et al. 2010; Livermore et al. 2012, 2015). More recently, Johnson et al. (2017a) have achieved a resolution limit of ~ 20-30 pc (magnification dependent) for a lensed system at $z \sim 2$ thereby revealing star-formation at scales that had never been previously accessed in the distant Universe (Figure 1.5).

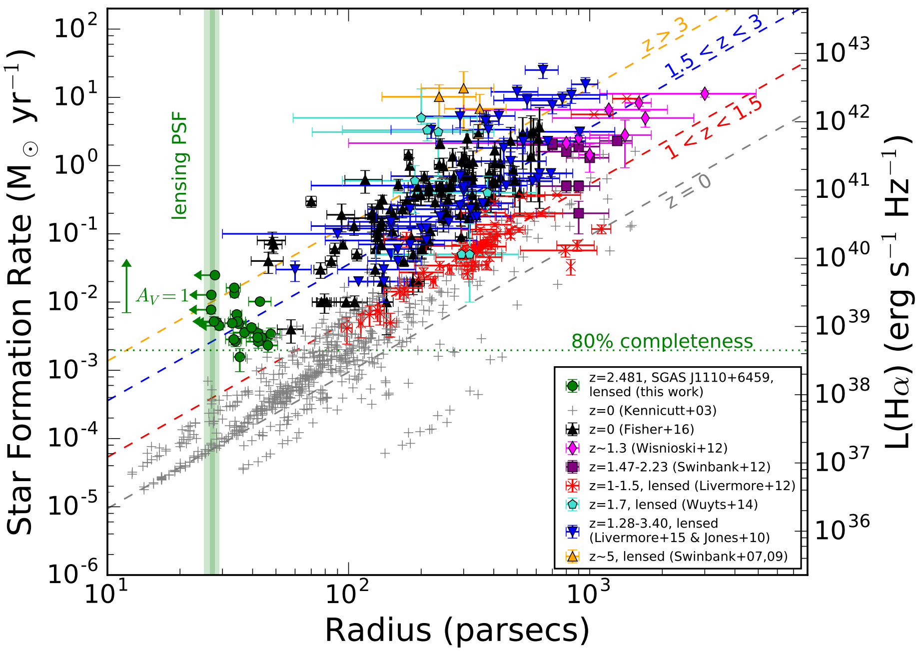

Figure 1.5 Star-formation - radius relation in the individual clumps in the lensed galaxy SGAS J111020.0+645950.8 at $z = 2.481$. This plot is a compilation of literature measurements of the clump sizes in both, lensed and unlensed galaxy samples. Clumps from the lensed galaxy at $z = 2.481$ with star formation rates and sizes estimated from the rest-frame ultraviolet (F606W filter) are plotted in green. The lensing PSF is shown with a vertical green stripe. For the five green points where the lensing PSF was larger than the measured size, the clump size is plotted as an upper limit at the value of the lensing PSF. Figure from Johnson et al. (2017a).

However, lensed studies are currently limited by the uncertainties in different lens modelling techniques. Nonetheless, with the current state of art technological capabilities, only the improved resolution provided by lensing has the potential to find out whether H II regions at high-z have intrinsically larger sizes than local galaxies, or this is simply a consequence of beam-smearing. Furthermore, this resolution gain enabled by lensing provides a possible pathway to study turbulence in high-z clumps and resolve the controversies around their cosmic evolution by resolving gas physics in the disc on sub-kpc scales.

1.3. Lens Modelling- *Lenstool*

In order to determine the intrinsic properties of galaxies, it is necessary to account for the lensing magnification which in turn requires the knowledge of the mass distribution of the lensing cluster. Therefore, the reliability of results derived about the physical properties of lensed galaxies depends strongly on the accuracy of the lensing mass models used to interpret their observations.

Lens modeling is a rapidly developing field in the past decade and has seen enormous progress in terms of the number of techniques used to model lenses (Liesenborgs, De Rijcke & Dejonghe 2006; Coe et al. 2008; Diego et al. 2015). Broadly speaking two kinds of approaches have been used for mass reconstruction of lensing clusters - Parametric and Non Parametric. Parametric models consider a physically motivated analytical profile for the potential of lens represented by a range of parameters. Then the model is optimised to obtain a set of best-fit parameters using some well-defined constraints. Parametric models are robust and avoid unphysical solutions. However, they rely on specific analytical models for the lensing potential that may be questionable in cases of complicated lensing examples. Whereas, non parametric models are "grid-based" (e.g., Lefor, Futamase & Akhlaghi 2013) in which mass distribution is considered to be made up of a regular grid of small elements of mass called pixels. This grid can either be static (e.g., Saha & Williams 1997; Abdelsalam, Saha & Williams 1998) or dynamic (e.g., Diego et al. 2005) in which it is refined iteratively in regions of high mass density. Sometimes, pixels are replaced by suitable basis functions so as to effectively enhance the intra-grid resolution. On one hand, there is clearly more flexibility in the non parametric way of modelling because of the large number of free parameters than the constraints while on the other hand, this can also lead to overfitting of data if the technique is not utilized carefully. This calls for the need of an external regularisation criterion (e.g mass positivity, limits in the derivatives of the solution) to avoid unwanted parameter degeneracies and identify the best physically motivated model.

A more recent approach to lens model classification is to classify models as LTM (Light traces mass) or Non LTM models because strictly speaking, both parametric and non parametric approaches are dependent on parameters. As the name suggests, LTM approach relies strongly on the assumption that galaxies follow the underlying mass distribution. Although this assumption is well supported by galaxy-galaxy lensing studies (Wilson et al. 2001) as well as clusters (Clowe & Schneider 2002), non LTM models have also been successfully able to achieve highly resolved mass distribution of lenses (Coe et al. 2010). This is because deviations from the standard LTM parametrization is likely to occur due to the presence of substructures along or behind the line of sight, scatter in galaxy mass to light ratios or asymmetric spread of dark matter within cluster halos. Lately, another improvement in this field has been to include the strengths of both the methods to reconstruct the lensing potential (Jullo & Kneib 2009). This essentially tries to give weight to the analytically traceable features of the potential with more complicated substructures.

LENSTOOL[7], one such method, is a lens ray-tracing software package for efficiently modelling galaxy clusters, first developed by Kneib (1993). It adopts a multi-scale model that accurately reconstructs the mass distribution in regions of highest density using large number of multiple image constraints at the same time extending the mass reconstruction to weak lensing regime of the lensing cluster using a grid of radial basis functions (RBF) with physically motivated profiles. Figure 1.6 illustrates the use of LENSTOOL in mass reconstruction of a complex merging cluster Abell 2744.

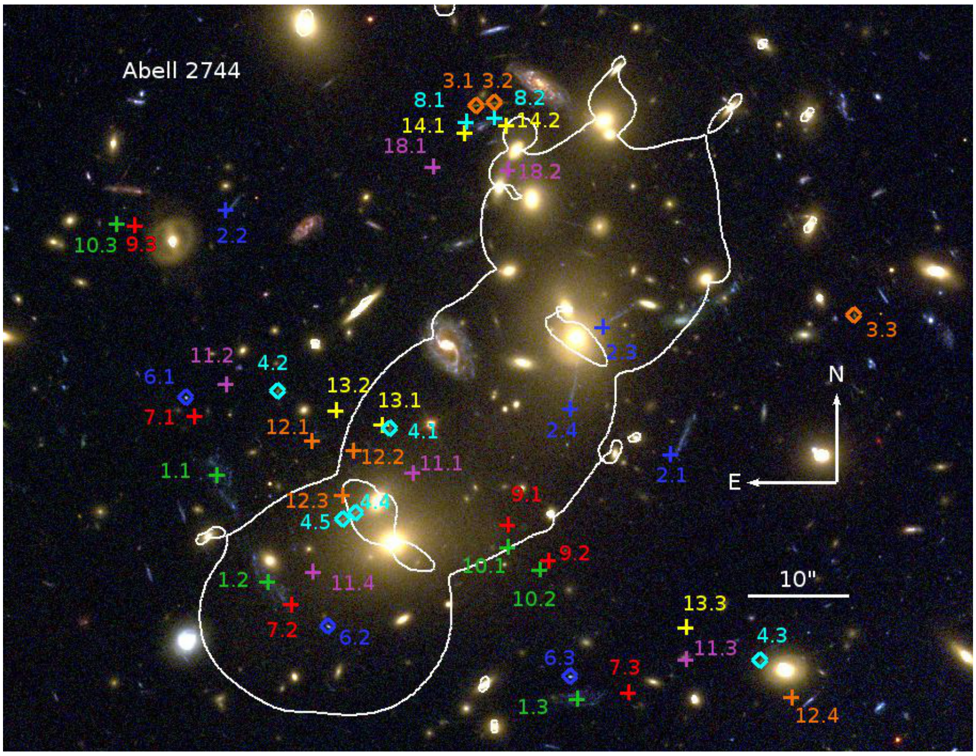

Figure 1.6 Overview of lens model and multiple-image systems for Abell2744. The underlying colour image is a composite created from HST/ACS images in the F814W (red), F606W (blue), and F435W (green) passbands. The locations of multiply imaged galaxies used as constraints in the model of Abell 2744 are overlaid. Diamonds designate image systems with spectroscopic redshifts, where crosses indicate that the redshift of the image system is left as a free parameter in the model. The critical curves (white) trace the region of high magnification for a source at z = 2. Figure from Johnson et al. (2014).

In my thesis, we use LENSTOOL to carry out detailed mass modelling of complicated lensing potentials. To give a clear theoretical foundation for modeling work, I will briefly summarise the necessary background. From simple geometry in Figure 1.1, we can see that

$$\vec{\beta} = \vec{\theta} - \vec{\alpha}(\vec{\theta}) \tag{1.2}$$

This equation forms the foundation of gravitational lensing and is known as the **lens equation**. Conveniently, lensing is considered as a reverse problem: where we construct a mass model given the position of observed images i.e. θ. Then, solving the lens equation, the source position β is inferred. The general and the most physical constraint on these

[7]http://projets.lam.fr/projects/Lenstool/wiki

inversion methods is the fact that different source regions corresponding to a given multiple image system should overlap as well as possible. Mathematically speaking, for an arbitrary lens potential, lens mapping can be described by the Jacobian matrix :

$$A = \frac{\partial \vec{\beta}}{\partial \vec{\theta}} = \left[\delta_{ij} - \frac{\partial \alpha_i(\vec{\theta})}{\partial \theta_j} \right]. \tag{1.3}$$

A is also called the inverse magnification tensor (M) which is $\frac{\partial \theta}{\partial \beta}$. The distortion in solid angle is given by the determinant of A. Transforming this equation in terms of partial derivatives of properly scaled and projected Newtonian potential of the lens $\psi(\theta)$, it can be shown that :

$$\mu = detM = \frac{1}{detA} = \frac{1}{[(1-\kappa)^2 - \gamma^2]} \tag{1.4}$$

where κ refers to the physical convergence or the isotropic magnification of the source (for e.g., a circle transforming to a circle with larger radius) and γ denotes the magnitude of the anisotropic shear in the mapping (a circle transforming to an ellipse).

Critical curves are curves in θ space where $detA = 0$. Corresponding curves in β space are called caustics. It is possible to look at critical curves and caustics in terms of magnification. These are curves of infinite magnification i.e. $\mu = detM = \frac{1}{detA} \rightarrow \infty$. They are of great importance because

1. They highlight regions of high magnification.

2. They demarcate the regions of different image multiplicity.

Figure 1.6 demonstrates the critical curves modelled for one of the well-studied cluster Abell 2744.

Current cluster-scale lens models have not been able to improve their image plane accuracy to match the resolution of observations used to construct the lens model in the first place. For comparison, in observations, HST image-plane resolution is $0.05'' - 0.1''$ and the typical angular resolution for IFS - AO observations is $0.1''$ whereas the residual root mean square (RMS) of most lens models lie between $0.2''$ and few arcseconds (Limousin et al. 2007; Lagattuta et al. 2017; Caminha et al. 2017). Line of sight substructures, redshift information of multiple image systems have been shown to have a significant contribution to the systematic errors arising in strong lens models of lensing clusters (Bayliss et al. 2014a; Johnson & Sharon 2016; Acebron et al. 2017). Most recently, HFF observations have significantly improved these errors by utilizing large number of constraints, both across the image plane and the redshift space (e.g. Acebron et al. 2017; Mahler et al. 2018).

1.4. Motivation

Magnification is one of the key quantities that we need from lensing modelling to interpret observations of lensed galaxies. While it is the accuracy of the lensing mass model that plays a major role in determining the best-fit magnification of the lensed system, precision of the source-plane reconstruction is the key to achieve the natural resolution of lensing. Even with the use of accurate lens models, simple source reconstructions removing the lens deflection from the observations does not allow us to correctly recover the intrinsic source-plane surface brightness. This is because of the point spread function (PSF) smearing of the image either from atmosphere or telescope (e.g. AO system or instrument).

The traditional approach of backward ray-tracing the image using equation 1.2 introduces a differential PSF smearing in the source plane due to the combination of the image-plane PSF and asymmetric lensing shear. This gives rise to an effective spatial source plane resolution that is significantly lower than that enabled by the lensing amplification. For example, the size of the source plane PSF for a $z \sim 2$ galaxy magnified by a factor of 10, can reach upto few hundred parsecs, thus preventing to resolve structures at scales below this resolution in the source morphology. Furthermore, in scenarios where there are multiple images of the same galaxy, it is of great interest to model them simultaneously and recover the best spatial resolution in the source plane.

However, in order to fully utilize the power of lensing and recover the physical properties of galaxy delensed, it is important to simultaneously combine the information from different images. This has been shown before by certain case studies (Coe et al. 2010; Jones et al. 2010a, 2015) of lensed systems. For example, Jones et al. (2010a) found that combining multiple images of a lensed galaxy at $z = 1.8$, the precision in measurement of metallicity gradient can be improved by almost a factor of 2. This is due to the fact that the effective source-plane PSF's of different images will have different orientation due to shear along different directions.

The effectiveness of LENSTOOL in lens modelling has been seen through some of the best image plane accuracies obtained for a variety of lensed systems in Hubble Frontier fields (e.g., Limousin et al. 2016; Lagattuta et al. 2017; Mahler et al. 2018). However the code for source reconstruction in LENSTOOL is currently only suitable for applications to simple profiles such as Gaussian or sersic light distributions. In reality, giant lensed arcs at high redshifts can actually have more complex surface brightness distribution (SBD). Therefore, a new approach is needed to effectively determine the SBD of the source galaxy.

A forward modelling approach of source reconstruction allows us to easily combine the observations from multiple images and deal with lensing PSF thus contributing to the accuracy of the reconstructed source brightness profile. The aim of the forward approach is simple: for a given lens model, utilize the constraints from the extended surface brightness profile of the lensed source to reconstruct its intrinsic profile. This approach not only overcomes the challenges posed by non-uniform PSF in reconstruction of strongly lensed arcs, it also fully exploits the unprecedented natural resolution of lensing otherwise missed by simple ray-tracing.

In this thesis, I explore the advantages of a forward source modelling approach in reconstruction of strongly lensed arcs over traditional image inversion methods. My thesis has two major components:- (1) First, I conduct a pilot study to test the use of a simplified forward source modelling approach on a strongly lensed galaxy at $z \sim 2$: SDSS1958+5950 and combine IFU observations from different multiple images of the lensed target. (2) Next, I extend the approach used in the pilot study to a fully automated algorithm for the forward source modelling of lensed galaxies behind cluster-scale lenses that deconvolves the effects of PSF. The algorithm utilizes the constraints from the extended surface-brightness profile of the lensed source for a given lens model and reconstructs its intrinsic distribution on a pixelated grid using a bayesian Monte-Carlo Markov chain (MCMC) optimization algorithm in LENSTOOL. I directly compare the results of forward reconstruction with simple ray-tracing to quantify the effects of source-plane PSF on the physical properties of lensed target galaxy.

One of the most compelling science drivers for the construction of the next generation of telescopes, such as the Giant Magellan Telescope (GMT) and the James Webb Space Telescope (JWST) is to study the formation and evolution of galaxies, especially the processes of star-formation and chemical enrichment occurring within distant, young galaxies on scales corresponding to individual star-forming regions. Accurately measuring the sizes and intrinsic velocity dispersions of clumps at high-z is crucial for understanding the role of turbulence on star-formation processes and the differences as compared to the local galaxies. Therefore it is imperative that current source modelling techniques reach the accuracy needed to interpret the wide variety of lensed systems that will become available with the future instruments such as the Near InfraRed Spectrograph (NIRSpec) aboard JWST or the Giant Magellan Telescope integral fields spectrograph (GMTIFS) on GMT in addition to lensed surveys by the Large Synoptic Survey Telescope (LSST).

1.5. Thesis Outline

The thesis aims to gain a deeper understanding of star-formation processes at sub-kpc scales by enabling the highest possible resolution in recovering the intrinsic properties of lensed galaxies. We have developed a fully Bayesian forward source modelling approach that enables deconvolution of PSF smearing effects from source profiles of strongly lensed galaxies in galaxy clusters.

As mentioned earlier, the use of an accurate source reconstruction technique relies heavily on a robust mass model of the lensing cluster. We begin with reconstructing a detailed mass distribution map of the lensing potential of SDSS1958+5950. Chapter 2 presents our work on the lens modelling of this system. This chapter describes our high-resolution imaging data from the Near-Infrared Camera (NIRC2) on Keck II telescope that was used to provide multiple image constraints for lens modelling. Throughout this thesis we adopt a standard Λ-CDM cosmology with $\Omega_m = 0.3$, $\Omega_\Lambda = 0.7$ and h = 0.7. All magnitudes are given in the AB system (Oke & Gunn 1983).

Chapter 3 describes our simplified forward source reconstruction technique that was used to combine IFU observations from different lensed images of the source galaxy at $z \sim 2$. We analyze the reconstructed morphology, kinematics, chemical gradient of the source galaxy based on the updated lens model at the highest spatial resolution enabled by lensing.

Chapter 4 describes our automated pixelized grid reconstruction technique implemented in LENSTOOL. We test this algorithm using different types of source profiles and compare the RMS error on reconstructions obtained using the new pixelized grid algorithm with traditional method of source reconstruction.

Chapter 5 details the application of the pixelated algorithm on the lensed galaxy at $z \sim 2$ in lensing group SDSS1958+5950. We identify clumps in the derived source plane Hα intensity maps and compare their physical sizes using the traditional and pixelated methods of reconstruction. There is an improvement in the signal-to-noise ratio (SNR) of clumps by ~10 times in the reconstructed profile by the pixelated technique compared to that obtained with traditional ray-tracing.

Chapter 6 summarises the main conclusions of my thesis. It briefly describes the current and future work simulated by my thesis.

CHAPTER 2

Pilot study of $z \sim 2$ lensed galaxy: Lens Model

This chapter has been previously published as 'High-resolution spatial analysis of a $z \sim 2$ lensed galaxy using adaptive coadded source-plane reconstruction', Sharma, S., Richard, J., Yuan, T., et al. 2018, MNRAS, 481, 1427 .The work is presented here in expanded and updated form.

2.1. Introduction

Magnification factors of strongly lensed systems can easily range between 1 - 10 (e.g. Richard et al. 2011), with reasonable lensing uncertainties (10 - 25 % ; Richard et al. 2011; Collett 2015). In extreme cases of giant arcs around galaxy groups and galaxy clusters, the magnification can reach up to a few $\times$ 10, rendering a physical resolution of less than 100 pc at $z \sim 2$. Therefore, giant distorted arcs are ideal candidates to study the physics of high-redshift SF regions at highest spatial resolution possible (Swinbank et al. 2006; Jones et al. 2010b; Yuan et al. 2012; Bayliss et al. 2014b; Livermore et al. 2015; Johnson et al. 2017b; Girard et al. 2018).

We choose one of the brightest targets in The Cambridge Sloan Survey of Wide Arcs in the Sky (CASSOWARY), SDSS1958+5950 (hereafter referred by its survey-ID: cswa128; $z = 2.225$). CASSOWARY survey presented a large sample of about 100 group-scale gravitationally lensed systems at $z \sim 1-3$ from the Sloan Digital Sky Survey (SDSS; York et al. 2000) imaging data (Stark et al. 2013). The survey targeted star-forming galaxies ($z \sim 1-3$) being lensed by an early-type galaxy (or group) at $z \sim 0.2-0.7$. Leethochawalit et al. (2016) (hereafter L16) presented IFU observations of a representative sample of 15 lensed galaxies from the survey.

cswa128 is lensed by a galaxy group at $z = 0.214$ and reported to have high [N II]/Hα at the outer edges, by previous work of (L16). A lens model based on SDSS imaging data was used to interpret IFU observations on a single lensed arc of this target. In this chapter, we present high resolution imaging data from the NIRC2 instrument on the Keck I telescope that enables us to build a more complex lens model for this system. We also discuss new spectroscopic observations on another lensed image of the galaxy than previously observed by L16.

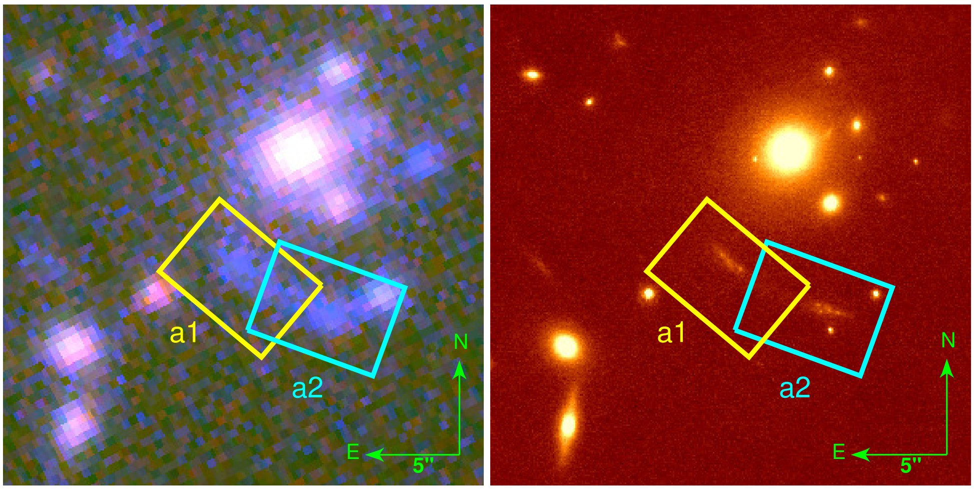

Figure 2.1 **Left:** SDSS color composite image of cswa128, lensed galaxy behind a galaxy group at $z = 0.214$ (red: SDSS z′ filter, green: SDSS r′ filter, blue: SDSS g′ filter). The OSIRIS pointings are indicated by two rectangles, each covering a different multiple image of the lensed galaxy at a mean systemic redshift of $z = 2.225$. Yellow rectangle a1 ($t_{exp} = 5.4$ks) represents OSIRIS field for previous observations by L16 while our new observations are shown by the cyan rectangle a2 ($t_{exp} = 5.4$ks). **Right:** Our new NIRC2 Kp band imaging data ($t_{exp} = 8.4$ks) with OSIRIS pointings overlaid on top. The spatial resolution has improved by a factor of 10 with NIRC2 observations. The length of the compass indicates an angular scale of 5.″0.

2.2. Observations and Data Reduction

2.2.1. Previous Data

CSWA128 is one of the brightest (r = 19.6) lensed galaxies included in the CASSOWARY survey with a mean systemic redshift of 2.225 derived using Hα and [OIII] λ 5007 emission lines (Stark et al. 2013). Publicly available *gri* imaging data from SDSS DR8 (Figure 2.1) had been used previously for creating a lens model for this system (Stark et al. 2013). The lensing galaxy group was spectroscopically confirmed to be at $z = 0.214$ (Stark et al. 2013). L16 conducted a follow up study using AO aided near-infrared IFU observations with OSIRIS (Larkin et al. 2006) instrument on the W. M. Keck I 10 m telescope. The physical location of their OSIRIS field is shown in yellow on the SDSS color composite in Figure 2.1.

2.2.2. New Data

NIRC2 Imaging data

To obtain a higher resolution image of the lensed system, cswa128 was observed with NIRC2 on 2017, September 8 UT using the laser-guide star (LGS) AO system on Keck II (PI: S.Sharma). Observations were taken in wide field mode ($40'' \times 40''$, plate scale 0.″04/pixel) using two filters Kp ($\lambda_0 = 2.12$ $\mu m, \Delta\lambda = 0.35$ μm), J ($\lambda_0 = 1.24$ $\mu m, \Delta\lambda = 0.16$ μm). Wide field mode was an optimal choice to obtain high resolution and cover the group members in the field of view (FOV) at the same time. A tip-tilt (TT) star with R $\sim$ 15.8 mag was chosen outside the FOV for these observations. Three point dithering (5″) pattern was adopted to avoid the noisy fourth quadrant of the detector. The total on-target exposure time was 8.4ks (Kp band) and 4.2ks (J band). J-K_p color image was mostly used for selecting the group members in our lens model, however due to relatively less exposure time in J band, we only present Kp band in this paper. Figure 2.1 shows the NIRC2 FOV for our observation. The spatial resolution of 0.″04 obtained using NIRC2 allows us to resolve fainter substructures in the lensed galaxy as shown in Figure 2.2.

The NIRC2 images were reduced with IRAF using the basic procedures that involved flat-fielding, sky subtraction and distortion correction. Flat-fielding was done by subtracting a stack median of lamp-off from lamp-on dome flats. The process of sky-subtraction was done iteratively. We constructed a sky image for every exposure using a sigma-clipped mean of its neighbouring exposures at different dither positions. After subtracting sky from the respective exposures, images were corrected for geometrical distortion and then stacked together to create an object mask. The objects identified in this mask were rejected for the next round of sky subtraction. Sky subtraction was repeated for a few more iterations till we converged on the final image after combining all the sky-subtracted frames. We used the 2MASS photometry to perform the flux calibration of our NIRC2 image. The astrometry was calibrated using SDSS imaging data by aligning location of the bright stars in the FOV.

OSIRIS IFU data

We obtained new data using OSIRIS with the natural guide star (NGS) AO system (Wizinowich et al. 2006) on the a1 multiple image (Figure 2.1) of the lensed galaxy. The observation was conducted on 2015, September 22 UT at (α_{2000}, δ_{2000}) = (19:58:35.117, +59:50:51.51)(PI:T.Yuan). The target was observed in the Kn2 band to cover the redshifted Hα and [N II] emission lines. We used a plate scale of 0.″1 which gave a field of view of 4.5×6.4 arcsec (Figure 2.1). The K_s = 9.8 mag NGS was chosen inside the NGS FOV of OSIRIS. A position angle (P.A.) of 70 deg. was used for the observation. We obtained five individual exposures of 900 s in an ABAB dithering sequence to optimize sky subtraction. The net on-target exposure time was 4.5 ks. The average spectral resolution was R ~ 3000 which corresponds to a resolution in velocity ~ 40 km/s. Centering of the IFU was done through short exposures of the TT star prior to science target exposure. The AO-corrected PSF was 0.″12.

We use the latest available OSIRIS data reduction pipeline (Larkin et al. 2006) to reduce the individual exposure frames. Major steps in the reduction pipeline include : dark and bias subtraction, flat-fielding, spectral extraction, wavelength calibration and telluric correction. Adjacent pairs of images were used as reference frames to perform sky subtraction through the IDL code of Davies (2007). The individual exposures were then combined using a 3σ mean clip to reject cosmic rays and bad lenslets. An A0D type standard star FS147 was used to perform telluric correction and flux calibration. The uncertainty in absolute flux calibration is estimated to be within 20%. The absolute astrometry calibration of the produced datacube was done using the high resolution NIRC2 image with an uncertainty of about 1 spaxel (~ 0.″1).

The critical analysis for this work is the extraction of emission line maps. We fitted gaussian profiles simultaneously to the three emission lines [N II] λ6548, 6583 and Hα after constraining the ratio of [N II] λ6548 and [N II] λ6583 to the theoretical value of 0.33 as described in

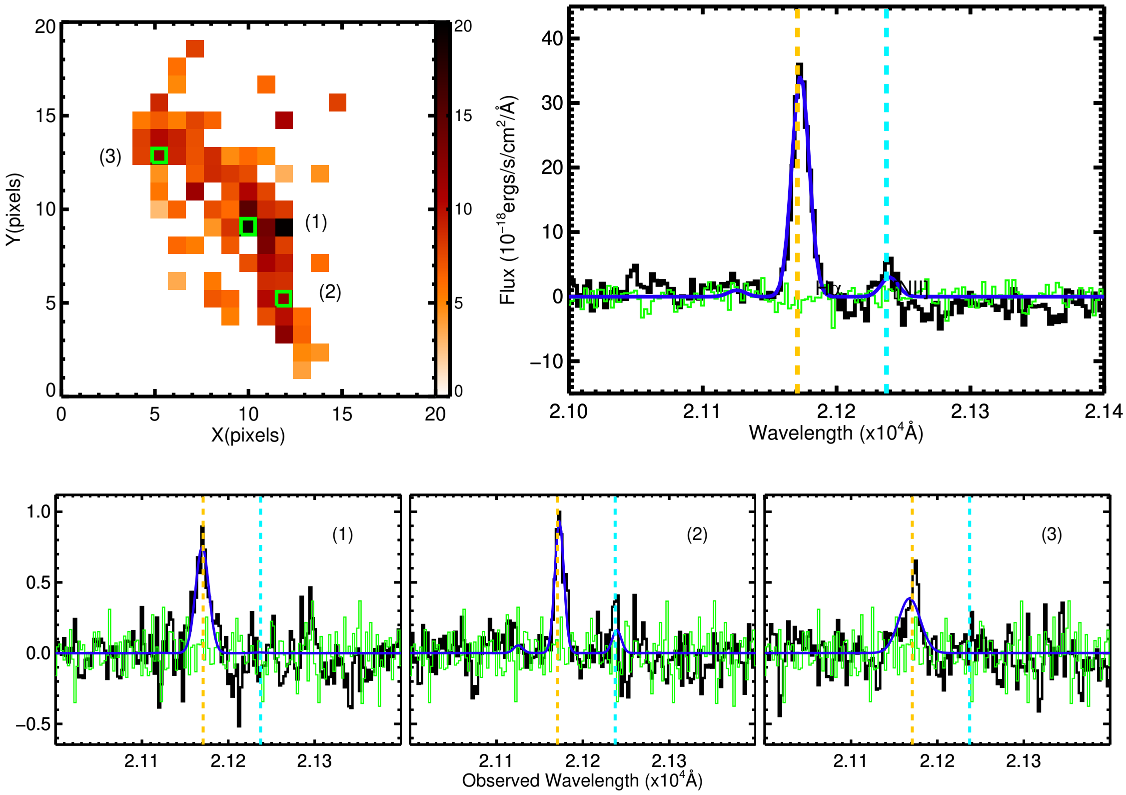

Figure 2.2 Examples of 1D spectra and Hα 2D intensity map from emission line fitting of new OSIRIS spectroscopic data on multiple image a2 of the lensed arc. **Top Left:** Hα 2D intensity map in units of 10^{-18} erg s^{-1} cm^2 arcsec^{-2} in the observed frame. 78 individual spaxels in the image plane achieve Hα SNR above 5σ. 1D spectra of the three green pixels in the 2D map are shown in the bottom three panels. **Top Right:** Integrated 1-D spectrum in the vicinity of Hα and [N II] lines obtained after summing all the IFU pixels with Hα detections above 5σ. The flux density is in units of 10^{-18} erg s^{-1} cm^{2}Å^{-1}. We achieve a SNR of 25 on Hα and 5 on [N II]. Note that the weaker [N II] λ6548 line is fixed to be 1/3 of the [N II] λ6584 line. The negative level of continuum is due to the its over-subtraction especially in the red part of the spectrum. **Bottom:** Panels shows the spectrum of individual spaxels. Yellow and Cyan vertical lines in Panels 1-4 indicate the location of redshifted Hα and red [N II] emission lines at $z = 2.225$ respectively. The raw spectrum is plotted in black; RMS of sky residuals in green and gaussian fits to the three lines are shown in blue.

Osterbrock (1989). We also constrained the mean and velocity width of [N II] λ6548,6583 lines to be the same as Hα λ6563. Fitting of emission lines was initially done for every spaxel in the image and source plane using a weighted χ^2 minimization procedure. Since the wavelength range covering [N II] and Hα lines was not dominated by the atmospheric OH lines, we followed the weighting procedure outlined in L16. For a given wavelength, the fitted spectra were weighted by a variance spectrum calculated using an emission line free region of the data cube. The generated 2D map from the emission line fitting had 78 spaxels with Hα SNR ≥ 5 and 15 spaxels with [N II] SNR ≥ 3 (Figure 2.2). We also present the coadded spectrum of all spaxels for comparison in Figure 2.2. Moreover, we notice that the spatial averaging of 3×3 surrounding spaxels fails to improve the SNR significantly. We present an adaptive binning technique using our new lens model to achieve higher SNR. The details of the method are discussed in Section 3.1.

2.3. Lens Modelling Methodology

The previous mass model for the galaxy group of cswa128 was constructed using the procedure described in Auger et al. (2013). The *gri* SDSS imaging data was used to fit a single Sersic profile to each of the lensing galaxy and the background source galaxy using a χ^2 optimization procedure. We use high resolution NIRC2 imaging data to obtain a well constrained lensing mass model. By finding additional substructures in observed images, we build a more robust model for this system. In this section, we describe our parametric approach to construct a strong lensing mass model for this system.

We use the publicly available software LENSTOOL[1] to reconstruct in detail the mass distribution of cswa128. The modeling software package LENSTOOL (Kneib 1993; Jullo et al. 2007) adopts a parametric approach to effectively model the mass distribution of lenses. It has been successfully used to model various lensed systems and has reliably reproduced the observations with best image plane accuracies (Jauzac et al. 2015; Limousin et al. 2016; Lagattuta et al. 2017; Mahler et al. 2018). A detailed reconstruction of the lensed galaxy involves the lensing model to capture both the *large* scale structure: caused by the potential of the host halo of the lens (galaxy group) and the *small* scale substructure associated with the locations of member galaxies within the galaxy group. These small scale potentials influence the distortions in lensing potential locally and are constrained using a light traces mass (LTM) approach by LENSTOOL. A Bayesian Monte Carlo Markov Chain (MCMC) minimization procedure in LENSTOOL (details about the procedure can be found in Jullo & Kneib 2009) was used to efficiently optimize the free parameters of the system.

A truncated Dual Pseudo-Isothermal Elliptical mass distribution (hereafter dPIE; Elíasdóttir et al. 2007) was used to model the mass components at both small and large scales. The dPIE profile is characterized by seven parameters: central position (x,y), orientation angle θ, ellipticity e, central velocity dispersion σ, two characteristic radii: r_{core} and r_{cut}. We model the group scale halo with a single dPIE profile and allow all its parameters except r_{cut} to vary freely with uniform priors. Since r_{cut} is unconstrained by strong lensing data, it is fixed to a value of 200 kpc, typical for group scale galaxy lenses.

To limit the parameter space, group members close to the arc within the strong lensing regime were included in the lens model. Individual galaxy clumps were also modelled with a dPIE profile, after fixing the associated geometrical parameters (x, y, e, θ) by running SExtractor (Bertin & Arnouts 1996) on the NIRC2 image presented in section 2.2.2. Other parameters (σ, r_{cut}) were scaled on the basis of K-band luminosity of galaxies (L_K), relative to a L_K^* galaxy using a constant mass-luminosity scaling relation (Faber & Jackson 1976) as described by the following equations (see also discussion in Richard et al. 2010) :

$$r_{core} = r^*_{core}(L_K/L^*_K)^{1/2}, \tag{2.1}$$

$$r_{cut} = r^*_{cut}(L_K/L^*_K)^{1/2}, \tag{2.2}$$

$$\sigma_0 = \sigma^*_0(L_K/L^*_K)^{1/4} \tag{2.3}$$

We fixed $r^\star_{cut}$ to 50 kpc but allowed $\sigma^\star_0$ to vary with a gaussian prior of mean $\mu = 158$ km/s and width $\sigma = 27$ km/s following the observational results of Bernardi et al. (2003) on $\sigma^\star$. Since

[1] http://projects.lam.fr/projects/lenstool

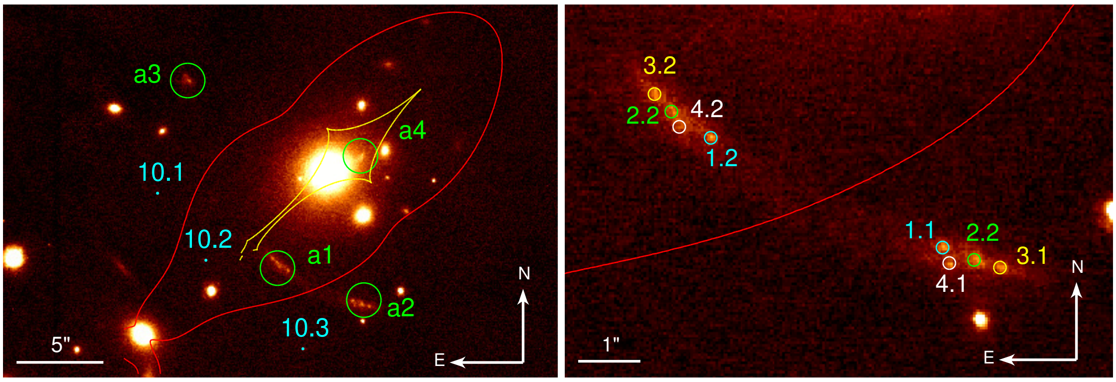

Figure 2.3 Our lens model of CSWA128. **Left:** NIRC2 imaging of CSWA128 in Kp band. Labeled in green circles (a1, a2, a3, a4) are the different multiple images of the lensed galaxy at $z = 2.225$. IFU data for a1 and a2 confirm their mean redshifts at 2.225 whereas a3 and a4 have been identified on the basis of similar morphology using NIRC2 image and initial predictions from our lens model. The critical lines at $z = 2.225$ are shown in red and the corresponding caustics in yellow. System 10 has been identified as a separate system and included in our model with redshift as a free parameter. **Right:** Close-up image of the lensed arc to show smaller substructures used as constraints in our mass model. Each color corresponds to a different set of constraints, matched across in the two multiple images.

r_{core} is typically small and does not have any significant effect on modeling results (Covone et al. 2006; Elíasdóttir et al. 2007; Limousin et al. 2007), it was fixed to 0.15 kpc. We did not include the BCG in the scaling relations because it might have a significantly different mass to light ratio as a result of its distinct formation history. The BCG was therefore modelled as a potential with σ as the only free parameter. In total we had eight free parameters in our model all of which have broad uniform priors.

We make use of the spectroscopic information and imaging data to identify different multiple images of the lensed galaxy. The counterparts a3 and a4 to the lensed arc (Figure 2.3) have been identified on the basis of their image configuration and similar morphology to a1 and a2. Furthermore, high resolution NIRC2 image allows us to uniquely identify various features (systems 1-4 in Figure 2.3) within the lensed arc and match them across multiple images a1 and a2. These knots are used as constraints in our lens model (See Table 2.1). The lower magnification of a3, a4 does not allow us to resolve all the features in their counterparts a1 and a2 (for e.g. systems 1 and 3) even with the high resolution data.

The model is then computed as an iterative optimisation process. The constraints come from the location of multiply imaged systems, where a positional uncertainty of $0\overset{''}{.}1$ is considered. During the optimisation, LENSTOOL produces different MCMC realizations minimising the RMS between the observed and predicted positions of all images. An initial set of constraints is fed into LENSTOOL and a basic lens model is created, where many parameters are degenerate with each other. We then use it to test different assumptions on the multiply-imaged pairs and add new constraints to improve the optimisation of the model and break any degeneracies. For example, multiple image system 4 in Figure 2.3 was included as a constraint in the later stages of modeling with the help of our early lens model which confirmed its identification. We also include the location of a secondary lensed system (labelled 10 in Figure 2.3) as a constraint in our lens model and optimize its redshift during the lens modeling.

To better understand the effect of low resolution imaging data on the output mass model, we

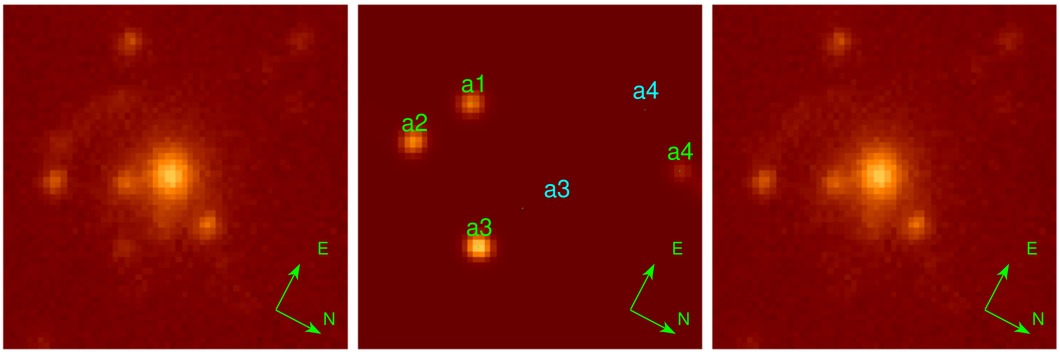

Figure 2.4 Lens model of CSWA128 based on SDSS imaging data. **Left:** Observed r-band SDSS image. **Middle:** Simulated image plane using the optimized lens model. First, the 'best' image plane positions predicted by the lens model are sent to the source plane. Then, using the barycentric source coordinates and a gaussian PSF with FWHM of 1.3", corresponding image positions (labelled in green) are predicted by the lens model. **Right:** Residual image. As clear, multiple image a4 is not bright enough to be detected in the SDSS data. Moreover, the multiple image locations a3, a4 (labelled in cyan) used as constraints in our final lens model (Figure 2.3) don't match with the predictions of this underconstrained SDSS model. Infact, NIRC2 data confirms that the predicted position of a3 actually coincides with a member galaxy of the lensing galaxy-group.

also carry out the modelling analysis using SDSS imaging data alone. In this case, our lens model utilizes limited constraints from a1 and a2 lensed images thus creating degeneracies in the optimized lens parameters. As shown in Figure 2.4, the image predictions by this under-constrained lens model show an inconsistency with the observations. We can easily see that there is a mismatch between the predictions of images and NIRC2 image constraints at a3 and a4. Therefore, unlike with NIRC2 data, it is practically impossible to use them as constraints to improve the optimization of the model and break any degeneracies.

Table 2.1 Constraints used in modeling cswa128, most of them are labelled in Figure 2.3. Not all the knots identified in a1 and a2 are resolved in the less magnified images a3 and a4.

Arc ID	R.A J2000 (deg)	Dec. J2000 (deg)	z
1.1	299.6462	59.8477	2.225 [2]
1.2	299.6483	59.8481	...
2.1	299.6459	59.8476	...
2.2	299.6486	59.8483	...
2.3	299.6515	59.8512	...
2.4	299.6459	59.8499	...
3.1	299.6457	59.8476	...
3.2	299.6488	59.8484	...
4.1	299.6461	59.8476	...
4.2	299.6485	59.8482	...
4.3	299.6515	59.8512	...
10.1	299.6524	59.8494	2.900 ± 0.25 [3]
10.2	299.6509	59.8483	...
10.3	299.6478	59.8469	...

2.4. Conclusions

The reliability of source-plane properties of lensed galaxies depends strongly on the accuracy of the lensing mass models used to interpret the high resolution observations. We use high resolution imaging data to identify additional substructures and construct a more robust map of the lensing potential of the galaxy group in cswa128 at $z = 0.214$. It is apparent that SDSS data lacks the required resolution and depth to identify different counterparts and arc substructures. This limits the accuracy of the model to interpret IFU observations. Using our modified model, we reach an astrometric precision of $0\farcs06$ in the predicted image positions. The mean flux magnification (measured by averaging the magnification for individual clumps constituting the arc) across a1 is $\mu_1 = 9.09 \pm 2.86$ and a2 is $\mu_2 = 11.56 \pm 5.98$.

In the next chapter, we analyze the physical properties of the source galaxy using a unique forward modelling approach based on this well-constrained lens model. We also compare the source-plane reconstruction obtained with the forward approach to that of traditional method to highlight the improvement in SNR and spatial resolution in the source plane.

[2] The redshifts of systems 1 - 4 are fixed to the spectroscopic redshift.
[3] The redshift of system 10 is optimized by the lens model.

CHAPTER 3

Pilot Study of $z \sim 2$ lensed galaxy: Source Reconstruction

This chapter has been previously published as 'High-resolution spatial analysis of a z ∼ 2 lensed galaxy using adaptive coadded source-plane reconstruction', Sharma, S., Richard, J., Yuan, T., et al. 2018, MNRAS, 481, 1427 .

3.1. Introduction

Lensing mass models play an important role in deriving the source plane properties of the background lensed galaxies. We derive the image to source plane mapping using the lens model described in Chapter 2 and correct IFU observations for lensing distortion. The focus of this chapter is mainly threefold: examine the source in terms of its morphology; derive kinematical patterns through velocity gradients and investigate chemical gradient through emission line ratios in the galaxy. In order to optimize the SNR of emission lines in the source plane, we merge the two independent observations, each from a different multiple image of the galaxy. The derived quantities from the coadded distribution undoubtedly provide a more reliable means to understand the physical conditions within the galaxy.

Using the lens model, we employ a forward modeling approach to combine the matching spaxels (which map to the same source position) from the two IFU datacubes. Then we fit the emission lines for the combined data to derive line fluxes, velocity, and velocity dispersion in the source plane. Moreover, since our technique is adapted to lens-model magnification, we are able to achieve enhanced Hα SNR at a resolution of ∼170 pc in highly magnified subregions of the source. We find that cswa128 is highly evident of a merging system.

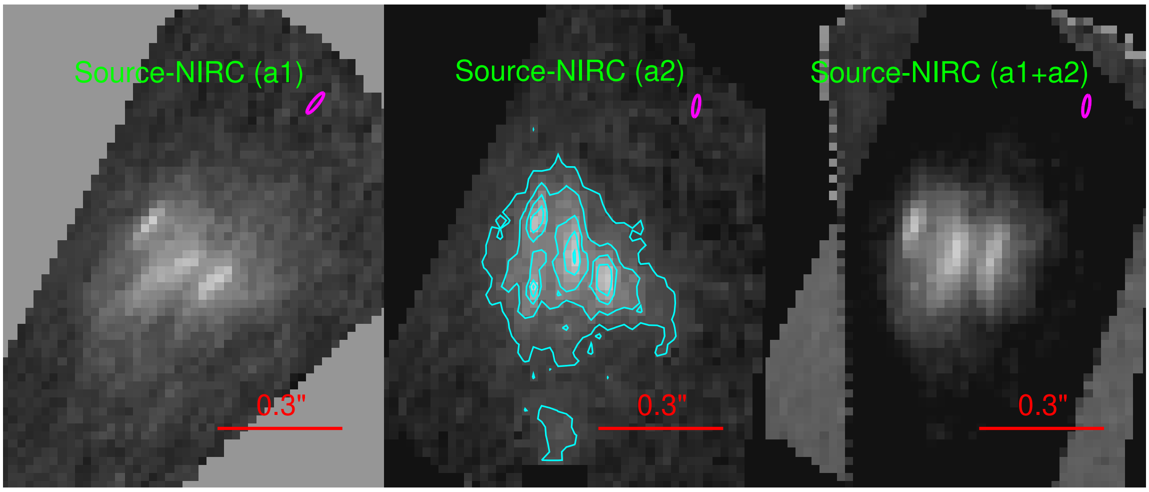

(a) Source Reconstruction of NIRC imaging data for each of the multiple images (a1, a2) of the lensed arc and their rendition into one frame using the best-fit lens model. Subsampling of 2 in source plane and 10 in the image plane is used to obtain a source-plane pixel size of 0.″02. The reconstructions are astrometrically aligned with the IFU - Hα source plane images shown in Figure 3.1b. Cyan contours highlight the different surface brightness levels of the source reconstructed a2 image of the lensed arc. Being the most magnified image of the galaxy, we use its contours to define the stellar emission from the galaxy. The last panel shows the combined source reconstructed image after manually adjusting the differences in position and orientation of a1 to match that of a2.

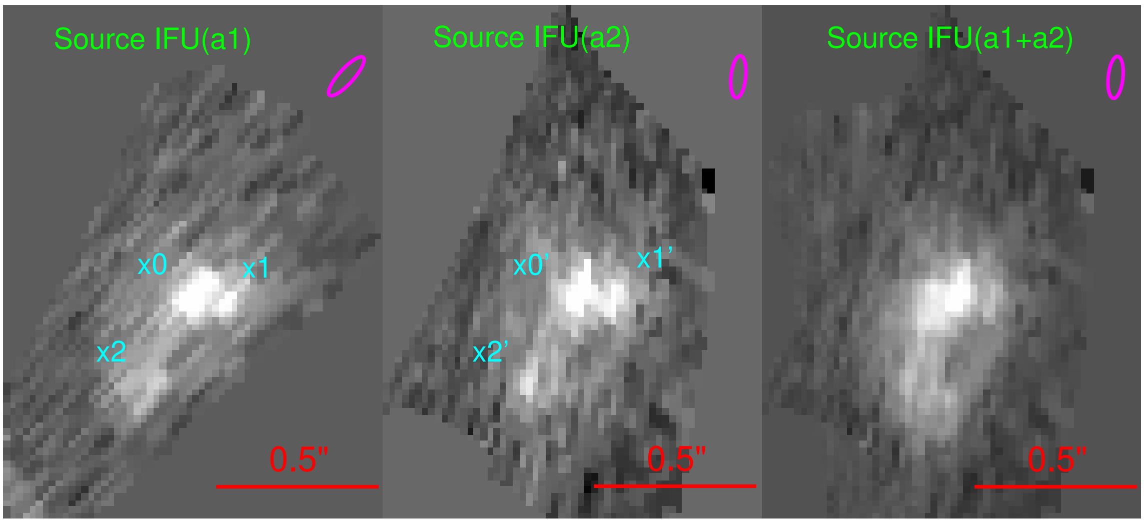

(b) Source Reconstruction of IFU data for each of the multiple images (a1, a2) of the lensed arc and their rendition into one frame using the best-fit lens model. About 6 datacube slices close to the redshifted Hα wavelength are stacked to form a co-added 2D image and then sent to the source plane. Subsampling of 5 in source plane and 10 in the image plane is used to obtain a source-plane pixel size of 0.″02. Clumps marked in cyan are matched across in the first two panels showing two independent reconstructions of the galaxy. The third panel shows the coadded image after manually adjusting the differences in position and orientation of a1 to match that of a2.

Figure 3.1 An example of source reconstructed stellar continuum from NIRC2 observations and Hα brightness distribution from IFU data for each of the magnified images (a1, a2) of the lensed arc and their rendition into a single frame to highlight the disadvantages of source-plane PSF. Magenta ellipses represent source-plane PSF's. As clear from the last image in both the panels, final merged image does not allow a significant improvement in SNR of different features labelled in cyan over individual reconstructions.

3.2. Traditional Ray Tracing Approach: Direct Image to Source Plane Mapping

We first use the *cleanlens* task in LENSTOOL[1] to convert the image plane maps to their corresponding source plane distributions. For each position in the image plane, this task computes the corresponding position in the source plane using the ray-tracing provided by our best-fit lensing model. We preserve the surface brightness to obtain the intrinsic source plane fluxes. The technical details of the *cleanlens* task alongwith an example of its implementation in LENSTOOL is explained in Appendix A. We use the *cleanlens* task with a sub-sampling of $ech = 10$ on the image and $sech = 2$ on the source plane for NIRC2 data or $sech = 5$ for IFU data. The source-plane reconstructions of NIRC2 imaging data and IFU data for lensed images a1 and a2 are shown in Figure 3.1.

This method breaks down as we proceed further with combining the individual reconstructions to obtain the overall source-plane profile. Because lensing preferentially shears the galaxy along a specific direction, there is a source-plane PSF (shown in magenta ellipses in Figure 3.1) associated with every reconstruction. The size of the source-plane PSF provides a reliable measure of the physical resolution we can achieve in the source plane. The orientation of the source-plane PSF is defined by the direction of lensing amplification. Reconstruction of different lensed images on the source plane will vary in their source-plane PSF's, both in size and orientation, making the co-adding a non-trivial problem. Traditionally, multiply lensed arcs were combined by a simple averaging after correcting for the offsets in position and PSF orientation (Yuan et al. 2017; Livermore et al. 2012; Sharon et al. 2012; Colley, Tyson & Turner 1996). However, as illustrated in Figure 3.1, a simple averaging of two images a1 and a2 will not provide an ideal improvement in the achievable SNR in the source plane, thus being of no significantly better use than the individual reconstructions.

3.3. Forward modeling Approach: Source to Image Plane Mapping

In this section, we describe our forward modelling approach to combine the IFU observations of two images (a1, a2) of cswa128. We ray-trace every spaxel from source to image plane at the location of two multiple images and convolve them with their respective image-plane PSFs (telescope+ seeing PSF, estimated from the observations). Following this technique, we generate a co-added 1-D spectrum for every source-plane spaxel by summing together the corresponding ray-traced spaxels convolved with the respective PSF's in the respective image-plane datacubes. This method not only circumvents the problem of combining different source plane PSF's but also provides a clever way to bin the image spaxels to maximize SNR in the source plane.

The overall procedure is outlined in the following steps:-

1. We use the *cleanlens* task of LENSTOOL with a grid over-sampling of $ech = 10$ on the image and $sech = 5$ on the source plane to create a template source plane frame.

[1] https://projets.lam.fr/projects/lenstool/wiki/LenstoolManual

The source plane pixel-scale after over-sampling is 0.″02. This template frame is only created for determining the source plane region that corresponds to the FOV of observations in the image plane.

2. Next, we create a series of source plane masks, each containing certain number of selected pixels. These masks, when added together cover adequately the entire region of the template source frame created in the previous step. The number of highlighted pixels in each mask depend on their location with respect to the caustic in the source plane. Because the source-plane pixels lying close to the caustic are highly magnified, they map to a larger part of image area. In such regions, we define masks of individual pixels whereas for regions with lower magnification, we increase the number of selected pixels. In low μ - high SNR regions of the data cube we resort to single pixel masks.

3. Each of the source plane masks are then sent to the image plane using LENSTOOL. The simulated image plane masks for each multiple image involve convolution by image PSF so that they can be directly compared with the observed images. We match the simulated masks with the observed datacubes to determine the image-plane spaxels ray traced from each of the source-plane masks.

4. This set of image plane pixels from the two IFU datacubes are then averaged together for each wavelength to create a 1D spectrum associated with every source plane mask.

5. Emission lines, Hα and [N II] are fit simultaneously for each 1D spectra following the same fitting procedure as described in section 2.2.2. We then manually inspect each fitted spectrum to reject spurious detections. We also note that the fitted parameters don't change significantly with a range of different initial conditions for the source plane spaxels in the fitting routine. We set a SNR cut of 5σ on Hα and 3σ on [N II] emission lines. If the achieved Hα SNR $< 5\sigma$ as a result of our fitting routine, we increase the size of our masks and repeat steps 1- 5. For source-plane pixels selected in more than one mask, we choose the fitting result with better Hα SNR.

We notice that a mask size of upto 5×5 pixels is sufficient to obtain an emission line fitting result of Hα SNR $\geq 5\sigma$ in different regions of the source. Using our adaptive forward modeling technique, we exploit the lensing amplification to optimize the spatial resolution in the source plane. This allows us to confidently analyse the dynamics of the lensed target which was previously limited only to the high SNR regions of the image plane.

In Figure 3.2, we compare the source reconstructions from our forward modeling technique with the traditional ray tracing methodology. We ray-trace the image plane fitted 2D Hα intensity map for multiple image a2 (as shown in Figure 2.2) and Hα SNR map back to the source plane and compare them to our coadded source plane reconstruction. As apparent in Figure 3.2, we are able to obtain a SNR improvement by a factor > 5 in the source plane. The improved SNR is achievable due to adaptively binning the image plane pixels, where the number of binned spaxels varies on the location of their corresponding source position. The forward modeling enables a relatively uniform PSF throughout the source-plane as compared to the variable PSF attained through traditional ray-tracing. We note that the image plane RMS of 0.″06 due to the lens model will translate into only small offsets between

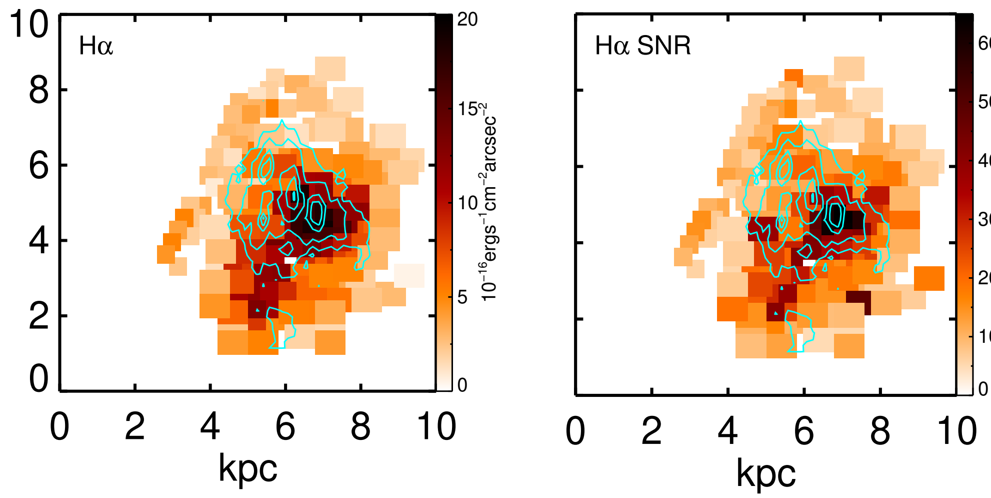

(a) Derived 2D Hα intensity in units of 10^{-16} erg s^{-1} cm^{2} arcsec^{-2} and SNR maps for combined source plane data using our forward-adaptive co-adding technique. Contours are the same as Figure 3.1.

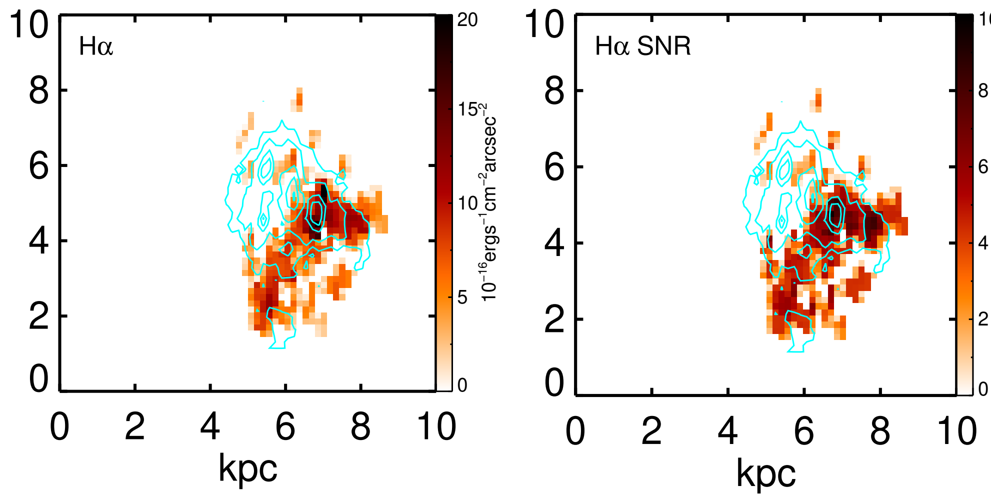

(b) Source reconstructed 2D Hα intensity in units of 10^{-16} erg s^{-1} cm^{2} arcsec^{-2} and SNR maps for multiple image a2 using traditional ray-tracing methodology. Contours are the same as Figure 3.1.

Figure 3.2 Comparing the 2D Hα intensity and SNR maps using (a) our forward coadded source-reconstruction with (b) the traditional ray tracing approach of multiple image a2 of cswa128. We obtain an SNR improvement of $6\times$ using our new approach. Figure also shows the difference in morphologies of the ionized gas emissions (as traced by Hα) and the stellar continuum (from NIRC2 observations) shown by cyan contours.

the co-added source plane locations of a1 and a2 which will not affect the reconstruction significantly.

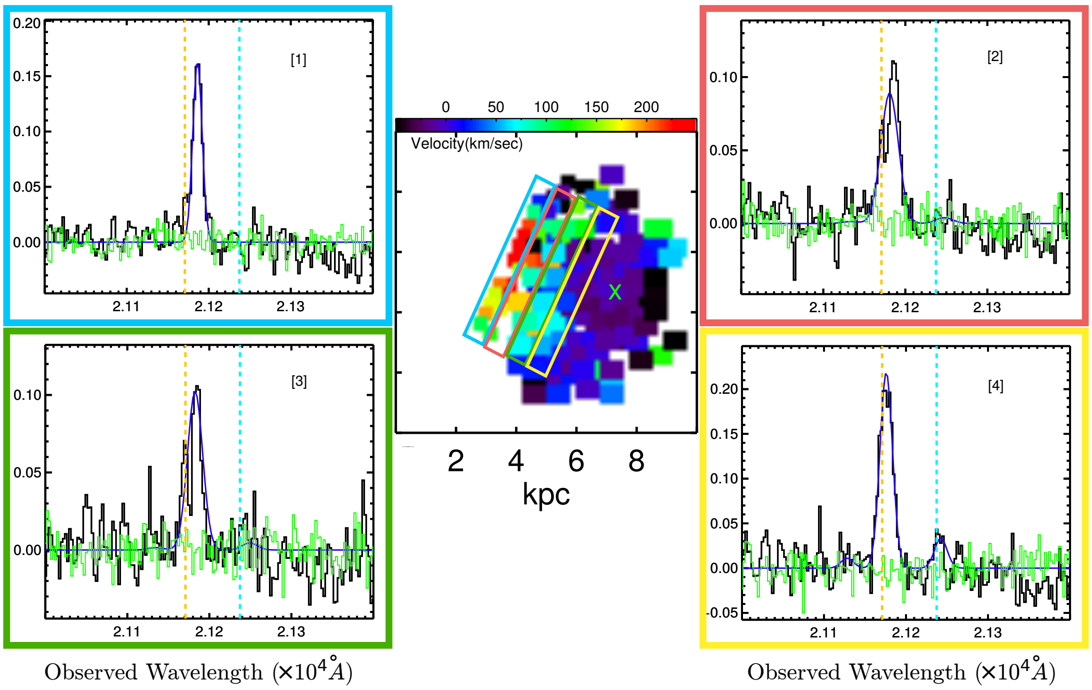

Figure 3.3 Derived source-plane 2D rotational velocity map and integrated 1D spectra of different source-plane regions using our forward-adaptive co-adding technique. The kinematical center ($z = 2.225$), shown by a green cross on 2D velocity map, is chosen to lie at the peak of Hα surface brightness distribution. The integrated spectra of different spaxels show a clear double peak as we move away from the center. The raw spectrum is plotted in black; RMS of sky residuals are plotted in green and gaussian fits to Hα and [N II] are shown in blue. Yellow and Cyan vertical lines in Panels 1-4 indicate the location of redshifted Hα and red [N II] emission lines at $z = 2.225$ respectively.

3.4. Source Properties

In the sections below, we discuss the source plane morphological and kinematical properties of cswa128.

3.4.1. Source Plane Morphology

We reconstruct the continuum image from NIRC2 observations using *cleanlens* task in LENSTOOL and present the source-plane morphology in Figure 3.1a. The reconstructed continuum intensity distribution, dominated by the stars in the galaxy, shows a clumpy structure. On the other hand, 2D source-plane Hα map (Figure 3.2) generated as a result of our forward modelling technique also shows a clumpy but more extended emission compared to the reconstructed continuum image of the lensed galaxy. As emphasized by previous studies (e.g Elmegreen et al. 2009; Förster Schreiber et al. 2011; Girard et al. 2018), clumpy morphology is commonly observed for high-z galaxies irrespective of their kinematical properties.

Our improved source-plane Hα morphology allows us to investigate the spatial distribution of the ionized gas emission in greater detail than before. We find that the reconstructed morphology of the ionized gas emission as traced with Hα differs significantly from the continuum emission, tracing the stellar structure of the lensed galaxy. As shown in Figure 3.2, we observe a clear mismatch in the location of the surface brightness peaks in the continuum and Hα maps. The spatial offsets between stellar continuum and ISM Hα gas have been previously observed in local luminous and ultra-luminous infrared galaxies dominated by merging events (e.g. Colina, Arribas & Monreal-Ibero 2005; Rodríguez-Zaurín et al. 2011; Barrera-Ballesteros et al. 2015).

3.4.2. Kinematics

The mismatch between stellar and ionised gas emission in cswa128 provides promising evidence for an ongoing merger. However, it is difficult to draw any conclusions about the disk/merger nature of high-z galaxies through morphology alone. Combining kinematics with morphology offers a distinct advantage to distinguish merger from isolated disks (e.g. Shapiro et al. 2008; Rodrigues et al. 2017; Yuan et al. 2017).

In this work, we acquire a much deeper understanding of the kinematical properties of cswa128 with the improved SNR of Hα and [N II] emission lines in the source plane, thanks to our forward modeling approach of combining the data from two different images of the galaxy. Our analysis indicates that the system is most likely undergoing a merging process. This result is consistent with the previous work by L16. This section outlines the different observations that led us to the above conclusion.

Figure 3.3 shows the 2D velocity map obtained as a result of our co-adding technique described in Section 3.3. The velocity gradient is highly inconsistent with a well-ordered rotating system. During the manual inspection of spectra, we notice a clear hint of double-peaked Hα emission in many spaxels, especially at the edges of the galaxy, indicating the presence of a merging pair in the system. This double peak signature was invisible in the previous study of this lensed system. We extract a 1D spectrum of different regions of the source-plane to show the presence of double-peaked Hα emission. As shown in Figure 3.3, the double-peaked emission is clearly visible as we move away from the kinematical center of the galaxy which is simply chosen to lie at the peak of Hα brightness distribution.

To further investigate the nature of the double peak, we refit Hα and [N II] emission lines, in the spectra of previously created masks but this time using double-gaussian profile each representing a different component of the emission. We refer to the two components as blue and red, in Hα and [N II] lines associated with every spaxel in the source plane. Because certain regions of the source-plane show quite a strong emission in one component than the other (see panels 1,4 in Figure 3.3), we define redshift ranges for the two components to allow the fitting routine to identify the correct one in the spectrum. Assisted by the initial 2D velocity map in Figure 3.3, we first associate the blue component with the disc and allow it to vary within ±80 km/sec of the kinematical center ($z \sim 2.225$). However on detailed investigation of individual spaxels at the edges of the galaxy, we find some spaxels showing emission bluer than the expected range, so we further extend the lower limit to -150 km/sec. Because the blue component gets weaker as we move away from the center of the galaxy, our preliminary analysis using a single component fit will only be dominated by the much stronger redder emission. The red component is used to fit any significant emission other

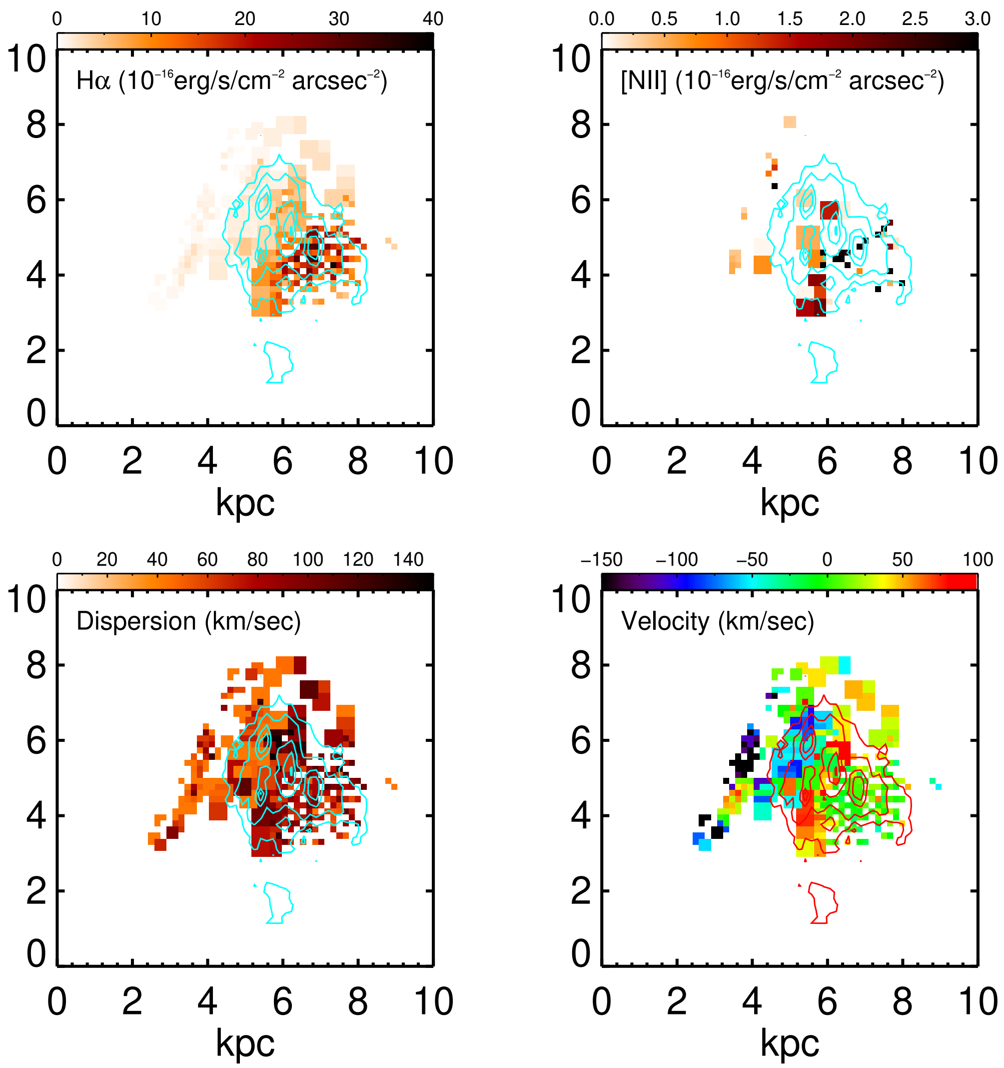

Figure 3.4 Derived source plane 2D maps for blue component of emission. The rotational velocity is calculated at the rest-frame of $z = 2.225$ and with respect to the kinematic center (green cross in Figure 3.3). Contours are the same as Figure 3.1.

than the blue component; quantitatively extending as ±150 km/sec of the redshift $z = 2.228$. Like before, [N II] (blue/red) SNR cutoff is set to 3σ. After visually inspecting the edgy spaxels, we identify Hα-blue SNR $\geq 3\sigma$ and Hα-red SNR $\geq 5\sigma$ as genuine detections.

The derived 2D maps for blue and red component are shown in Figure 3.4 and Figure 3.5 respectively. We find that the source-plane 2D velocity field for the blue component is highly disturbed and remains inconsistent with a rotating disk. The average velocity dispersions for the blue and red component are 69.9 ± 25.0 km/sec and 70.2 ± 21.5 km/sec respectively. This is in agreement with the observations of high-redshift mergers, further strengthening the merger scenario in cswa128.

3.4.3. Rest-Frame Emission Line Ratios

Figure 3.6 shows the derived 2D source-plane [N II]/Hα maps for the blue and red component of emission. The average log([N II]/Hα) for the blue and red components are respectively -0.56 ± 0.31 and -0.51 ± 0.29. With these ratios alone, we can not rule out contaminations

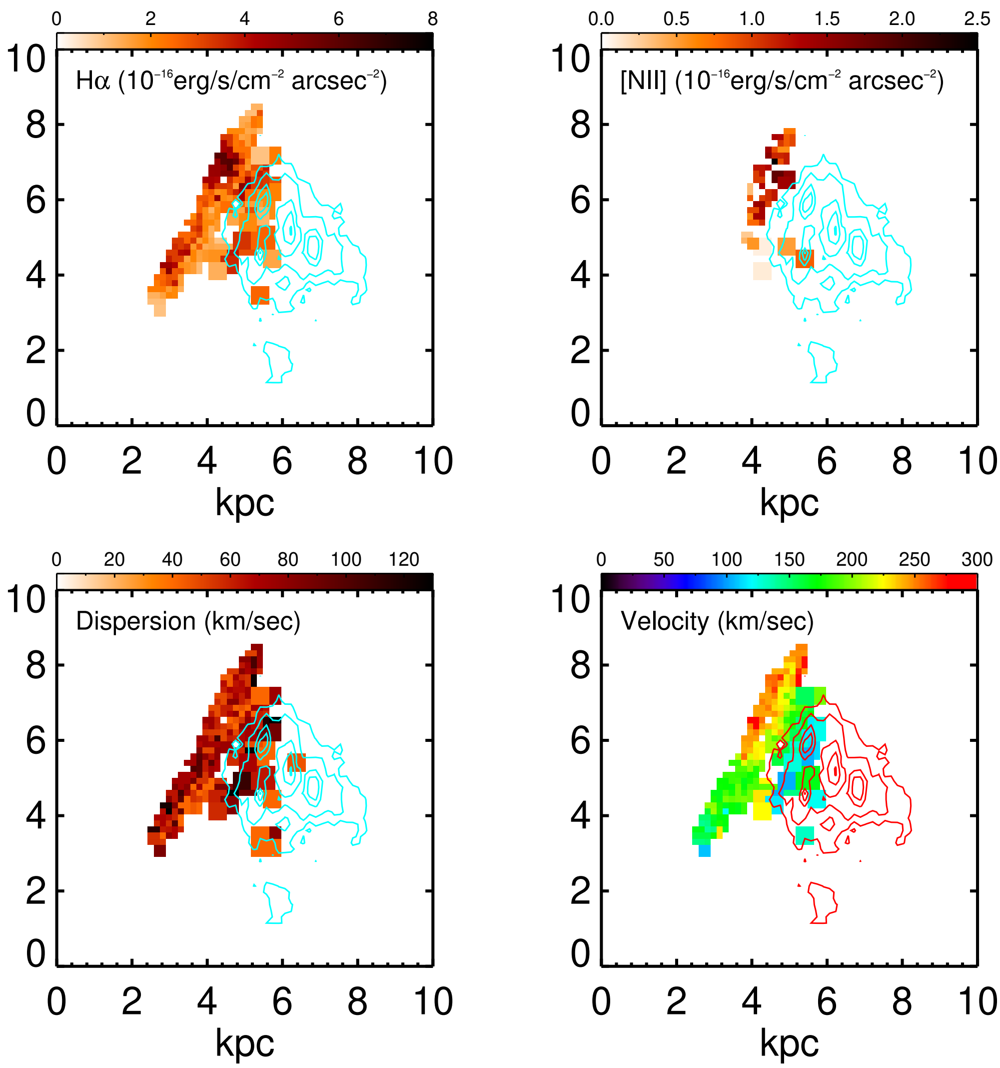

Figure 3.5 Derived source plane 2D maps for red component of emission. The rotational velocity is calculated at the rest-frame of $z = 2.225$ and with respect to the kinematic center (green cross in Figure 3.3). Contours are the same as Figure 3.1.

from shocks or AGN (Kewley et al. 2013). We therefore advise readers to interpret metallicity of this system with caution. Further observations including more line ratios such as [O III]/Hβ and [S II] will help to provide a more robust diagnostic for metallicity.

Further, we use the calibration of Pettini & Pagel (2004) to convert [N II]/Hα into metallicity. The correlation between metallicity and N2 ($\equiv \log([\text{N II}]\lambda6583/\text{H}\alpha)$) used is as follows :

$$12 + \log(\text{O/H}) = 8.90 + 0.57 \times \text{N2} \tag{3.1}$$

As shown in Figure 3.6 we observe flat metallicity gradients, a signature commonly observed in merging galaxies (Kewley et al. 2010; Wuyts et al. 2016; Cortijo-Ferrero et al. 2017; Wang et al. 2017). We notice that our metallicity distribution maps are limited by the low SNR of [N II] emission lines. Deeper IFS data is needed to better resolve [N II] and perform a detailed analysis of emission line ratios.

3.4.4. Spectral Energy Distribution fitting, Stellar Mass and Star formation Rate

We use the software LE PHARE (Ilbert et al. 2010) to perform SED fitting of the lensed system in cswa128. LE PHARE computes the best-fit SED based on population synthesis models by Bruzual & Charlot (2003). It uses a $\chi 2$ minimization procedure to provide the best-fit parameters such as stellar mass, SFR and extinction value. We fix the redshift to 2.22 and use the attenuation law by Calzetti et al. (2000) and IMF by Chabrier (2003). We use E (B -V) ranging from 0 to 2 and an exponentially decreasing SFR ($\propto e^{-t/\tau}$) with τ varying between 0 and 13 Gyr. We estimate the best fit stellar mass as $10^{10.4\pm0.3}$ $M_{\odot}$ and extinction E(B-V) = 0.4. The total SFR from the best-fit SED is 361 ± 411 $M_{\odot}$ yr^{-1}. All values have been corrected for lensing flux magnification. Because of limited photometric bands, LE PHARE obtains high uncertainties in SFR estimates from the SED fitting. Therefore we calculate dust-uncorrected SFR using total Hα emission as 201.92 ± 20.78 $M_{\odot}$ yr^{-1}. The total dust uncorrected SFR of cswa128 is ~ 3.5 times higher than typical star forming galaxies lying on the $z \sim 2$ mass-SFR relation (e.g. Zahid et al. 2012) of the main sequence. This is in agreement with the merger scenario also supported by the turbulent kinematics, double-peaked emission lines and the offsets between ionised gas and stellar continuum.

3.5. Conclusions

Along with a high resolution lens model described in Chapter 2, we present an adaptive forward modelling approach to combine observational data sets on different instances of the lensed arc. We resolve the structure and kinematics of the lensed target at scales of ~170 pc in the source plane. We are able to detect different velocity components of [N II] and Hα emission lines using this approach that are not seen in traditional source-plane coadding methods. We propose merger as the most plausible scenario in cswa128 on the basis of following observations:

1. **Morphology:** Offset between the clumpy stellar emission compared to the rather extended Hα morphology.

2. **Kinematics:** Chaotic velocity distribution with a clear double-peaked Hα emission possibly representing different components of merger.

3. **Chemical gradient:** Flat metallicity gradients derived from [N II]/Hα emission line ratios.

The results are consistent with the previous analysis by Leethochawalit et al. (2016). However, with the improved SNR of the emission lines in the source plane, we find more conclusive evidence of an ongoing merger in cswa128.

The forward modeling technique presented in this chapter has been developed specifically for this lensed target and required considerable manual intervention, especially in the construction of source masks. However, being computationally inexpensive, this approach offers a very quick and effective way of combining the data from multiple images to enhance the SNR of emission line maps in the source plane. We further develop this approach into a fully automated inversion of extended lensed images in a Bayesian manner. In the next

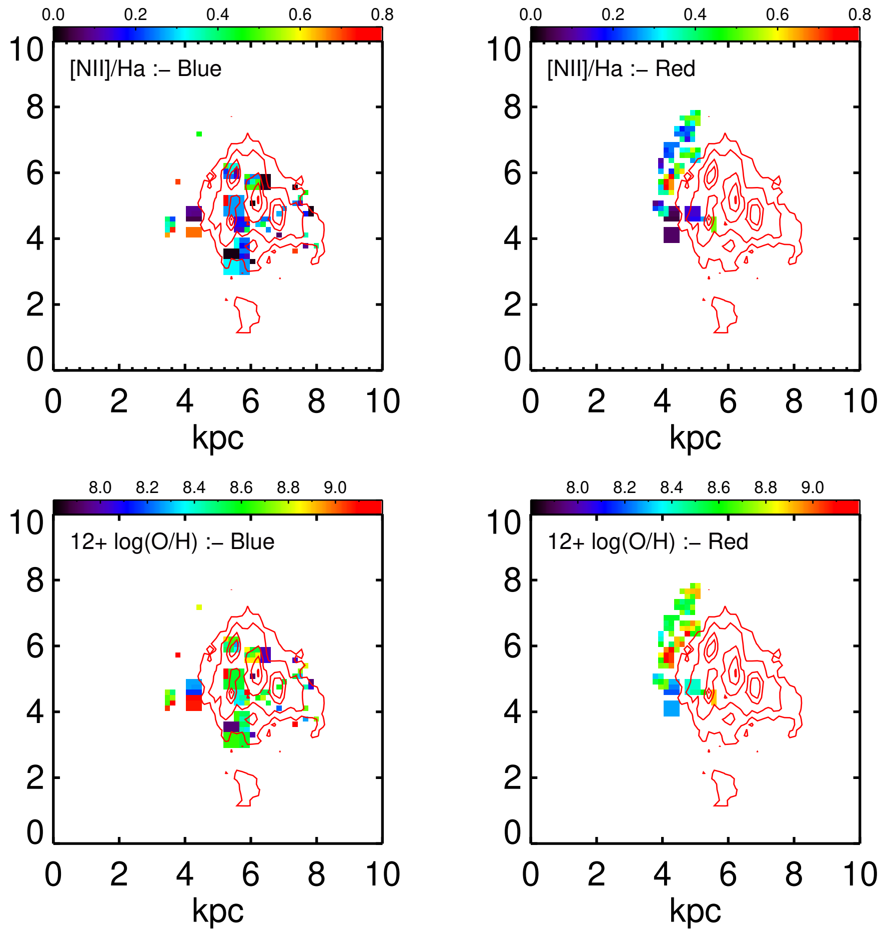

Figure 3.6 Derived 2D source-plane [N II]/Hα and metallicity maps for blue and red components of emission. Contours are the same as Figure 3.1.

chapter of my thesis, I outline our pixelated source reconstruction technique implemented in LENSTOOL.

CHAPTER 4

The Pixelated Forward Source Modelling in LENSTOOL

4.1. Introduction

Source reconstruction in LENSTOOL was so far limited to the following two techniques: a) *Traditional/Direct Reconstruction*: creates a de-lensed image of the source galaxy by means of backward ray-tracing using the lens model. As discussed in detail in Chapter 3, this method generates an effective source-plane PSF, below which structures remain undetected in the source-plane. b) *Parametric Reconstruction*: where an analytical profile (for e.g., Gaussian, moffat, sersic) described by a small number of parameters is fit to the image-plane data using constraints from the observed SBD while accounting for PSF smearing in the image plane. However, because this method relies on a parametrized shape of the source, it generally fails to address complex profiles, such as irregular, asymmetric or clumpy galaxies, where simple assumptions about the source morphology might not be justified.

In reality, giant lensed arcs at high redshifts can have complex SBD than simple source profiles such as Gaussian or sersic light distributions. A pixelated forward source modelling approach overcomes the challenges posed by the source plane PSF in the direct reconstruction methods, simultaneously allowing for unbiased reconstructions of irregular source morphologies. Therefore, I extend the forward approach described in Chapter 3 to implement an automated pixelated grid based source modelling procedure in LENSTOOL. This not only improves the effectiveness of our forward source modelling approach presented in Chapter 3 but also provides much higher flexibility and accuracy in modelling lensed galaxies.

The aim of a pixelated forward approach is simple: for a given lens model, utilize the constraints from the extended surface-brightness profile of the lensed source to optimize the intrinsic SBD on a pixel by pixel basis. This is usually done by minimizing a merit function e.g. χ^2. Various methods have been developed for the inversion of extended lensed images; more so for galaxy-scale lenses (Warren & Dye 2003; Claeskens et al. 2006; Brewer & Lewis 2006; Tagore & Keeton 2014; Nightingale, Dye & Massey 2018) compared to the more complex mass distributions of group scale/cluster lenses (Yang, Birrer & Treu 2020; Suyu et al. 2006). Most of the methods developed for galaxy-scale lenses, model the source light distribution and the lens model at the same time using Bayesian analysis. This is because the lens system can be generally described by a relatively simple mass model constructed with at most one or two sets of multiple images. As a result, the total number of free parameters/constraints in the system are few allowing computationally fast solutions. However, it becomes difficult to meet the demands for increased computational efficiency caused by the huge parameter space involved in the inversion of extended arcs lensed by more complex lensing distributions such as group scale/cluster lenses.

To solve the problem of high computing power in source-plane modelling of giant arcs, I keep the mass profile of the lens model fixed and only vary the source parameters - fluxes of individual pixels in the source-plane grid. I use a Bayesian Monte Carlo Markov Chain (MCMC) algorithm called Massive Inference (MassInf; part of the BAYESYS package in LENSTOOL Skilling 1998) to optimize the brightness of every pixel in the source-plane grid. The MassInf algorithm deals with the flux parameters of the pixelated source in a semi-analytical manner, thus making the procedure computationally cost-effective. The constraints come from the extended image plane distribution of the target galaxy. A weighting map is also supplied to LENSTOOL that accounts for the uncertainty in the observed data. I ensure regularization or smoothness in the source profile by allowing every grid-based pixel to be defined by a Gaussian radial basis function (RBF) of a known size. The Bayesian MCMC algorithm samples the posterior distribution and outputs a number of reconstructed source frames and their corresponding image reconstructions.

The full algorithm has been made publicly available in the latest version of the software LENSTOOL[1] for source plane reconstruction of strongly lensed galaxies. The development of the pixelated source modelling algorithm forms the core of this thesis. This chapter presents the details of the algorithm along with simulations used for testing the method. The structure of this chapter is as follows - Section 4.2 provides an overview of the algorithm and its implementation into LENSTOOL is described in Section 4.3. In Section 4.4, we describe the tests undertaken on simulated data to validate the algorithm with their results illustrated in Section 4.5. This section is followed by a conclusion (Section 4.6).

4.2. Basic Formalism

The description of the pixelized source reconstruction algorithm can be divided into two major steps: setting up a uniformly pixelated grid framework in the image and source planes and a Bayesian MCMC optimization procedure for optimizing the surface brightness in the source-plane. In this section, we overview these two key features of our source-reconstruction algorithm in detail.

4.2.1. Setting up grids using transformation matrix

The lens equation 1.2 describes the mapping from the source to the image plane i.e. using a given convergence map κ of the lens, it is possible to calculate the flux at each position β

[1] https://git-cral.univ-lyon1.fr/lenstool/lenstool

in the source plane knowing the flux at each position θ in the image plane. Therefore, we construct **s** and **I** as vectors representing the list of pixels in (a) the pixelated source grid we aim to reconstruct, and (b) the pixelated image plane corresponding to the observations. The pixelized source reconstruction algorithm treats the problem of source profile light estimation as a linear inverse problem. The linearity of lensing operator **L** ensures :

$$\mathbf{I} = \mathbf{L}\ \mathbf{s} \tag{4.1}$$

where **L** is completely determined by the known mass distribution of the lens (κ) which remains fixed and needs to be computed apriori. Further, we take into account the response of the instrument by a linear operator (**H**) that corresponds to the effect of convolution of the image by PSF. Then the above equation becomes:

$$\mathbf{I} = \mathbf{H}\ \mathbf{L}\ \mathbf{s} \tag{4.2}$$

where the convolution $\boldsymbol{H}\ \boldsymbol{L}$ is collectively referred to as the transformation matrix (**T**).

Every pixel in the source-plane grid is represented by a 2D Gaussian radial basis function (RBF) to smooth the otherwise discretely defined framework of the uniformly pixelized grid. Therefore **T** defines the mapping of every source pixel based RBF ray-traced to the image plane after PSF convolution. Finally, we consider white Gaussian noise vector (**N**) such that the observed image can be written as :

$$\mathbf{I} = \mathbf{T}\ \mathbf{s} + \mathbf{N} \tag{4.3}$$

4.2.2. Bayesian optimization

Once the transformation matrix, **T**, has been computed, we use a Bayesian optimization approach implemented by the MassInf algorithm (Bayesys manual, Skilling 1998), to solve for the counts in the source pixels, denoted by vector **s** in equation 4.3. The Bayesian approach in LENSTOOL effectively samples the parameter space, at the same time providing reliable uncertainties in the free parameters - the brightness of each pixel in the source grid. In particular, the MassInf algorithm uses a Gibbs sampling approach to effectively sample a huge parameter space. It explores the correlations of the most relevant parameters in the model thus making the optimization procedure computationally cost-effective.

The Bayesian approach implements two levels of inference - parameter space exploration and model comparison. Mathematically, parameter exploration requires the unnormalised posterior Probability Density Function (PDF; equal to the product of the likelihood and the prior). The second level is achieved using the normalization of posterior also called as evidence. Bayes' theorem provides a relation between all these quantities as follows:

$$P(s|D) = \frac{Pr(s) * P(D|s)}{P(D)} \tag{4.4}$$

where P(s | D) is the posterior PDF, P(D | s) is the likelihood of getting the observed data given the source s, Pr(s) is the prior PDF for the source brightness and P(D) is the evidence. A $\chi 2$ estimator is constructed to quantify how well each trial image reconstruction fits the observational data :

$$\chi^2 = \sum_{i,j} \frac{(O_{ij}^2 - D_{ij}^2)}{\sigma_{ij}^2} \tag{4.5}$$

where $\mathbf{O}_{ij}$ is the reconstructed , $\mathbf{D}_{ij}$ is the observed brightness of the (i,j) pixel in the image plane and σ_{ij} is the associated weight map. The likelihood function associated with $\chi 2$ is :

$$P(D|s) = \frac{1}{Z_l} exp - \frac{\chi 2}{2} \tag{4.6}$$

where $Z_l = \prod \sqrt{2\pi\sigma_{ij}}$ is a dimensionless normalization. Here, we assume that the resulting source distribution has to be positive everywhere. This is well described by a Poisson prior on source counts as :

$$Pr(s_{ij}) = exp(-s_{ij}^2/q)/q \tag{4.7}$$

where q is a dimensional unit of flux and a nuisance parameter with a PDF given by :

$$\pi(q) = q_0^2 q e^{-q/q_0} \tag{4.8}$$

The $x\, e^{-x}$ form has been chosen to keep the expression tractable analytically while keeping q away from 0 and ∞. The parameter q_0 is fixed and specified by the user to LENSTOOL. Since it is shown to have a little impact on the final reconstruction (Jullo et al. 2014), we fix $q_0 = 10$ in our simulations. The number of RBFs (n) is another nuisance parameter estimated by the sampler to reproduce the data. Prior on n is best described by a geometric PDF:

$$Pr(n) = (1-c)c^{n-1} \; where \quad c = \frac{\alpha}{\alpha+1} \tag{4.9}$$

and $\alpha = 2\%$ of the total number of RBFs. Again, like q_0, α does not change the reconstruction significantly (Jullo et al. 2014).

According to a user defined source model parameter space, the MCMC sampler randomly draws mock models and computes their χ^2. Progressively, the Bayesian MCMC sampler converges to the best fit parameter space with the highest posterior PDF and randomly draws some realizations in this parameter space. The evidence is required to characterize our confidence in the model we optimize. The evidence works as Occam's razor i.e. a simple model with few free parameters will have higher evidence as compared to a complex model giving the same fit. As a result, we have a number (set to 200) of reconstructed source frames and their corresponding image planes. We average these sampled frames and construct the 'best' reconstruction.

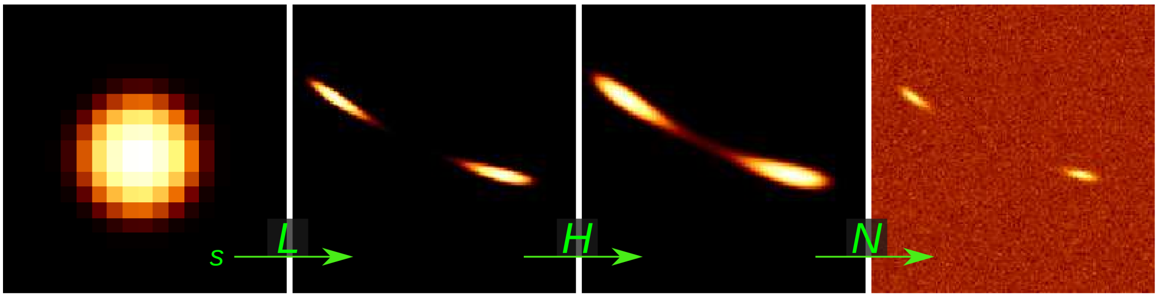

(a) Different vectors as shown in equation 4.3. Starting from left: true source, model image after applying lensing vector **L**, application of PSF vector **H**, addition of noise vector **N**.

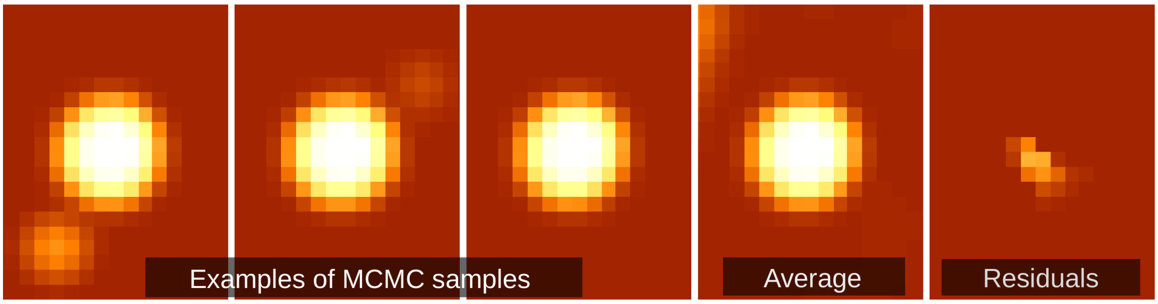

(b) Starting from left: Reconstructed source frames returned by the Bayesian MCMC sampler, best source reconstruction after averaging all MCMC samples, source-plane residuals.

Figure 4.1 Illustration of the pixelated algorithm using an example of a Gaussian profile in the source plane.

4.3. Implementation in LENSTOOL

The code implementing the pixelated grid algorithm is fully automated and is publicly available as a part of LENSTOOL[2]. In this section, I highlight the different portions of the code that were specifically developed as a part of this thesis to implement the two key features of the pixelized grid algorithm explained in Section 4.2.

The transformation matrix, as described in Section 4.2.1, is produced apriori and remains fixed throughout the optimization process. In the code, the function - *precompsource* produces the transformation matrix (variable *fluxmap* in the code). Following equation 4.3, 2D weight map, **N**, is supplied to LENSTOOL as $1/\sigma_{ij}^2$, where σ_{ij} (variable *wframe* in the code) is the noise standard deviation in the lensed image. Typically the noise is uniform across the FoV but could vary as well due to differences in exposure times across different parts of the image. To specify **H** vector in equation 4.3, we provide the width of a PSF profile (or just the PSF profile itself) that has been estimated through observations. Another parameter, the FWHM of Gaussian RBF is given by the user and stored as the variable *rbfsig* in the code. The function *testpixel* in the code computes an image pixel frame using the source pixel-frame and *fluxmap* matrix as described by equation 4.2. Main functions that had been modified or newly introduced as a part of the pixelated modellling code are listed in Table 4.1.

[2] http://projects.lam.fr/projects/lenstool

All these input parameters are specified to LENSTOOL as keywords in a parameter file. The section of the parameter file that computes source reconstruction procedure is *cleanlens*. The pixelated algorithm, in particular, is initiated using the keyword *cleanset = 4* and has been developed into a working code in this thesis. Further details about these keywords and their usage is shown with an example of a parameter file given in Appendix A.

The second part of the formalism iteratively applies the transformation matrix to the model source grid within a bayesian framework such that it best reproduces the observed image plane fluxes. As mentioned in Section 4.2.2, I utilize the MassInf algorithm to implement Bayesian MCMC optimization of the source-plane fluxes. This algorithm provides a computationally effective way to solve for linear data with Gaussian errors using input priors, as detailed in Section 4.2.2. The performance of the MassInf algorithm in handling a large parameter space has been previously seen in another application of LENSTOOL that maps the weak lensing mass distribution through a multi-scale grid of RBF's (Jauzac et al. 2015, 2012). I have implemented the MassInf optimization to be specifically suitable for optimizing the source-plane profiles of lensed galaxies.

Table 4.1 Newly added/modified functions committed to the publicly accessible LENSTOOL code to implement the pixelated source reconstruction algorithm.

Name of the function	Purpose	Formalism
precompsource()	Create **T**	Transformation Matrix ($\mathbf{T} = \boldsymbol{H}\,\boldsymbol{L}$)
d_rbf()	Convolve the source grid with RBF FWHM	
testpixel()	Compute **I** given **s** & **T**	Equation 4.2
o_run_bayes()	Initialize variables for MassInf optimization Set nuisance parameters q_0 and α	Equations 4.8 & 4.9
UserMontitor()	Launch optimization in MassInf setting	Transformation Matrix
o_chires()	Compute $\chi 2$	Equation 4.5

In Figure 4.1, the application of the pixelated algorithm is shown for a mock source model - a Gaussian profile in the source plane. The figure highlights the outputs from different stages of the algorithm including the effect of the transformation matrix and the reconstructed frames returned by the MCMC sampler. In this simulation, we are able to recover the light profile in the central region of the source, where the flux is larger, with less than 5 % error.

Regarding the computational cost, while direct ray-tracing runs in less than a second, a test run of the pixelated algorithm for an example shown in Figure 4.1 on a 100×100 grid will scale between dozens minutes to an hour. In general, when estimating large source light profiles on a larger grid can result in an increase in this value by 4-5 times. While this is a current limitation of the algorithm, we are confident that the implementation of more sophisticated packages for linear optimization will decrease the computational time needed by the algorithm.

4.4. Simulations

We apply the algorithm to simulated data and compare the results to those obtained with traditional ray-tracing techniques. Using the simulations, we are able to quantify the effect of varying SNR of image plane data, Gaussian PSF width, Gaussian RBF width, source pixel size on the reconstruction obtained using the pixelated algorithm. In these simulations, we assume a fixed mass profile (or lens model) with different kinds of model profiles - one Gaussian, two Gaussians - overlapping and non-overlapping in the source plane. For simplicity purposes, the lens model is the same as the one developed for the galaxy group in cswa128 and source redshift is set to 2.225. In all our simulations, pixel size in the source plane is half of that in the image plane.

We begin with a model source which is ray-traced to the image plane after convolving with a known PSF size and random noise of a given standard deviation to obtain the corresponding model image. Next, this model image is supplied to LENSTOOL using a parameter file that describes the optimized parameters of the lens model along with the PSF width, standard deviation of noise and Gaussian RBF size. Finally, the reconstructed source is compared to the model source using RMS error that is determined by summing over all pixels with surface brightness greater than 1% of the peak source brightness. The threshold of 1% excludes the contribution of low surface brightness pixels (probably at the tail of the Gaussian profile) in affecting the value of the RMS error. We use the RMS error in the source plane as a quantitative measure of the performance of the algorithm. To validate our results, we repeat these simulations 20 times and report the mean and standard deviation of the final RMS error for all our test cases.

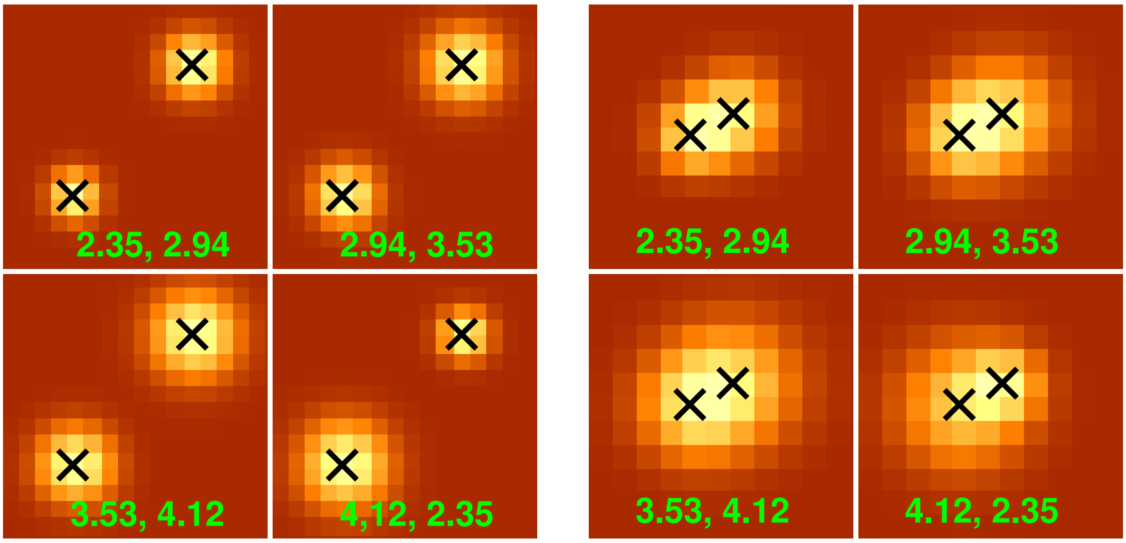

Figure 4.2 Double Gaussian source profiles used for testing the pixelated algorithm. Every source profile constitutes of two different Gaussians with the ratio of their standard deviation σ to source pixel size chosen from 1, 1.25, 1.5, 2.0. Black crosses represent the centers of member Gaussians in the profile. Ratios of FWHM ($\sim 2.35 \times \sigma$) to the source-plane sampling for both the Gaussians are listed in green. We split these sources into two different categories depending on the separation between their centers. **Left:** Centers of two Gaussians are separated from each other. **Right:** Centers of two Gaussians are closely spaced causing them to overlap each other.

4.4.1. One Gaussian Tests

In order to make our simulations independent of the source-pixel size, we choose FWHM of each Gaussian to be a factor of the sampling in the source-plane. Specifically, we allow σ to vary between (1, 1.25, 1.5, 1.75) $\times$ source pixel size. Given the background Gaussian source, we obtain the true lensed image with a pixel scale of $0\farcs1$. This pixel scale has been chosen to reproduce mock HST like spatial resolution. Thereafter, the Gaussian PSF of varying FWHM i.e. (2.0, 2.5, 3.0) × image pixel size is convolved with true lensed images to simulate HST quality of data. For comparison, the typical size of HST PSF is roughly 1.5 -2 times the spatial resolution of data as represented by our simulations. Lastly, Gaussian noise of different standard deviation is added to simulate the test cases that represent peak SNR of 20, 10, 5, 3 in the final model image.

4.4.2. Two Gaussian Tests

To validate the application of pixelated algorithm on more complex sources, we test it on source profiles consisting of two Gaussians in the source plane. We vary the separation and the size of member Gaussians and construct sources which have: a) widely separated Gaussians, and b) overlapping Gaussians. The double Gaussian source profiles used in our simulations are summarized in Figure 4.2. Moreover, we choose the values of PSF widths and Gaussian noise as those in single Gaussian tests to compare the trends in the RMS error across simulations.

Figure 4.3 compares the reconstructed output computed by the pixelated algorithm with the traditional method for one of the source profiles shown in Figure 4.2. As it is clear from the top panel, the residuals in the image plane are consistent with the added noise in the true image. The middle and bottom panels show a direct comparison of the source profiles reconstructed using the pixelated and traditional approaches respectively. We obtain an improvement by a factor of 5 in the source plane RMS error using the pixelated source modelling technique.

4.5. Simulation Results

Through these simulations, we will investigate whether the pixelated algorithm is able to recover the true source profile when reconstructing the mock images described in the previous section. In particular, we study the effect of SNR and PSF width in the image plane on the final source plane reconstruction modelled by the pixelated technique. We also compare the output source-plane RMS error in both the scenarios - pixelated and direct reconstruction for all the source profiles.

4.5.1. Effect of PSF

At a fixed peak SNR in the image plane data, we calculate the source-plane RMS error as a function of the size of the Gaussian RBF for profiles reconstructed using the pixelated technique. In this chapter, we only present the results for overlapping double Gaussian source profiles in Figure 4.4. Similar results for single Gaussian and non-overlapping double Gaussians are shown in Appendix B. As expected, the source-plane RMS error increases with increasing PSF width in the image plane data. Moreover, Figure 4.4 shows that the best case RBF width for which we obtain minimum RMS error depends on the size of the Gaussians in the true source. Theoretically, we would expect the RBF size to match the FWHM of the Gaussian in single Gaussian tests or that of the smallest Gaussian in the

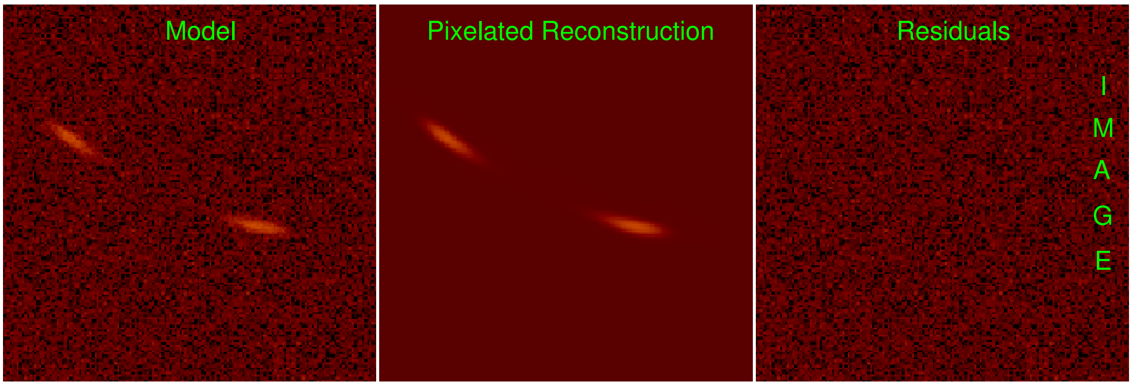

(a) Starting from left: True image, pixelated reconstruction, residuals in the lensed plane.

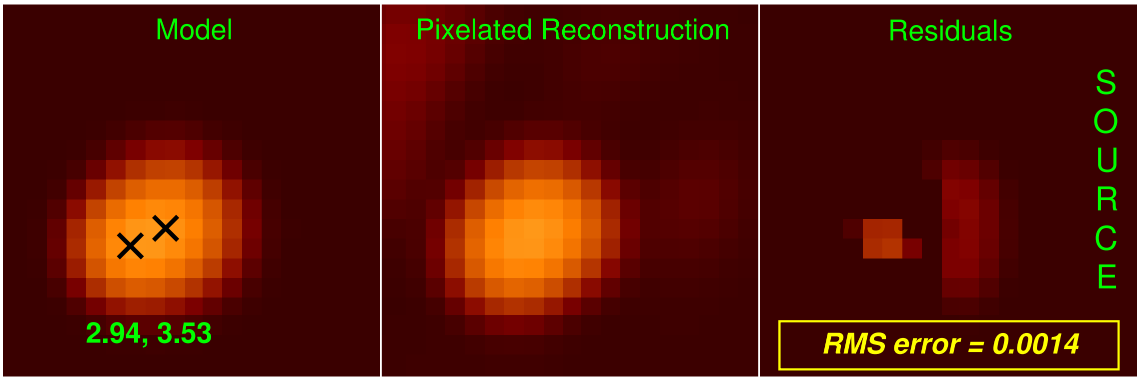

(b) Starting from left: True source, pixelated reconstruction, residuals in the unlensed plane.

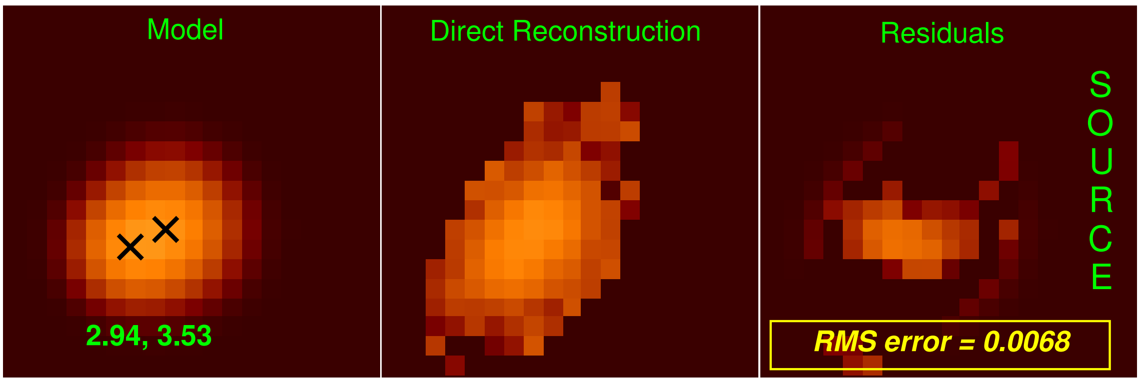

(c) Starting from left: true source, direct reconstruction, residuals in the unlensed plane.

Figure 4.3 Pixelated vs direct reconstruction for a double Gaussian source profile with σ's equal to 1.25 and 1.5 $\times$ pixel size in the source plane. Black crosses in the source model represent the centers of member Gaussians in the profile with the ratios of FWHM ($\sim 2.35 \times \sigma$) to the source-plane sampling listed in green. Standard deviation of Gaussian PSF used to create model image is $0.''1$ or 2.5 $\times$ image plane sampling. Gaussian noise added to the lensed image results in a peak SNR of 10 in the image plane. Standard deviation of "best" Gaussian RBF is 3.25 $\times$ pixel size in the source plane as it results in minimum $\chi 2$ during MCMC optimization. As shown at the bottom of the source plane residuals, there is an improvement by a factor of 5 in the RMS error for the reconstruction computed using the pixelated approach.

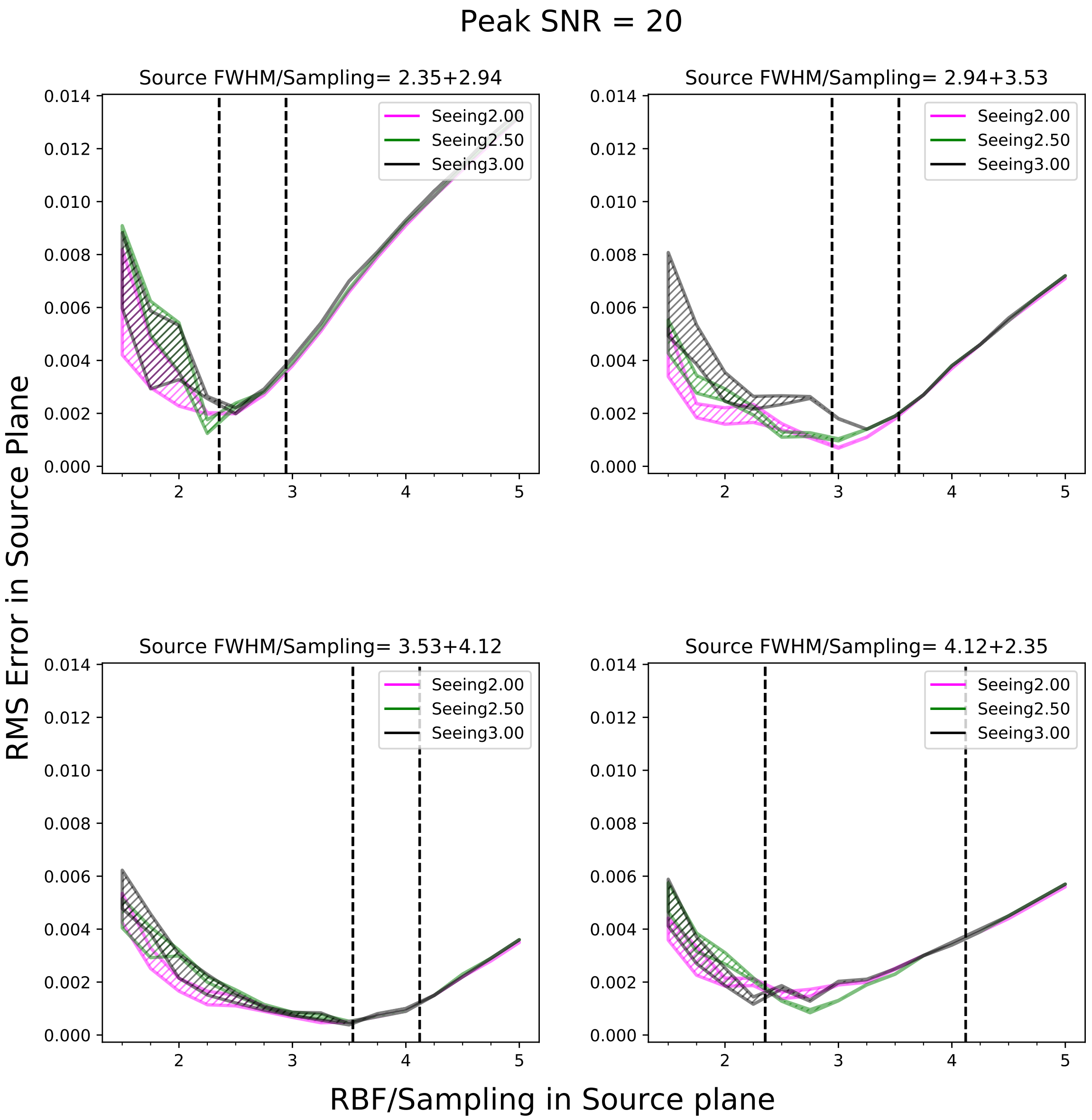

Figure 4.4 Source-plane RMS error as a function of RBF widths for overlapping double Gaussian source models for a fixed peak SNR of 20 in the image plane. Different colors represent trends for different values of FWHM of Gaussian PSF i.e. (2.0, 2.5, 3.0) $\times$ image pixel size. Shaded regions show 1 σ error bars in the RMS error calculated by repeating a single simulation 20 times. Dashed vertical lines show values of FWHM of member gaussians in every source model.

double Gaussian profile. As clear from these figures, this has been consistently observed in all our tests.

4.5.2. Effect of SNR

We also quantify the impact of changing SNR in the observed data on the final RMS error obtained in the source plane reconstructed using the pixelated method. Figure B.3, Figure B.4 and Figure 4.5 summarize the results for different types of Gaussian source profiles. On average, an increase in the source-plane RMS error can be clearly observed with decreasing

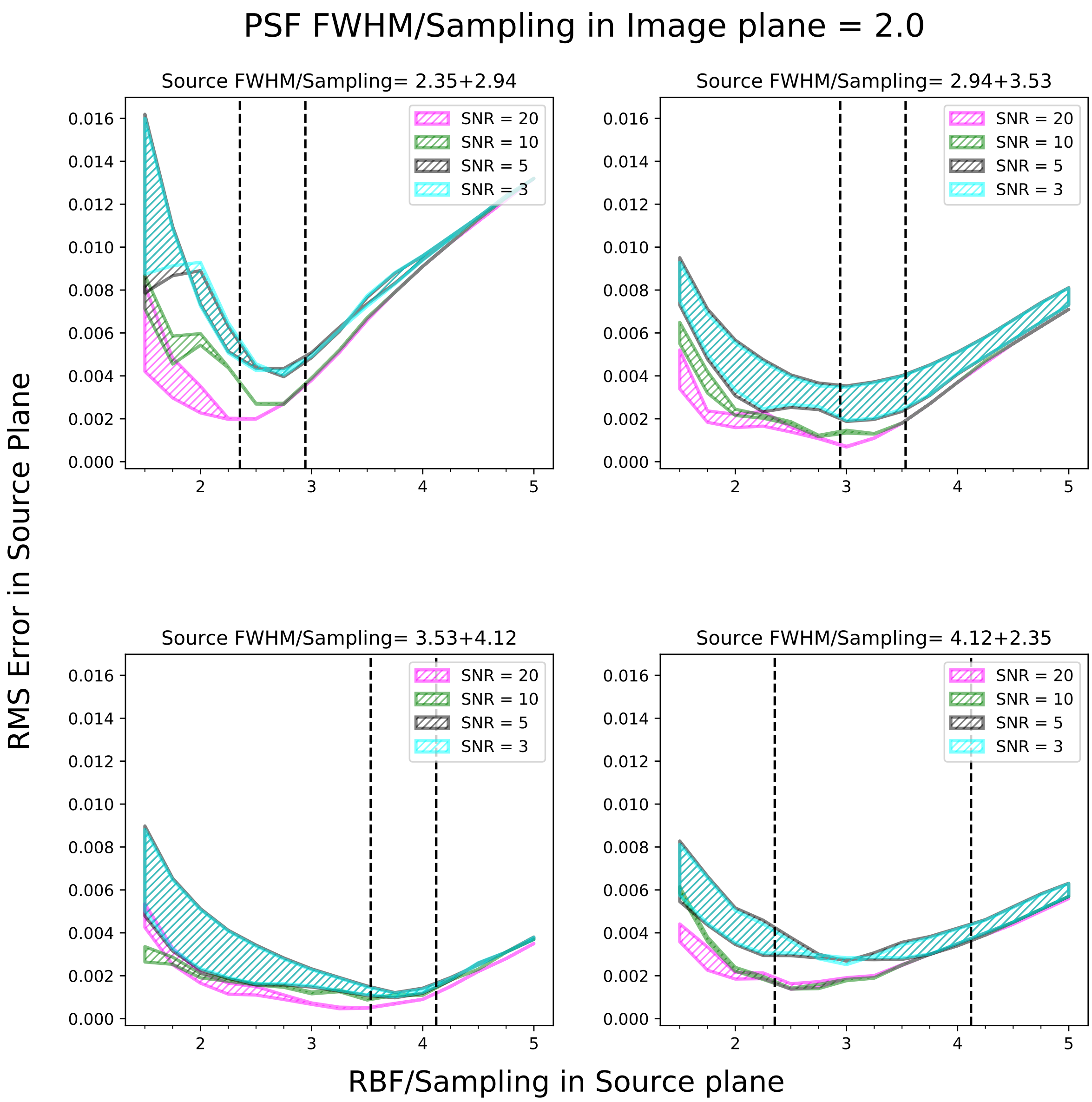

Figure 4.5 Source-plane RMS error as a function of RBF widths for overlapping double Gaussian source models for a fixed ratio of PSF FWHM / Image plane sampling = 2.0. Different colors represent trends for different values of peak SNR i.e. (20, 10, 5, 3) in the image plane. Shaded regions show 1 σ error bars in the RMS error calculated by repeating a single simulation 20 times. Dashed vertical lines show values of FWHM of member gaussians in every source model.

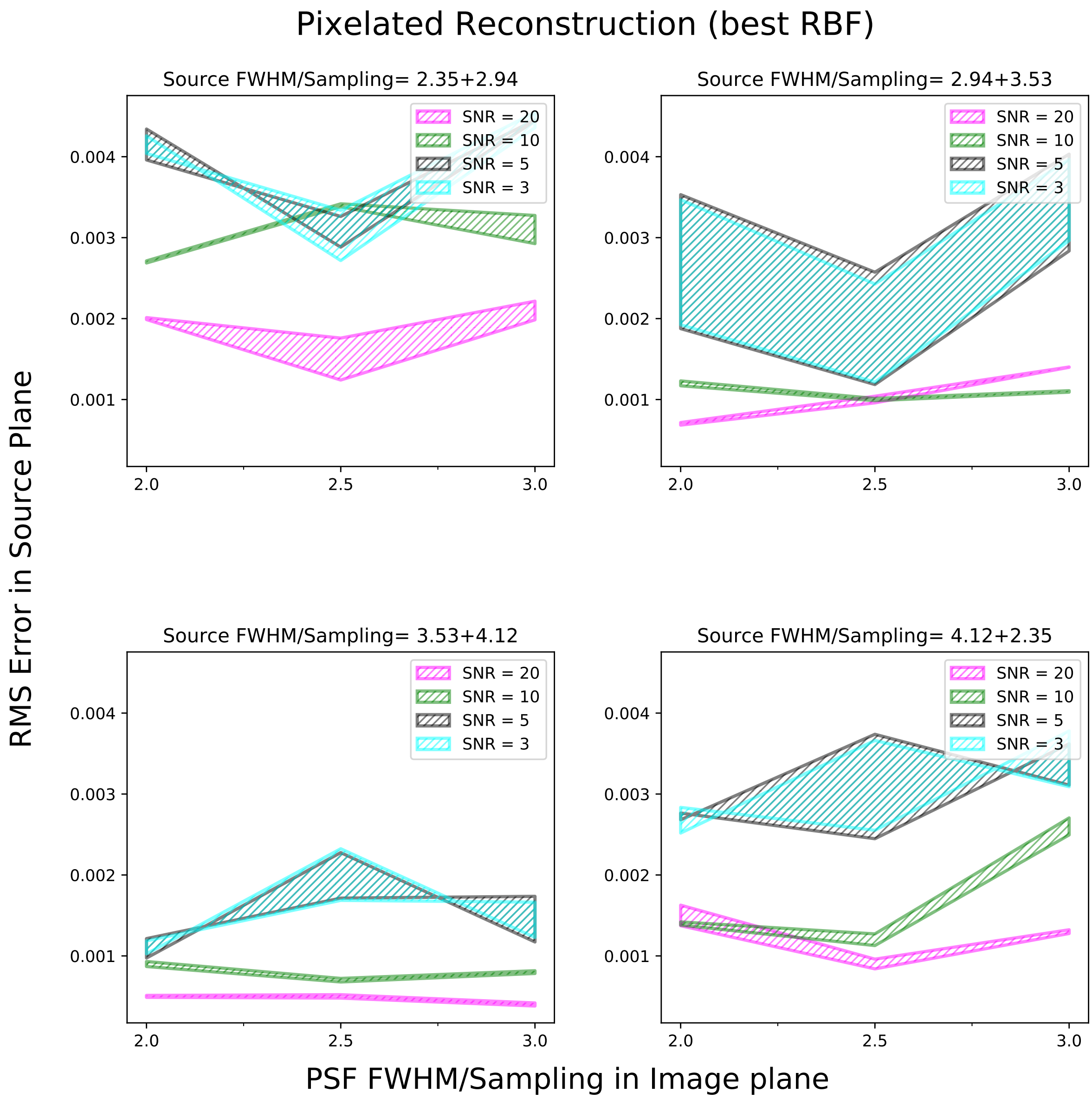

Figure 4.6 Source-plane RMS error computed on overlapping double Gaussian source profiles reconstructed with pixelated modelling technique as a function of the ratio of PSF FWHM to image plane sampling at the "best" RBF size. FWHM of "best" Gaussian RBF for every test case is chosen such that the image plane $\chi 2$ for that RBF value is minimum during Bayesian optimization. Different colors represent trends for different values of Peak SNR in the image plane. Shaded regions show 1 σ error bars in the source plane RMS error calculated by repeating a single simulation 20 times.

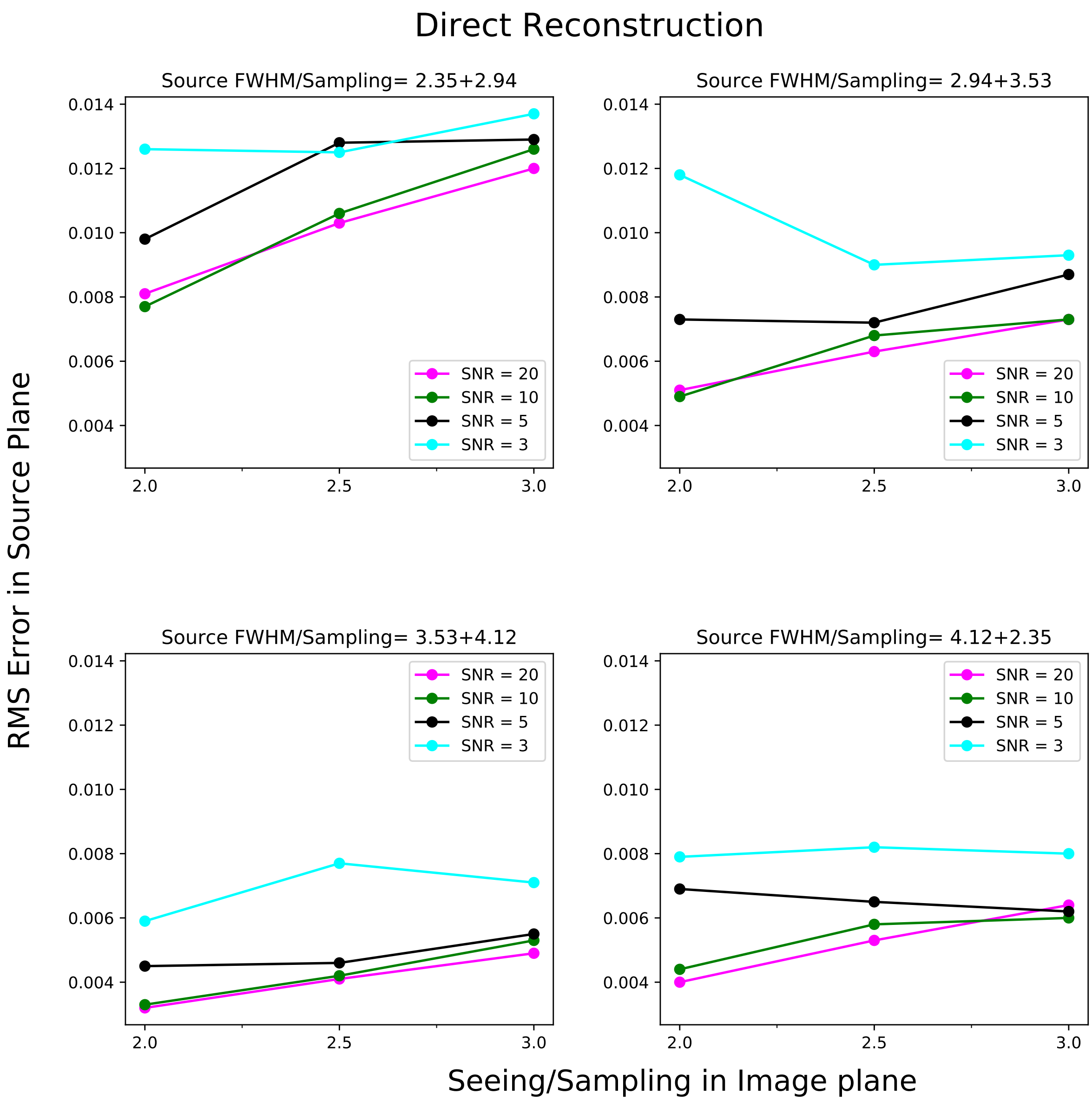

Figure 4.7 Source-plane RMS error computed on overlapping double Gaussian source profiles reconstructed with direct ray-tracing as a function of the ratio of PSF FWHM to image plane sampling. Different colors represent trends for different values of Peak SNR in the image plane..

peak SNR values in the corresponding image plane data. Moreover, as is the case with the PSF FWHM, the lowest value of source-plane error is achieved at a RBF width close to the FWHM of the smallest Gaussian in the respective source model profile. The performance of the pixelated method across the Gaussian source profile also varies : we observe higher source-plane RMS error for single Gaussians as compared to double Gaussian profiles.

We also compare the SNR trends obtained via the two techniques for overlapping double Gaussian sources in Figures 4.6 and 4.7. While we roughly observe the source-plane RMS error to increase with increasing PSF width or decreasing peak SNR in the image plane, the maximum value of RMS error at a given FWHM of the Gaussian PSF can reach upto $\sim 5-6$ $\times$ the RMS error of the same source calculated using pixelated method of reconstruction. Similar results have been achieved for other source profiles used for testing the algorithm as shown in Appendix B (Figures B.5 - B.8).

4.6. Conclusions

The pixelated algorithm in LENSTOOL allows detailed modelling of the source in the unlensed plane without any prior or assumption about the source light profile. We tested the algorithm on a variety of source profiles and provided a detailed comparison with the reconstruction obtained from ray-tracing techniques. We quantified the performance of the algorithm using the source-plane RMS error which shows that the pixelated method consistently results in significantly lower RMS errors (upto a factor of 5) than the traditional method of reconstruction. Using the mock data, we showed that our pixelated source modelling algorithm finds a reliable solution even in complex cases such as close compact sources. Hence, the pixelated algorithm is both robust and flexible in source delensing and deconvolves the effects of lensing PSF from the source plane reconstruction.

To validate the algorithm using more realistic simulations of high-z galaxies, our future work will involve the application of the pixelated algorithm on inputs from cosmological simulations such as Bournaud & Elmegreen (2009); Mayer et al. (2016), Faure et al submitted. The idea is to ray-trace the lensed galaxies to the image-plane and compare the reconstructions to recover clump locations, physical sizes etc. A detailed analysis of such tests will be a part of my future work with simulations. In the next chapter, we discuss the application of the pixelated technique on the specific case of cswa128 to demonstrate the gain in information that can be achieved after removing PSF effects from the source reconstruction of a real lensed high-z galaxy.

CHAPTER 5

Testing the Pixelated Approach - Resolving star-forming clumps in cswa128

5.1. Introduction

The pixelated forward source modelling technique described in Chapter 4 adopts a sophisticated approach to delens a uniformly pixelized source grid, deconvolved from the source-plane PSF, using efficient Bayesian optimization. The results from different tests indicate that the pixelated reconstructions provide a much reliable estimation of the intrinsic SBD of the simulated sources including rather complex profiles of close compact sources (Section 4.5).

In this chapter, we describe its application on cswa128. The clumpy and irregular morphology of cswa128 makes it an ideal test case for the pixelated algorithm. We utilize the IFU data on multiple images of the lensed galaxy in cswa128 to reconstruct the source-plane Hα maps at high resolution using the pixelated grid reconstruction. We then run these reconstructed maps through a clump-finding algorithm ASTRODENDRO to detect Hα clumps. Using the clump detections made by ASTRODENDRO, we are able to measure the SNR and physical sizes of H II regions in the source plane. We repeat the Hα fitting and clump detection for the source-plane Hα maps reconstructed using the direct method and compare the results of the clump size measurements from the two methods of reconstruction. This comparison of SNR and clump sizes is helpful in understanding the implications of spatial resolution effects on deriving the sizes of star-forming regions in gravitationally lensed high-z objects.

The structure of this chapter is as follows - Section 5.2 describes the application of the pixelated technique on IFU data of lensed images a1 and a2 of cswa128 to compute the corresponding Hα maps. In Section 5.3, we describe clump measurements and address the differences in the physical sizes of Hα clumps between the direct and pixelated methods of source reconstruction. We discuss the results in Section 5.4 and present the conclusions in

Section 5.5.

5.2. Source Reconstruction

We extract 14 wavelength channels in the vicinity of the Hα emission line from the IFU data corresponding to a1 and a2 images in the lensed system. We then utilize the detailed lens model presented in Chapter 2 to reconstruct these channels using two different methods in LENSTOOL: direct reconstruction or traditional ray-tracing and pixelated grid algorithm. Using the 3D datacube source reconstruction task in LENSTOOL (see Appendix A for details), we obtain a ray-traced source-plane datacube for both the lensed images. The source plane resolution obtained after a sub-sampling of 5 on the source grid enables in a pixel scale of $0.''02$. On the other hand, pixelated grid reconstruction is computed through individual LENSTOOL runs of each of the channels in the datacube. In terms of code, both these techniques are available to use with the *cleanlens* task in LENSTOOL (see Appendix A for description of its usage).

As mentioned in Section 4.3, the standard deviation of noise, full width at half maximum (FWHM) of PSF in the image plane and Gaussian RBF in the source plane are the important inputs to the pixelated algorithm in LENSTOOL, in addition to the lens model best fit parameters. To estimate the noise in the data, we not only consider the variance of emission-free regions of the datacube, but also the correlation of noise between pixels. We use the value of AO corrected PSF of $0.''12$ and $0.''15$ for IFU observations of a1 and a2 lensed images respectively. The size of the Gaussian RBF is defined as a factor of the sampling in the source plane to remove any dependencies of the source pixel size on the final reconstruction (Section 4.3). Specifically, we test values of 1.5, 1.75, 2.0, 2.25, 2.5 as the ratios of the FWHM of the RBF to the sampling in the source plane. We note relatively higher image plane $\chi 2$ for RBF > 2.0 but do not find significant differences among the others. Therefore, we present the results using a RBF ratio of 1.5.

Figures 5.1a and 5.1c show snapshots of the reconstructed source frames around the red-shifted Hα emission line using the pixelated and direct approach for the a1 and a2 lensed images respectively. On the basis of visual inspection of the reconstructed images, the clumpy features in the light profile (cyan ellipses in 5.1b), especially with low SNR, are more pronounced in the pixelated reconstruction of a wavelength channel as compared to the direct method for lensed image a1. This is because these faint features become further diffused in the direct reconstruction owing to the wings of the lensing PSF in the source-plane. The corresponding 2D Hα maps generated for both of the lensed images are shown in Figure 5.1b and 5.1d (further details in Section 5.2.1).

Quantitatively, the maximum linear resolution achieved in the direct reconstruction as derived from the FWHM of the projected image plane PSF in the direction of greatest magnification varies between 25-290 pc. With the pixelated technique, we achieve a uniform resolution of ~ 250 pc derived from the size of the Gaussian RBF used to reconstruct the source plane. Even though the maximum linear resolution is higher with the direct approach, the irregular source plane PSF introduces uncertainties in the measurement of clump sizes, as demonstrated in the next section.

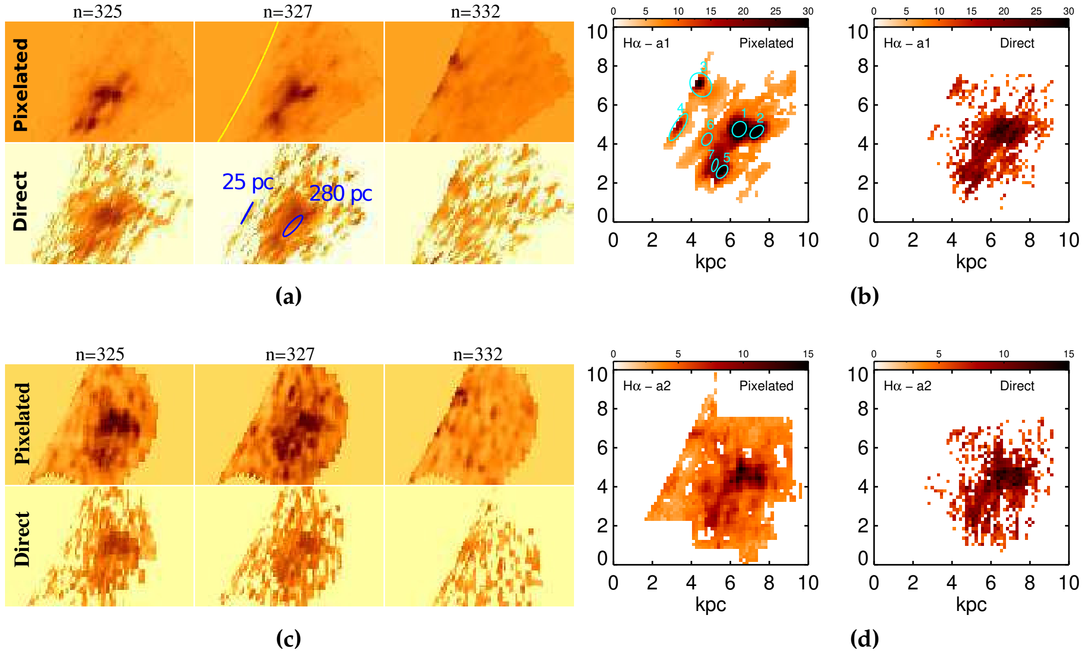

Figure 5.1 (a) Reconstruction of three arbitrary wavelength channels around the Hα emission line using the pixelated (upper panels) and direct (lower panels) methods of source reconstruction from the a1 datacube. Different values of **n** at the top of the panels represent the channel numbers in the corresponding IFU data cubes. The yellow curve shown in the middle panel represents caustics (regions of high magnification in the source plane) using the best fit lens model. The blue ellipses show the FWHM of the effective source plane PSF's at two different locations in the source plane. (b) Derived 2D source plane Hα intensity maps in units of 10^{-16} erg s^{-1} cm^{-2} arcsec^{-2} using the pixelated and direct method of source reconstruction for the a1 lensed image. The cyan ellipses refer to the clumps detected by the ASTRODENDRO in the pixelated reconstruction of the a1 lensed image as described in Section 5.3. (c) and (d) same as (a) and (b) respectively, but for the lensed image a2.

5.2.1. Hα emission line fitting

We fit the Hα emission lines in the reconstructed source plane data for the a1 and a2 lensed images with the same fitting procedure as described in Chapter 3. For every pixel in the source plane, we fit a 1D Gaussian profile to the Hα emission line using a weighted χ^2 minimization procedure with the redshifts, the Gaussian FWHM and the flux of the emission line as free parameters. We reconstruct the channels free of emission lines and close to the redshifted Hα wavelength to calculate the variance spectrum for weighting the source spectrum. The results from Hα fitting are shown in Figures 5.1b and 5.1d.

Figure 5.1 illustrates the advantage of the pixelated approach in recovering the intrinsic shape of the source profile and in maximizing the SNR on the Hα emission, especially in the highly distorted regions (clump IDs: 3 and 4) near the caustics. We present a rigorous analysis of the clump sizes and their SNR in Section 5.3.

A clear distinction between the two approaches is more apparent for a1 than a2 because of the higher SNR in the observational data of a1 lensed image. As expected, this reflects the sensitivity of the pixelated algorithm towards the SNR of the input image plane data. Moreover, we notice that the actual values of Hα fluxes vary across the reconstruction of individual images due to significant uncertainties ($\sim 25\%$) in the flux calibration of the two observations. However, since we only compare the physical profiles of the reconstructed images, we do not need to account for the differences in the absolute values of Hα fluxes.

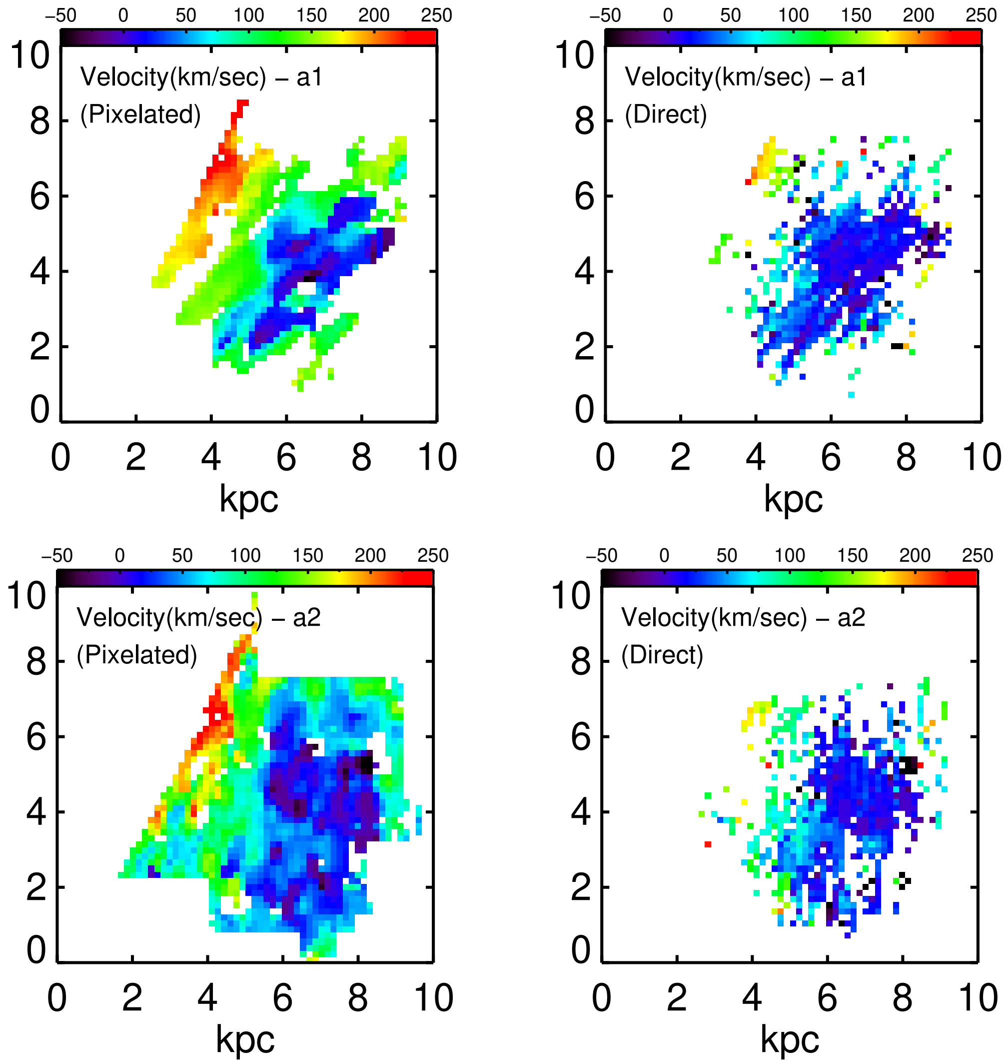

Figure 5.2 Comparison of derived source-plane 2D rotational velocity maps for a1 and a2 lensed images of cswa128 using the traditional and pixelated methods of source reconstruction in LENSTOOL. Using the pixelated approach, we can easily recover the kinematics of this system in the extended regions of low Hα brightness emission, that had been missed by the direct reconstruction.

5.2.2. Kinematics

Following the procedure of Hα emission line fitting highlighted in the earlier section, we compute the resolved maps of rotational velocities for a1 and a2 lensed images. The kinematic center (having zero velocity) is chosen to lie at the peak of the Hα brightness in the source plane. Figure 5.2 shows the Hα kinematics of the two multiple images in cswa128. Comparing the pixelated results with those of direct reconstruction, we conclude that the high velocity i.e. >150 km/sec (or low Hα surface brightness) regions are completely missed in the direct approach indicating the gain in spatial resolution achievable with the pixelated technique. The resolved kinematic maps generated via the pixelated approach are also in strong agreement with the results of the manual forward approach presented in Chapter 3 (Figure 3.3). A full detailed kinematic analysis is beyond the scope of this thesis and will be done in the follow up work on this lensed system. We also note that the maps for a1 and a2 are consistent with each other showing that they belong to the same lensed galaxy.

5.3. Clump Measurements

In this section, we report the clump sizes measured in the derived source-plane Hα profile of the a1 lensed image computed using both the methods of reconstruction. We do not consider a2 because of the low SNR in the reconstructed data. We use a python package ASTRODENDRO[1] to compute hierarchical trees of structures called dendograms (Rosolowsky et al. 2008; Goodman et al. 2009) to detect clumps in the Hα maps. As compared with other non-hierarchical methods (e.g. CLUMPFIND, Williams, de Geus & Blitz 1994), ASTRODENDRO prevents the formation of 'pathological' small clumps between two prominent clumps and allows structures with very different physical scales to be detected (Goodman et al. 2009).

The algorithm selects clumps on the basis of three input parameters: (a) minimum value of flux that acts as a threshold to define clumps; we set it to 5σ (b) minimum difference in flux between two close structures for them to be considered separate; we set it to 10 % following Oklopčić et al. (2017) (c) minimum number of pixels in a clump, which is set to be 4 pixels corresponding to an effective radius of selected clumps to be greater than the source plane RBF size used for reconstruction.

After computing the dendrograms, the ASTRODENDRO package extracts the relevant parameters such as the location, surface area, effective major, minor axis and total fluxes of the identified structures. We find seven clumps in the pixelated reconstruction that satisfy the criteria we imposed. However, not all of these identified clumps are recovered using the traditional approach. We define the effective radius of a clump as the half width at half maximum (HWHM) derived from the geometric mean of the semi-major and semi-minor axis of the ellipse fitted to that clump in the source plane emission-line map.

We correct the effective radii of clumps by subtracting the appropriate PSF HWHM at the clump location in quadrature. In case of direct reconstruction, the lensing PSF is non-uniform across the source plane and is therefore calculated separately at the location of each clump. On the other hand, a regular PSF correction equivalent to the RBF size is applied to the clump sizes derived using the pixelated reconstruction. As shown in Figure 5.3, the effective size estimates of the clumps are always lower using the pixelated method. Moreover, higher number of clumps are detected in the pixelated source-plane Hα reconstruction. For detections, where either of the effective axis estimate returned by the ASTRODENDRO is smaller than the size of the source plane PSF at that location, we plot the upper limit at the value of the source plane PSF as shown in Figure 5.3.

We use the fitted elliptical apertures in the pixelated reconstruction as a guide to measure the SNR of the individual clumps. Noise is calculated as the standard deviation of the total flux within a given aperture in the emission-line free regions of the source. SNR is then computed as the ratio of the total flux within the aperture to the value of noise. For locations

[1]http://www.dendrograms.org/

in the source plane where we only detect clumps using the pixelated method, we report an upper limit of 3 on their SNR in the direct reconstruction.

Figure 5.3 compares the SNR and PSF corrected physical sizes (effective radii) of the clumps detected in the a1 source plane Hα maps for both the reconstruction techniques. SNR of the clumps in the pixelated approach is higher than the traditional approach by almost a factor of 10. In particular, smaller clumps near the caustics (IDs: 3, 4 and 8 in Figure 5.2) are resolved with greater SNR using the pixelated reconstruction. This figure also shows that the pixelated method allows more clump detections that yields atleast 100 pc smaller clump sizes.

We use the jackknife method to calculate the uncertainties in the clump sizes derived using the pixelated approach. For each wavelength channel, we average 100 randomly drawn samples returned by the MCMC sampler to create n different realizations. Then, Hα emission line fitting is repeated n times and ASTRODENDRO measurements are computed on each of these fitted Hα maps. When necessary, the effective radii of the ellipses measured by the ASTRODENDRO package are thresholded at the PSF size along a particular axis and then the geometric mean (or effective radii) are calculated. Finally, the uncertainty is calculated as the standard deviation of the effective radii from all the random realizations in the jackknife tests.

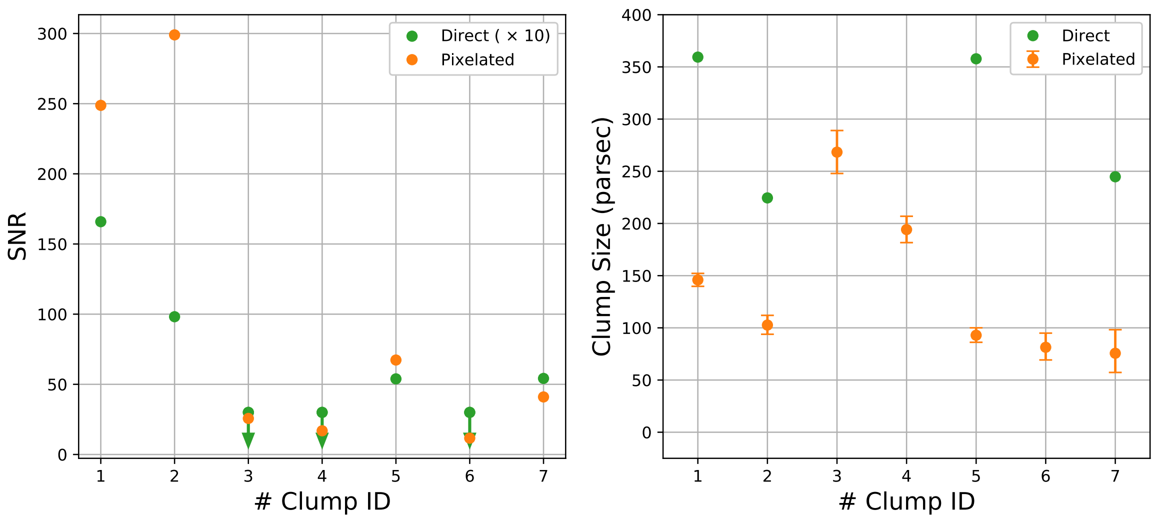

Figure 5.3 Clump SNR and sizes: pixelated vs direct reconstruction. **Left:** SNR comparison for all the clumps detected in the source-plane reconstruction of Hα maps as labelled in Figure 5.1b. SNR estimated for detections in the direct reconstruction (green data points) has been artificially enhanced by a factor of 10 to exemplify the difference in values between the two methods. Only clump IDs 1, 2, 5 and 7 are detected in the direct reconstruction. For the other clumps, we plot the SNR as an upper limit, set at 3. **Right:** PSF corrected clump sizes characterized by Gaussian HWHM for detections in the Hα maps obtained with the two methods of reconstruction.

5.4. Discussion

Observationally, in the high-z universe, clumps have mostly been identified in the rest-frame UV, optical or Hα maps (Elmegreen et al. 2007, 2009; Genzel et al. 2011; Förster Schreiber et al. 2011; Guo et al. 2012; Wuyts et al. 2012; Tadaki et al. 2014; Buck et al. 2017). In this work, we recover the physical sizes of H II regions that probe star-formation in this lensed system. Previous measurements (Elmegreen et al. 2005, 2007, 2009; Förster Schreiber et al. 2011; Guo et al. 2011, 2015) of clump sizes in star-forming galaxies at $1 \lesssim z \lesssim 3$ have suggested that star-formation occurs in large complexes with critical scale of ~ 1 kpc. On the contrary, results from this work otherwise indicate that star-formation can also occur on small spatial scales in this redshift interval. Smallest physical scale that we recover in the lensed galaxy using the pixelated reconstruction is ~ 100 *pc*, which has not been seen in the analysis of the ray-traced image. Similar results have also been recently shown by Johnson et al. (2017b) where star-forming clumps have been detected with sizes down to ~ 30 pc using a forward source modelling technique to deconvolve the effects of lensing PSF.

While there are only a handful of high-z systems that have been probed at such small spatial scales, these studies have indicated a clear correlation of the size distribution of clumps with the spatial resolution achievable in the source plane at such redshifts. Therefore, we need to expand such analyses to a larger sample of lensed galaxies in order to gain new insights into the epoch of star-formation and assembly of galaxies. We discuss such plausible ways of applying the pixelated technique to a large sample of lensed galaxies in our future work in the final chapter of the thesis.

5.5. Conclusions

This chapter examines the use of pixelated source modelling approach on cswa128 in probing the spatial scales of star-formation at $z \sim 2$. We present an in-depth analysis of the lensed system where we demonstrate that we are able to gain more information about the source morphology after deconvolving the effects of lensing PSF from the source profile. The case study of the pixelated technique on cswa128, as presented in this chapter, clearly shows that the approach is successful in minimizing the anisotropic distortion due to the PSF in the source plane, yielding more accurate source profiles. Specifically, with the pixelated reconstruction, we can probe spatial scales upto 100 pc within the clumps after correcting for the source-plane PSF. We also obtain ~ 10 times higher SNR values in clump detections using the pixelated reconstruction, some of which are undetected with the direct reconstruction. Moreover, we can maximize the SNR of the most distorted and faint clumps near the caustics in the source plane only using the pixelated method of reconstruction.

The results of this case study of the pixelated approach on cswa128 present a counter example to the general picture of high-z clump size measurements in literature and therefore need further validation with similar examples. In the next and the final chapter of this thesis, I present the key conclusions of my thesis and discuss the scope for future work.

CHAPTER 6

Conclusions

Somewhere something incredible is waiting to be known.
– Carl Sagan

Spatially resolved observations of galaxies in the peak of the star formation epoch ($z \sim 1-3$; Madau & Dickinson, 2014) hold the key for understanding the physics of galaxy formation and evolution. The main aim of this thesis was to develop forward source modelling to allow unparalleled view of individual star-forming regions at the highest spatial resolution yielding clump properties in galaxies between $1 \leq z \leq 3$.

Gravitational lensing provides a rare opportunity to obtain magnified views of these galaxies at an enhanced spatial resolution. Observations of strongly lensed galaxies have revealed a large number of clumpy irregular disks at higher redshifts ($z > 1$). However, the clump properties are observed to be a function of the spatial resolution. Moreover, it has not been possible to fully exploit lensing in high-redshift studies with traditional ray-tracing methods of source reconstruction. This is because the traditional approach of backward ray-tracing the image introduces a differential PSF smearing in the source plane due to the combination of the image-plane PSF and asymmetric lensing shear. This gives rise to an effective spatial source-plane resolution that is significantly lower than that enabled by the lensing amplification. Furthermore, the loss in resolution becomes even more severe in the highly magnified regions of the source plane, thus presenting a major hurdle in recovering the intrinsic properties of lensed galaxies at the highest resolution.

For the first part of the project, we develop a unique forward modelling approach to combine IFU observations from different multiple images of a lensed target. The application of this approach was validated using a pilot study in Chapter 3 on a highly magnified lensed galaxy, cswa128, at $z \sim 2$. In this case we obtained an order of magnitude improvement in the source plane spatial resolution as compared to the traditional ray-tracing methods. This approach is based on a well constrained and robust lens model presented in Chapter 2. This pilot study into the novel technique was extremely useful as it helped in maximally utilizing the spatial information on multiple extended arcs of the same source.

The success of this pilot study paved the way for the next project where we developed a pixelized source-modelling approach and integrated it into the source code of LENSTOOL. Unlike the pilot study where the forward modelling involved manual intervention, the pixelized grid algorithm is fully automated. This new technique utilized constraints from the extended surface-brightness profile of the lensed source for a given lens model and reconstructed its intrinsic distribution on a pixelated grid using a Bayesian MCMC optimization algorithm in LENSTOOL. The algorithm was applied to reconstruct the morphology of cswa128 where we obtained a significant improvement ($\sim \times 10$; Figure 5.3) in the SNR over the traditional method of reconstruction. This is because this novel technique recovers low surface brightness clumps in the source morphology as a result of PSF deconvolution in the source-plane (Figure 5.1). Moreover as consistently suggested by the detailed morphological and kinematical analysis in both projects, we propose an ongoing merger as the origin of the lensed system in cswa128.

To prepare ourselves for interpreting large samples of lensed galaxies, it is of crucial importance to continue studying individual cases like cswa128 in great detail in order to better understand the systematics of lens models and capture the important physical properties of high-z galaxies that are otherwise unattainable without lensing. For example, the fraction of mergers in star-forming galaxies at $z \sim 1-3$ has long been debated. In this redshift regime, merger fractions show a strong dependence with the classification scheme used to classify merger signatures in high-z observational data (e.g. Hung et al. 2015; Molina et al. 2017). Predictions from high resolution simulations show that current observations significantly underestimate the occurrence of mergers in typical star forming galaxies at $z \geq 1$ (Rodriguez-Gomez et al. 2015). Gravitational lensing coupled with high resolution imaging and spectrographic observations have the potential to unambiguously classify a galaxy as a merger or disk dominated as demonstrated in this work. In fact, without gravitational lensing, a galaxy like cswa128 would easily be misclassified as a typical clumpy SF galaxy at $z \sim 2$. Furthermore, the work from this thesis will provide timely application to a wide variety of lensed systems that will become available with the future instruments such as NIRSpec aboard JWST or GMTIFS on GMT in addition to lensed surveys like LSST.

6.1. Future Work

During my PhD, I have gained extensive experience in modelling lensed sources and analyzing IFU observations, therefore preparing me to deal with challenges in both theoretical modelling and observations. In particular, my work with LENSTOOL development to include forward source modelling and PSF deconvolution has uniquely positioned me to resolve the controversies around the complex nature of star-forming clumps and their cosmic evolution.

6.1.1. Theoretical Advances

There are a few ways to improve the precision of source reconstruction obtained via the pixelated grid method in LENSTOOL. The current implementation of the algorithm has been done using a regular grid in the source-plane. However, an irregular adaptive source grid helps to take full advantage of the information contained in the lensed images (e.g.

Nightingale & Dye 2015). It effectively allows higher resolution in the more magnified sub-regions of the source. Therefore, we will upgrade the code to a more advanced, adaptive grid procedure. Another possible extension of this work would be to incorporate a regularization term in the $\chi 2$ calculation (Joseph et al. 2019) and compare its use with RBFs in the source plane.

One of the main limitations of the pixelated algorithm is that it does not take into account lens model fitting when reconstructing the lensed source profile i.e. we keep the lens parameters fixed at the 'best' values returned by the MCMC sampler during lens fitting alone. This is a non trivial problem because of the very high computational cost of such an optimization task. However, an intermediate solution would be to only iterate over a few lens mass parameters (drawn from the posterior of lens model fitting) thus allowing us to recover the best source reconstruction and lens potential simultaneously.

Finally, theoretically it should be possible to combine multiple observations (a1 and a2 in the case of cswa128) in a single optimization run to improve SNR in the final source plane reconstruction. The technical implementation for multiple image fitting would require different *imframe*s (see Appendix A for details on this keyword) in LENSTOOL. While that is currently not possible, incorporating them into LENSTOOL would be our immediate goal for the future. I intend to follow up my work on forward source modelling to include some of the modifications as mentioned earlier in this section.

6.1.2. Observational Prospects

Motivated by the results of the pixelated grid approach on cswa128, it is possible to apply this technique to characterize the properties of a large sample of high-z lensed galaxies with an unprecedented spatial resolution. In my follow-up work, I will compile existing HST imaging and spectroscopic data on sources detected through previous observations of strongly lensed systems behind galaxy clusters. Most of the lensing clusters have been studied extensively in the literature and therefore have high resolution lens models that can be exploited with the help of pixelated source modelling technique to acquire a deeper understanding of the background source properties.

My sample will primarily consist of lensed galaxies from the data samples of Livermore et al. (2012) (8 galaxies), Livermore et al. (2015) (17 galaxies), The Grism Lens-amplified Survey from Space (GLASS) survey; Jones et al. (2015) (3 galaxies), Wang et al. (2018) (2 galaxies), Patrício et al. (2018) (8 galaxies). Most of the lensing clusters from Jones et al. (2015) and Patrício et al. (2018) have been observed either as a part of *Frontier Fields* or *CLASH* initiative with lens-models being publicly available. Adaptive optics-assisted integral field spectroscopy is available for all the lensed systems from Livermore et al. (2012) and Livermore et al. (2015) with VLT/SINFONI, Keck/OSIRIS and Gemini/NIFS instruments and from MUSE for Patrício et al. (2018) sample. Systems available from GLASS survey have HST grism spectroscopy on the multiple images.

Specifically, like cswa128, we can measure the intrinsic sizes of star-forming clumps for the new sample of galaxies. Moreover, reconstruction of HST imaging as well as IFU data will enable detailed comparison of stellar and ionized gas morphologies of high-z lensed systems. It will also be possible to directly compare my modelled sources with previous results in literature allowing to find more compact clumps than previously observed in the studies of high-z lensed objects.

We can also derive the 2D kinematics i.e. velocity and dispersion maps from the reconstructed IFU data of the sample. The high resolution will enable to distinguish whether a galaxy is rotationally-supported, velocity dispersion-dominated, or interacting/merging. Accurate measurements of intrinsic kinematical properties of a large sample will thus provide valuable insights into feedback mechanisms that drive star-formation in high-z galaxies.

The pixelated technique can also be applied to IFU data to probe the dynamical evolution of clump properties with cosmic time, thus providing strong observational constraints for their theoretical modelling in cosmological simulations (e.g. Ceverino, Dekel & Bournaud 2010). Therefore this project will not only deliver the largest homogeneous sample of high-z clump properties derived so far that will allow a direct comparison with local studies but will also provide an important benchmark for comparisons to the predictions by cosmological simulations of high-z galaxies.

The results from the application of pixelated modelling techniques on existing data of lensed galaxies will motivate its further use on simulated JWST data products as well as new data from ground-based telescopes. This will help us prepare better for upcoming deep surveys using JWST's NIRSpec and MIRI instrument that combined with previous observations will provide new insights into the most active period of galaxy formation.

Bibliography

Abdelsalam H. M., Saha P., Williams L. L. R., 1998, MNRAS, 294, 734

Acebron A., Jullo E., Limousin M., Tilquin A., Giocoli C., Jauzac M., Mahler G., Richard J., 2017, MNRAS, 470, 1809

Auger M. W., Budzynski J. M., Belokurov V., Koposov S. E., McCarthy I. G., 2013, MNRAS, 436, 503

Barrera-Ballesteros J. K. et al., 2015, A&A, 582, A21

Bayliss M. B., Johnson T., Gladders M. D., Sharon K., Oguri M., 2014a, ApJ, 783, 41

Bayliss M. B., Rigby J. R., Sharon K., Wuyts E., Florian M., Gladders M. D., Johnson T., Oguri M., 2014b, ApJ, 790, 144

Behrendt M., Burkert A., Schartmann M., 2015, MNRAS, 448, 1007

Bernardi M. et al., 2003, AJ, 125, 1849

Bertin E., Arnouts S., 1996, A&AS, 117, 393

Bouché N. et al., 2007, ApJ, 671, 303

Bournaud F., 2016, in Astrophysics and Space Science Library, Vol. 418, Galactic Bulges, Laurikainen E., Peletier R., Gadotti D., eds., p. 355

Bournaud F., Elmegreen B. G., 2009, ApJ, 694, L158

Bouwens R. J. et al., 2012, ApJ, 752, L5

Bradley L. D. et al., 2008, ApJ, 678, 647

Brewer B. J., Lewis G. F., 2006, ApJ, 651, 8

Bruzual G., Charlot S., 2003, MNRAS, 344, 1000

Buck T., Macciò A. V., Obreja A., Dutton A. A., Domínguez-Tenreiro R., Granato G. L., 2017, MNRAS, 468, 3628

Bundy K. et al., 2015, ApJ, 798, 7

Calzetti D., Armus L., Bohlin R. C., Kinney A. L., Koornneef J., Storchi-Bergmann T., 2000, ApJ, 533, 682

Caminha G. B. et al., 2017, A&A, 607, A93

Cappellari M. et al., 2011, MNRAS, 413, 813

Carton D. et al., 2018, MNRAS, 478, 4293

Cen R., Ostriker J. P., 1993, ApJ, 417, 415

Ceverino D., Dekel A., Bournaud F., 2010, MNRAS, 404, 2151

Chabrier G., 2003, PASP, 115, 763

Claeskens J.-F., Sluse D., Riaud P., Surdej J., 2006, A&A, 451, 865

Clowe D., Schneider P., 2002, A&A, 395, 385

Coe D., Benítez N., Broadhurst T., Moustakas L. A., 2010, ApJ, 723, 1678

Coe D., Fuselier E., Benítez N., Broadhurst T., Frye B., Ford H., 2008, ApJ, 681, 814

Coe D. et al., 2013, ApJ, 762, 32

Colina L., Arribas S., Monreal-Ibero A., 2005, ApJ, 621, 725

Collett T. E., 2015, ApJ, 811, 20

Colley W. N., Tyson J. A., Turner E. L., 1996, ApJ, 461, L83

Contini T. et al., 2016, A&A, 591, A49

Contini T. et al., 2012, A&A, 539, A91

Cortijo-Ferrero C. et al., 2017, MNRAS, 467, 3898

Covone G., Adami C., Durret F., Kneib J.-P., Lima Neto G. B., Slezak E., 2006, A&A, 460, 381

Cresci G. et al., 2009, ApJ, 697, 115

Cresci G., Mannucci F., Maiolino R., Marconi A., Gnerucci A., Magrini L., 2010, Nature, 467, 811

Croom S. M. et al., 2012, MNRAS, 421, 872

Davies R. I., 2007, MNRAS, 375, 1099

de Vaucouleurs G., 1959, Handbuch der Physik, 53, 275

Delgado R. G. et al., 2013, in IAU Symposium, Vol. 295, The Intriguing Life of Massive Galaxies, Thomas D., Pasquali A., Ferreras I., eds., pp. 300–303

Dessauges-Zavadsky M. et al., 2017, A&A, 605, A81

Diego J. M., Broadhurst T., Zitrin A., Lam D., Lim J., Ford H. C., Zheng W., 2015, MNRAS, 451, 3920

Diego J. M., Sandvik H. B., Protopapas P., Tegmark M., Benítez N., Broadhurst T., 2005, MNRAS, 362, 1247

Dyer C. C., Roeder R. C., 1980, ApJ, 241, L133

Einstein A., 1936, Science, 84, 506

Elíasdóttir Á. et al., 2007, ArXiv e-prints

Elmegreen B. G., Elmegreen D. M., Chandar R., Whitmore B., Regan M., 2006, ApJ, 644, 879

Elmegreen B. G., Elmegreen D. M., Vollbach D. R., Foster E. R., Ferguson T. E., 2005, ApJ, 634, 101

Elmegreen D. M., Elmegreen B. G., Marcus M. T., Shahinyan K., Yau A., Petersen M., 2009, ApJ, 701, 306

Elmegreen D. M., Elmegreen B. G., Ravindranath S., Coe D. A., 2007, ApJ, 658, 763

Faber S. M., Jackson R. E., 1976, ApJ, 204, 668

Fensch J., Duc P.-A., Weilbacher P. M., Boquien M., Zackrisson E., 2016, A&A, 585, A79

Fisher D. B. et al., 2017, MNRAS, 464, 491

Folkes S. et al., 1999, MNRAS, 308, 459

Förster Schreiber N. M. et al., 2006, The Messenger, 125

Förster Schreiber N. M. et al., 2018, ApJS, 238, 21

Förster Schreiber N. M. et al., 2011, ApJ, 739, 45

Franx M., Illingworth G. D., Kelson D. D., van Dokkum P. G., Tran K.-V., 1997, ApJ, 486, L75

Genzel R. et al., 2008, ApJ, 687, 59

Genzel R. et al., 2011, ApJ, 733, 101

Genzel R. et al., 2006, Nature, 442, 786

Girard M. et al., 2018, ArXiv e-prints

Glazebrook K., 2013, PASA, 30, e056

Goodman A. A., Rosolowsky E. W., Borkin M. A., Foster J. B., Halle M., Kauffmann J., Pineda J. E., 2009, Nature, 457, 63

Green A. W. et al., 2014, MNRAS, 437, 1070

Guo Y. et al., 2015, ApJ, 800, 39

Guo Y. et al., 2011, ApJ, 735, 18

Guo Y., Giavalisco M., Ferguson H. C., Cassata P., Koekemoer A. M., 2012, ApJ, 757, 120

Gusev A. S., 2014, MNRAS, 442, 3711

Hewitt J. N., Turner E. L., Schneider D. P., Burke B. F., Langston G. I., 1988, Nature, 333, 537

Ho I. T., Kudritzki R.-P., Kewley L. J., Zahid H. J., Dopita M. A., Bresolin F., Rupke D. S. N., 2015, MNRAS, 448, 2030

Hubble E. P., 1926, ApJ, 64

Hubble E. P., 1936, Realm of the Nebulae

Hung C.-L. et al., 2015, ApJ, 803, 62

Ilbert O. et al., 2010, ApJ, 709, 644

Jauzac M. et al., 2015, MNRAS, 446, 4132

Jauzac M. et al., 2012, MNRAS, 426, 3369

Johnson T. L. et al., 2017a, ApJ, 843, L21

Johnson T. L., Sharon K., 2016, ApJ, 832, 82

Johnson T. L., Sharon K., Bayliss M. B., Gladders M. D., Coe D., Ebeling H., 2014, ApJ, 797, 48

Johnson T. L. et al., 2017b, ApJ, 843, 78

Jones T., Ellis R., Jullo E., Richard J., 2010a, ApJ, 725, L176

Jones T., Ellis R. S., Richard J., Jullo E., 2013, ApJ, 765, 48

Jones T. et al., 2015, AJ, 149, 107

Jones T. A., Swinbank A. M., Ellis R. S., Richard J., Stark D. P., 2010b, MNRAS, 404, 1247

Joseph R., Courbin F., Starck J. L., Birrer S., 2019, A&A, 623, A14

Jullo E., Kneib J.-P., 2009, MNRAS, 395, 1319

Jullo E., Kneib J.-P., Limousin M., Elíasdóttir Á., Marshall P. J., Verdugo T., 2007, New Journal of Physics, 9, 447

Jullo E., Pires S., Jauzac M., Kneib J.-P., 2014, MNRAS, 437, 3969

Katz N., Hernquist L., Weinberg D. H., 1992, ApJ, 399, L109

Kewley L. J., Maier C., Yabe K., Ohta K., Akiyama M., Dopita M. A., Yuan T., 2013, ApJ, 774, L10

Kewley L. J., Rupke D., Zahid H. J., Geller M. J., Barton E. J., 2010, ApJ, 721, L48

Kneib J.-P., 1993, PhD thesis, Ph. D. thesis, Université Paul Sabatier, Toulouse, (1993)

Lagattuta D. J. et al., 2017, MNRAS, 469, 3946

Larkin J. et al., 2006, New Astronomy Reviews, 50, 362

Leethochawalit N., Jones T. A., Ellis R. S., Stark D. P., Richard J., Zitrin A., Auger M., 2016, ApJ, 820, 84

Lefor A. T., Futamase T., Akhlaghi M., 2013, New Astronomy Reviews, 57, 1

Liebes S., 1964, Physical Review, 133, 835

Liesenborgs J., De Rijcke S., Dejonghe H., 2006, MNRAS, 367, 1209

Limousin M. et al., 2016, A&A, 588, A99

Limousin M. et al., 2007, ApJ, 668, 643

Livermore R. C. et al., 2012, MNRAS, 427, 688

Livermore R. C. et al., 2015, MNRAS, 450, 1812

Madau P., Dickinson M., 2014, ARA&A, 52, 415

Mahler G. et al., 2018, MNRAS, 473, 663

Maiolino R. et al., 2008, A&A, 488, 463

Mayer L., Tamburello V., Lupi A., Keller B., Wadsley J., Madau P., 2016, ApJ, 830, L13

Molina J., Ibar E., Swinbank A. M., Sobral D., Best P. N., Smail I., Escala A., Cirasuolo M., 2017, MNRAS, 466, 892

Morgan W. W., 1958, PASP, 70, 364

Narayan R., Bartelmann M., 1996, arXiv Astrophysics e-prints

Narayan R., Blandford R., Nityananda R., 1984, Nature, 310, 112

Navarro J. F., White S. D. M., 1993, MNRAS, 265, 271

Nightingale J. W., Dye S., 2015, MNRAS, 452, 2940

Nightingale J. W., Dye S., Massey R. J., 2018, MNRAS, 478, 4738

Oke J. B., Gunn J. E., 1983, ApJ, 266, 713

Oklopčić A., Hopkins P. F., Feldmann R., Kereš D., Faucher-Giguère C.-A., Murray N., 2017, MNRAS, 465, 952

Patrício V. et al., 2018, MNRAS, 477, 18

Pettini M., Pagel B. E. J., 2004, MNRAS, 348, L59

Refsdal S., 1964, MNRAS, 128, 295

Richard J., Jones T., Ellis R., Stark D. P., Livermore R., Swinbank M., 2011, MNRAS, 413, 643

Richard J. et al., 2010, MNRAS, 404, 325

Rodrigues M., Hammer F., Flores H., Puech M., Athanassoula E., 2017, MNRAS, 465, 1157

Rodriguez-Gomez V. et al., 2015, MNRAS, 449, 49

Rodríguez-Zaurín J., Arribas S., Monreal-Ibero A., Colina L., Alonso-Herrero A., Alfonso-Garzón J., 2011, A&A, 527, A60

Rosolowsky E. W., Pineda J. E., Kauffmann J., Goodman A. A., 2008, ApJ, 679, 1338

Saha P., Williams L. L. R., 1997, MNRAS, 292, 148

Scoville N., 2007, in Astronomical Society of the Pacific Conference Series, Vol. 375, From Z-Machines to ALMA: (Sub)Millimeter Spectroscopy of Galaxies, Baker A. J., Glenn J., Harris A. I., Mangum J. G., Yun M. S., eds., p. 166

Shapiro K. L. et al., 2008, ApJ, 682, 231

Sharon K., Gladders M. D., Rigby J. R., Wuyts E., Koester B. P., Bayliss M. B., Barrientos L. F., 2012, ApJ, 746, 161

Skilling J., 1998, in Maximum Entropy and Bayesian Methods, Erickson G. J., Rychert J. T., Smith C. R., eds., p. 1

Soucail G., Mellier Y., Fort B., Mathez G., Cailloux M., 1988, A&A, 191, L19

Stark D., Ellis R., Richard J., Egami E., Kneib J., Smith G., 2007, in American Astronomical Society Meeting Abstracts, Vol. 210, American Astronomical Society Meeting Abstracts #210, p. 70.03

Stark D. P. et al., 2013, MNRAS, 436, 1040

Stott J. P. et al., 2014, MNRAS, 443, 2695

Suyu S. H., Marshall P. J., Hobson M. P., Bland ford R. D., 2006, MNRAS, 371, 983

Swinbank A. M., Bower R. G., Smith G. P., Smail I., Kneib J.-P., Ellis R. S., Stark D. P., Bunker A. J., 2006, MNRAS, 368, 1631

Swinbank A. M. et al., 2010, Nature, 464, 733

Swinbank A. M., Sobral D., Smail I., Geach J. E., Best P. N., McCarthy I. G., Crain R. A., Theuns T., 2012, MNRAS, 426, 935

Tadaki K.-i., Kodama T., Tanaka I., Hayashi M., Koyama Y., Shimakawa R., 2014, ApJ, 780, 77

Tagore A. S., Keeton C. R., 2014, MNRAS, 445, 694

Tamburello V., Rahmati A., Mayer L., Cava A., Dessauges-Zavadsky M., Schaerer D., 2017, MNRAS, 468, 4792

Troncoso P. et al., 2014, A&A, 563, A58

van Starkenburg L., van der Werf P. P., Franx M., Labbé I., Rudnick G., Wuyts S., 2008, A&A, 488, 99

Walsh D., Carswell R. F., Weymann R. J., 1979, Nature, 279, 381

Wang X. et al., 2018, arXiv e-prints, arXiv:1808.08800

Wang X. et al., 2017, ApJ, 837, 89

Warren S. J., Dye S., 2003, ApJ, 590, 673

White S. D. M., Rees M. J., 1978, MNRAS, 183, 341

Williams J. P., de Geus E. J., Blitz L., 1994, ApJ, 428, 693

Wilson G., Kaiser N., Luppino G. A., Cowie L. L., 2001, ApJ, 555, 572

Wisnioski E. et al., 2015, ApJ, 799, 209

Wisnioski E. et al., 2011, MNRAS, 417, 2601

Wizinowich P. L. et al., 2006, PASP, 118, 297

Wuyts E., 2015, in IAU Symposium, Vol. 309, Galaxies in 3D across the Universe, Ziegler B. L., Combes F., Dannerbauer H., Verdugo M., eds., pp. 243–246

Wuyts E., Rigby J. R., Sharon K., Gladders M. D., 2012, ApJ, 755, 73

Wuyts E. et al., 2016, ApJ, 827, 74

Yang L., Birrer S., Treu T., 2020, arXiv e-prints, arXiv:2001.07719

Yang Y. et al., 2008, A&A, 477, 789

York D. G. et al., 2000, AJ, 120, 1579

Yuan T. et al., 2017, ApJ, 850, 61

Yuan T.-T., Kewley L. J., Rich J., 2013, ApJ, 767, 106

Yuan T.-T., Kewley L. J., Swinbank A. M., Richard J., 2012, ApJ, 759, 66

Yuan T.-T., Kewley L. J., Swinbank A. M., Richard J., Livermore R. C., 2011, ApJ, 732, L14

Zahid H. J., Dima G. I., Kewley L. J., Erb D. K., Davé R., 2012, ApJ, 757, 54

Zheng W. et al., 2012, Nature, 489, 406

Zwicky F., 1937, Phys. Rev., 51, 290

Appendices

APPENDIX A

Source reconstruction through *cleanlens* task in LENSTOOL

Technical details of three different modes of *cleanlens*, that I have used or developed in my thesis, are described in this appendix. This task forms a part of the input parameter file that is required by LENSTOOL.

- *cleanset = 1 :*
  - **Direct Image Reconstruction**

    This feature uses a pixel frame of lensed image as an input (keyword- *imframe* in the parameter file below) and computes the corresponding source frame (keyword- *sframe*) by applying the lens equation 1.2 for every pixel in the image frame at a given redshift. Subsampling parameters *echant* and *sechant* need to be specified to define the sampling of pixels in the image and source plane respectively. The values of these parameters are generally estimated from the flux magnification of the system. While it saves computational time, direct reconstruction effectively transfers the image-plane PSF to the source frame. In scenarios when the units of image pixels are defined as total flux per pixel (instead of surface brightness), it is possible to preserve the surface brightness in the ray-tracing using the keyword *flux =1*.
  - **3D Datacube Direct Reconstruction (*New*)**

    This mode is an extended application of *cleanset = 1* to IFU datacubes. It computes 3D datacube source frame for every input image cube supplied to LENSTOOL employing the same algorithm as that of direct reconstruction. In practice, to use this feature of source reconstruction, keyword- *imframe* simply needs to be replaced by *cubeframe* in the parameter file below.

Below is a parameter file that was used to reconstruct NIRC2 imaging data with the direct reconstruction algorithm. The output reconstructed frames are illustrated in Figure 3.1.

```
runmode
        reference       3 299.647000 59.849762
        image    0 image.mul
        source   0 source.dat
        inverse  0 0.1 200
        pixel    0 151 simu.fits
        end
grille
        nombre   100
        polaire  0
        nlentille       6
        end
source
        z_source        2.225000
        end
cleanlens
        cleanset        4 2.225
        imframe 3 image_a1.fits      ## NIRC2 Image to be reconstructed
        contour 1 contour.dwcs   ## Contour in image plane sent to source plane
        c_image center.dwcs      ## Center of the image that defines the source
        ncont   1 clean.fits
        sframe  source_a1.fits   ## Source file name
        pixelx    0.04           ## Pixel scale in image plane data
        pixely    0.04
        s_n       100            ## 100 * 100 grid in source plane
        echant   10
        s_echant  2
        flux  1          # conserve surface brightness
        end

potentiel       O1               ## Lens model
        profil  81
        x_centre        4.453426
        y_centre        3.941943
        ellipticite     0.665719
        angle_pos       43.658438
        core_radius     15.886827
        core_radius_kpc 55.249964
        cut_radius      57.793073
        cut_radius_kpc  200.988228
        v_disp      709.825612
```

```
        z_lens      0.2140
        end
potentiel       O2
        profil  81
        x_centre          0.000000
        y_centre          0.000000
        ellipticite       0.200000
        angle_pos         0.000000
        core_radius       0.000000
        core_radius_kpc   0.000000
        cut_radius        44.234021
        cut_radius_kpc    153.833618
        v_disp      281.013163
        z_lens      0.2140
        end
potentiel       2.
        profil  81
        x_centre          2.024064
        y_centre          −2.579400
        ellipticite       0.208219
        angle_pos         90.000000
        core_radius       0.000000
        core_radius_kpc   0.000000
        cut_radius        15.820339
        cut_radius_kpc    55.018739
        v_disp      95.614555
        mag         18.588000
        z_lens      0.2140
        end
potentiel       3.
        profil  81
        x_centre          3.293941
        y_centre          1.151280
        ellipticite       0.000000
        angle_pos         0.000000
        core_radius       0.000000
        core_radius_kpc   0.000000
        cut_radius        8.340955
        cut_radius_kpc    29.007522
        v_disp      69.426298
        mag         19.978000
        z_lens      0.2140
        end
potentiel       4.
        profil  81
```

```
        x_centre        -10.674163
        y_centre        -9.406440
        ellipticite     0.000000
        angle_pos       0.000000
        core_radius     0.000000
        core_radius_kpc 0.000000
        cut_radius      24.525383
        cut_radius_kpc  85.292458
        v_disp  119.048521
        mag     17.636000
        z_lens  0.2140
        end
potentiel       5.
        profil  81
        x_centre        -10.560429
        y_centre        -13.215240
        ellipticite     0.810874
        angle_pos       260.000000
        core_radius     0.000000
        core_radius_kpc 0.000000
        cut_radius      20.389933
        cut_radius_kpc  70.910513
        v_disp  108.548545
        mag     18.037000
        z_lens  0.2140
        end
cline
        nplan   0 2.225000
        dmax    500.000000
        algorithm       MARCHINGSQUARES
        limitHigh       5.0
        limitLow        0.100000
        end
grande
        iso     0 0 1.000000 0.000000 0.000000
        name    best
        profil  0 0
        contour 0 0
        large_dist      2.000000
        end
cosmologie
        model   1
        H0      70.000000
        omegaM  0.300000
        omegaX  0.700000
```

```
        omegaK   0.
        wX       −1.000000
        wa       0.000000
        end
champ
        xmin     −11.875
        xmax     11.875
        ymin     −11.875
        ymax     11.875
        end
fini
```

- *cleanset = 4 :* **Pixelated Grid Reconstruction (*New*)**

  For a given image frame, this task computes an optimized source frame with a fixed ray-tracing matrix provided by the lens model. Again, source grid is user-defined with the help of subsampling parameters *echant* and *sechant* similar to *cleanset = 1*. FWHM of gaussian PSF, source RBF are defined in a separate section *observ* of the parameter file.

Below is an example parameter file that was used to initiate a test run of the pixelated algorithm.

```
runmode
      reference         3  299.647000  59.849762
      image     0  image.mul
      source    0  source.dat
      inverse  3  0.1  200              ## Run optimization
      pixel     0  151  simu.fits
      end
grille
      nombre   100
      polaire  0
      nlentille        6
      end
source
      z_source         2.225000
      end
cleanlens
      cleanset         4  2.225
      imframe  3  slice325.fits        ## Image to be reconstructed
      wframe   3  wframe325.fits       ## 2D weight map
      c_image  center.dwcs
      ncont    0  clean.fits
      pixelx   0.1                     ## Pixel scale in image data
      pixely   0.1
```

```
        s_n      100                ## 100 * 100 grid in source plane
        echant   5
        s_echant         5
        end

potentiel       O1                ## Lens model
        profil   81
        x_centre         4.453426
        y_centre         3.941943
        ellipticite      0.665719
        angle_pos        43.658438
        core_radius      15.886827
        core_radius_kpc  55.249964
        cut_radius       57.793073
        cut_radius_kpc   200.988228
        v_disp     709.825612
        z_lens     0.2140
        end
potentiel       O2
        profil   81
        x_centre         0.000000
        y_centre         0.000000
        ellipticite      0.200000
        angle_pos        0.000000
        core_radius      0.000000
        core_radius_kpc  0.000000
        cut_radius       44.234021
        cut_radius_kpc   153.833618
        v_disp     281.013163
        z_lens     0.2140
        end
potentiel        2.
        profil   81
        x_centre         2.024064
        y_centre         -2.579400
        ellipticite      0.208219
        angle_pos        90.000000
        core_radius      0.000000
        core_radius_kpc  0.000000
        cut_radius       15.820339
        cut_radius_kpc   55.018739
        v_disp     95.614555
        mag        18.588000
        z_lens     0.2140
        end
```

```
potentiel      3.
        profil   81
        x_centre          3.293941
        y_centre          1.151280
        ellipticite       0.000000
        angle_pos         0.000000
        core_radius       0.000000
        core_radius_kpc   0.000000
        cut_radius        8.340955
        cut_radius_kpc    29.007522
        v_disp      69.426298
        mag         19.978000
        z_lens      0.2140
        end
potentiel      4.
        profil   81
        x_centre          −10.674163
        y_centre          −9.406440
        ellipticite       0.000000
        angle_pos         0.000000
        core_radius       0.000000
        core_radius_kpc   0.000000
        cut_radius        24.525383
        cut_radius_kpc    85.292458
        v_disp   119.048521
        mag      17.636000
        z_lens   0.2140
        end
potentiel      5.
        profil   81
        x_centre          −10.560429
        y_centre          −13.215240
        ellipticite       0.810874
        angle_pos         260.000000
        core_radius       0.000000
        core_radius_kpc   0.000000
        cut_radius        20.389933
        cut_radius_kpc    70.910513
        v_disp   108.548545
        mag      18.037000
        z_lens   0.2140
        end
cline
        nplan    0  2.225000
        dmax     500.000000
```

```
        algorithm        MARCHINGSQUARES
        limitHigh        5.0
        limitLow         0.100000
        end
grande
        iso     0 0 1.000000 0.000000 0.000000
        name    best
        profil  0 0
        contour 0 0
        large_dist       2.000000
        end
cosmologie
        model   1
        H0      70.000000
        omegaM  0.300000
        omegaX  0.700000
        omegaK  0.
        wX      -1.000000
        wa      0.000000
        end
observe
        rbfsig  1  1.5          ## FWHM of source-plane RBF
        seeing  1 0.12          ## FWHM of image-plane PSF
        binning 0 0
        bruit   0
        sky      0.0
        dispersion       0.0
        idum    -1
        end
champ
        xmin    -11.875
        xmax    11.875
        ymin    -11.875
        ymax    11.875
        end
fini
```

APPENDIX B

Simulation Results

Here we simply present the results of pixelated algorithm testing on single Gaussians and non-overlapping double Gaussian source profiles. These figures have been discussed in detail in section 4.5, Chapter 4.

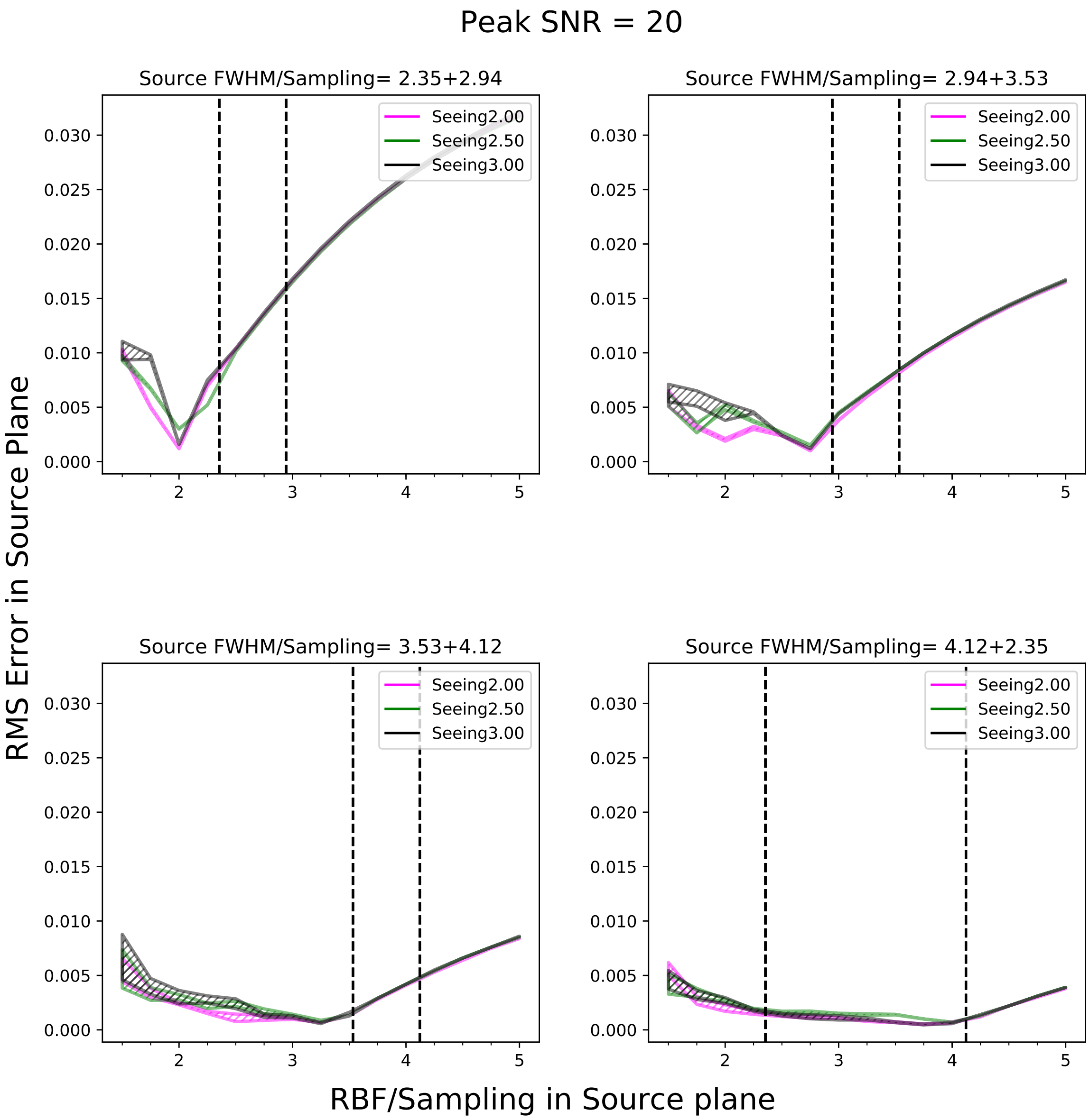

Figure B.1 Source-plane RMS error as a function of RBF widths for single Gaussian source models for a fixed peak SNR of 20 in the image plane. Different colors represent trends for different values of FWHM of Gaussian PSF i.e. (2.0, 2.5, 3.0) × image pixel size. Shaded regions show 1 σ error bars in the RMS error calculated by repeating a single simulation 20 times. Dashed vertical lines show values of FWHM of member gaussians in every source model.

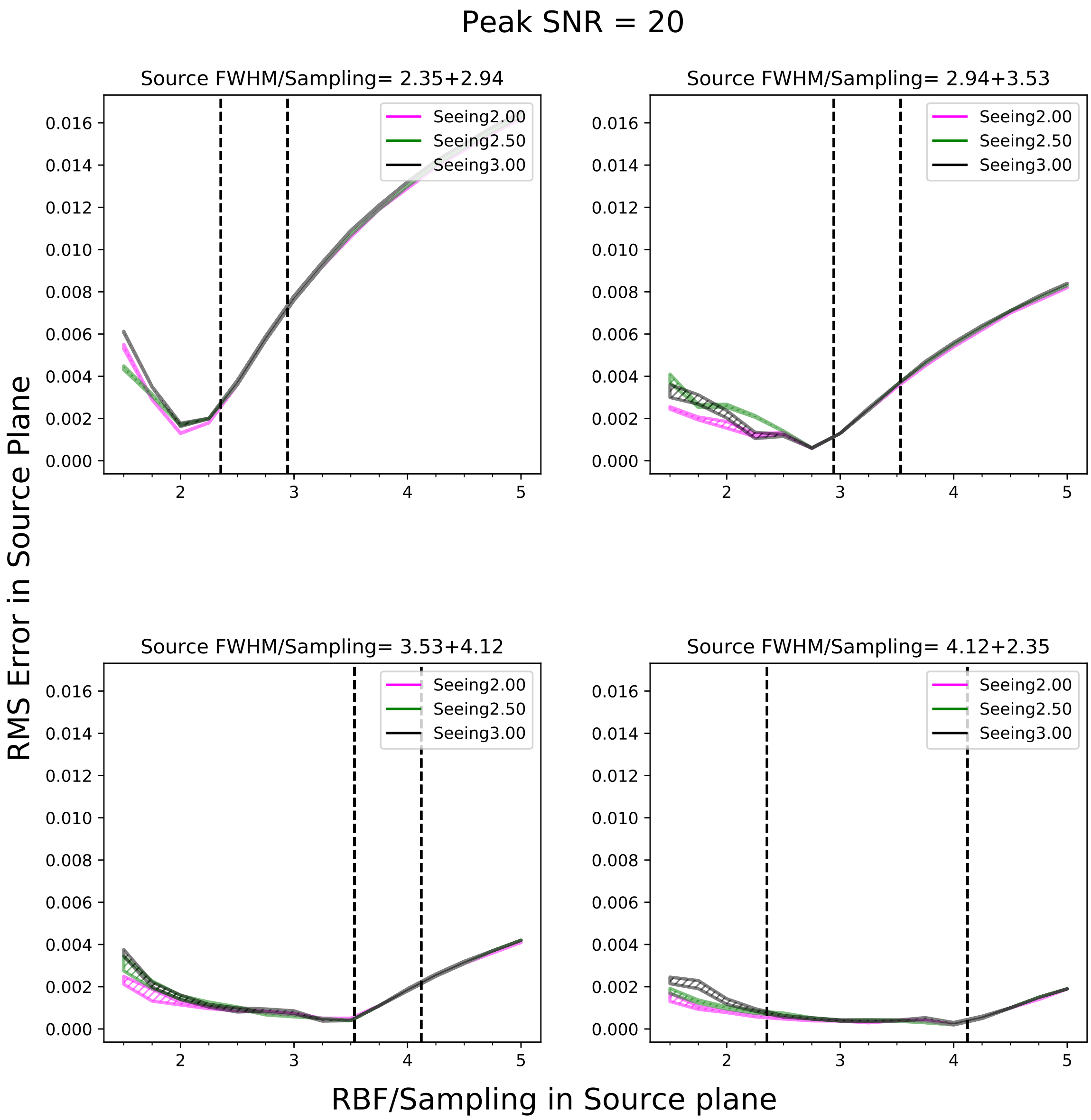

Figure B.2 Source-plane RMS error as a function of RBF widths for non-overlapping double Gaussian source models for a fixed peak SNR of 20 in the image plane. Different colors represent trends for different values of FWHM of Gaussian PSF i.e. (2.0, 2.5, 3.0) $\times$ image pixel size. Shaded regions show 1 σ error bars in the RMS error calculated by repeating a single simulation 20 times. Dashed vertical lines show values of FWHM of member gaussians in every source model.

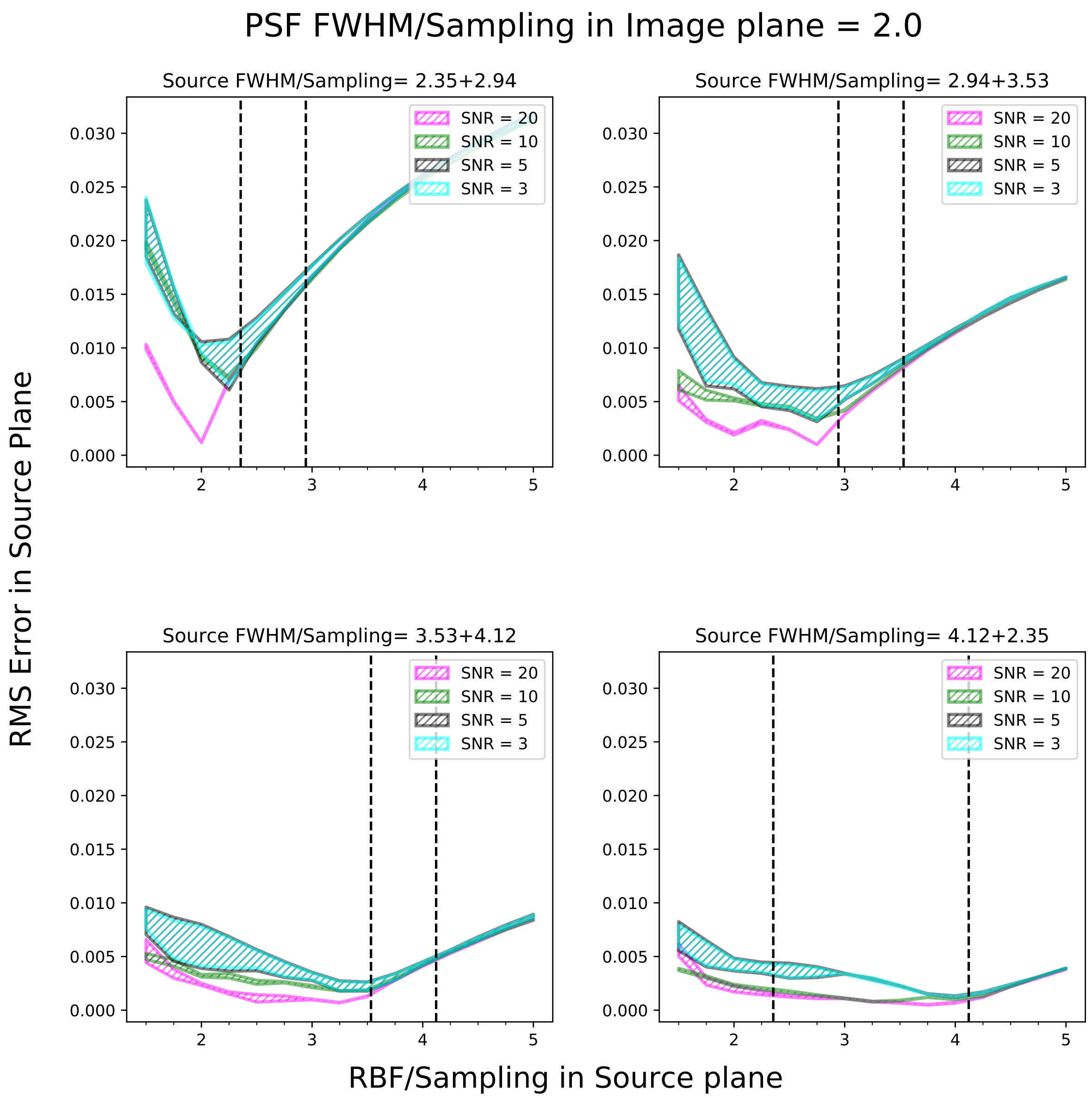

Figure B.3 Source-plane RMS error as a function of RBF widths for single Gaussian source models for a fixed ratio of PSF FWHM / Image plane sampling = 2.0. Different colors represent trends for different values of peak SNR i.e. (20, 10, 5, 3) in the image plane. Shaded regions show 1 σ error bars in the RMS error calculated by repeating a single simulation 20 times. Dashed vertical lines show values of FWHM of member gaussians in every source model.

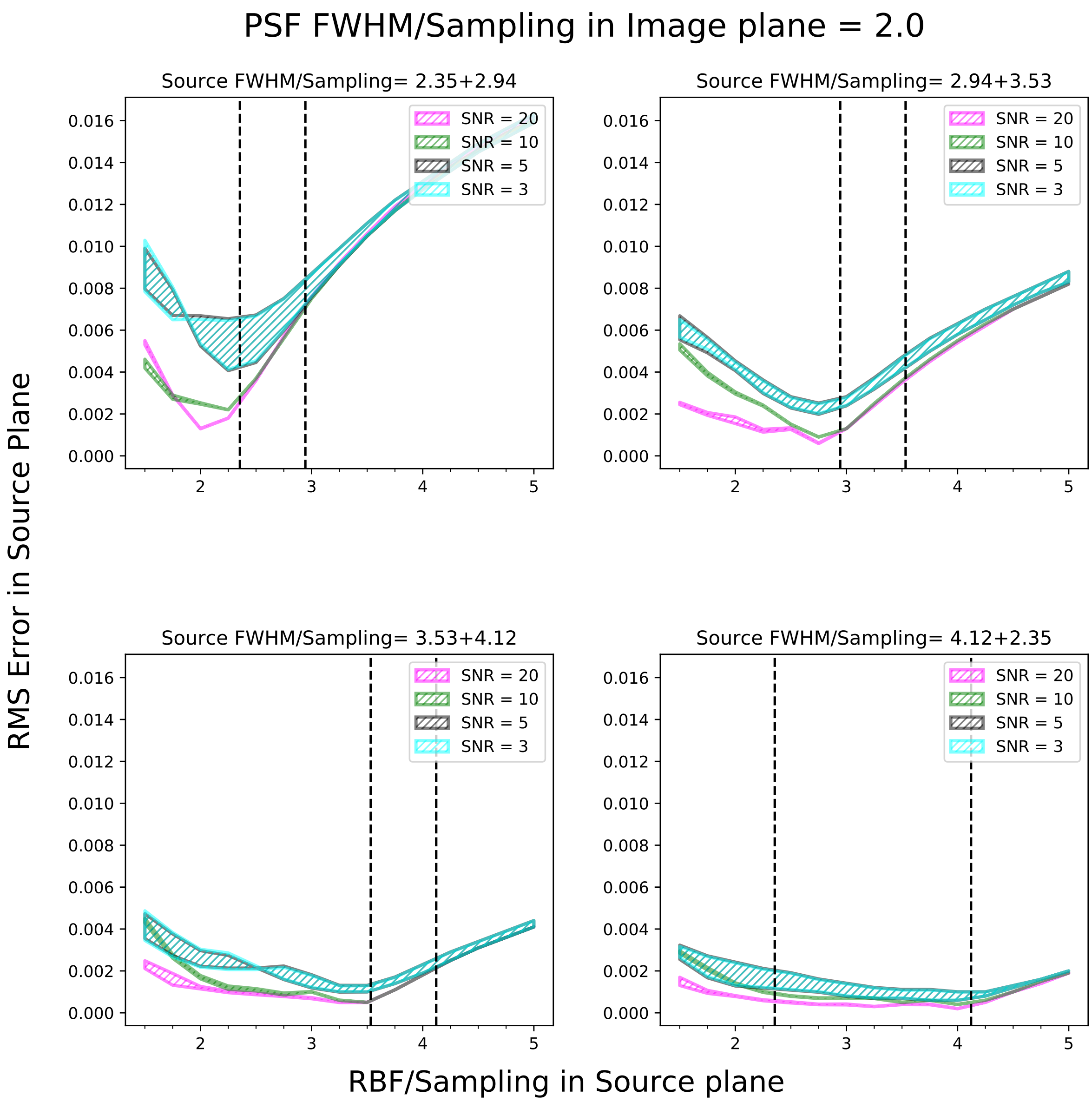

Figure B.4 Source-plane RMS error as a function of RBF widths for non-overlapping double Gaussian source models for a fixed ratio of PSF FWHM / Image plane sampling = 2.0. Different colors represent trends for different values of peak SNR i.e. (20, 10, 5, 3) in the image plane. Shaded regions show 1 σ error bars in the RMS error calculated by repeating a single simulation 20 times. Dashed vertical lines show values of FWHM of member gaussians in every source model.

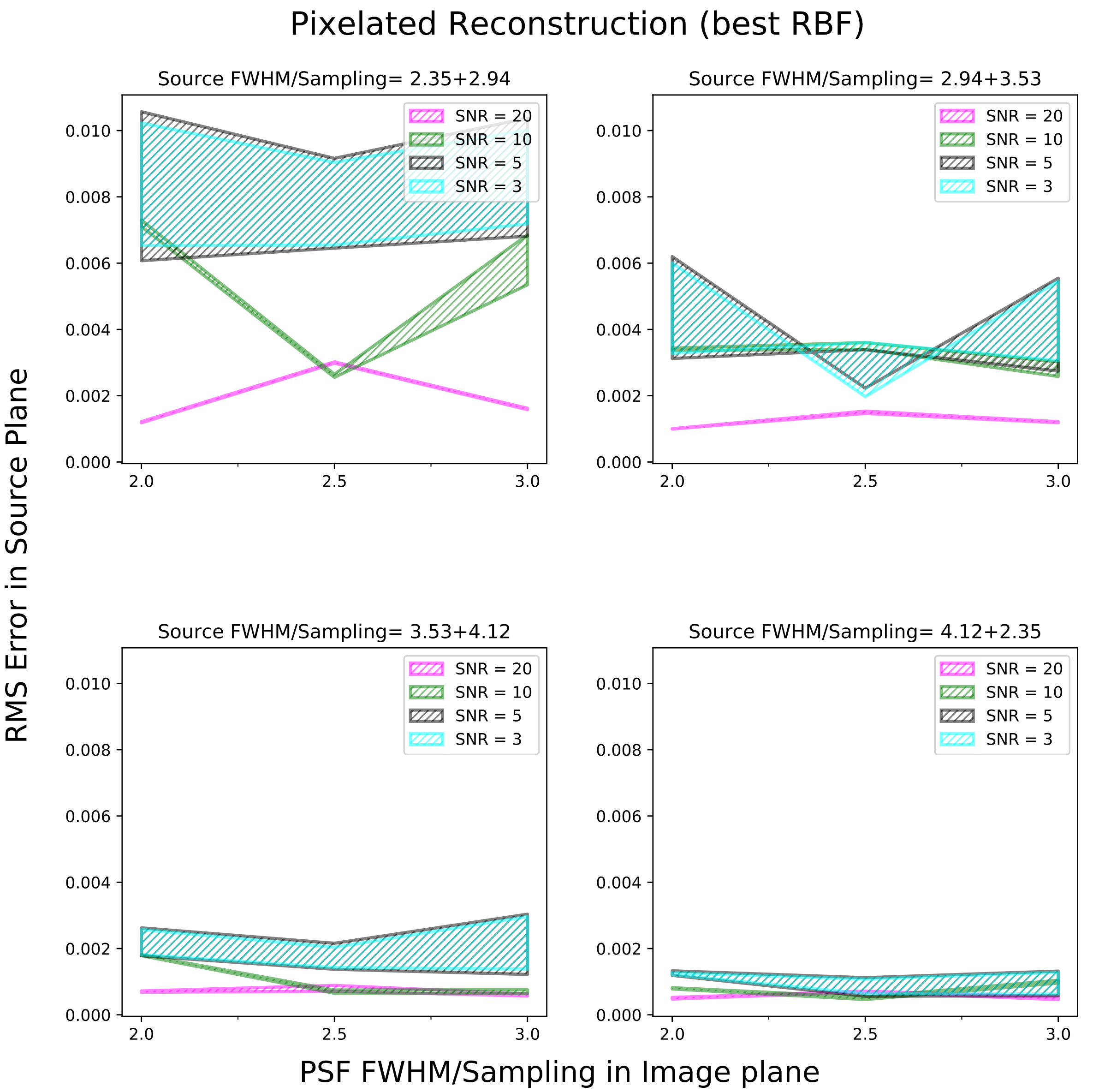

Figure B.5 Source-plane RMS error computed on single Gaussian source profiles reconstructed with pixelated modelling technique as a function of the ratio of PSF FWHM to image plane sampling at the "best" RBF size. FWHM of "best" Gaussian RBF for every test case is chosen such that the image plane $\chi2$ for that RBF value is minimum during Bayesian optimization. Different colors represent trends for different values of Peak SNR in the image plane. Shaded regions show 1 σ error bars in the source plane RMS error calculated by repeating a single simulation 20 times.

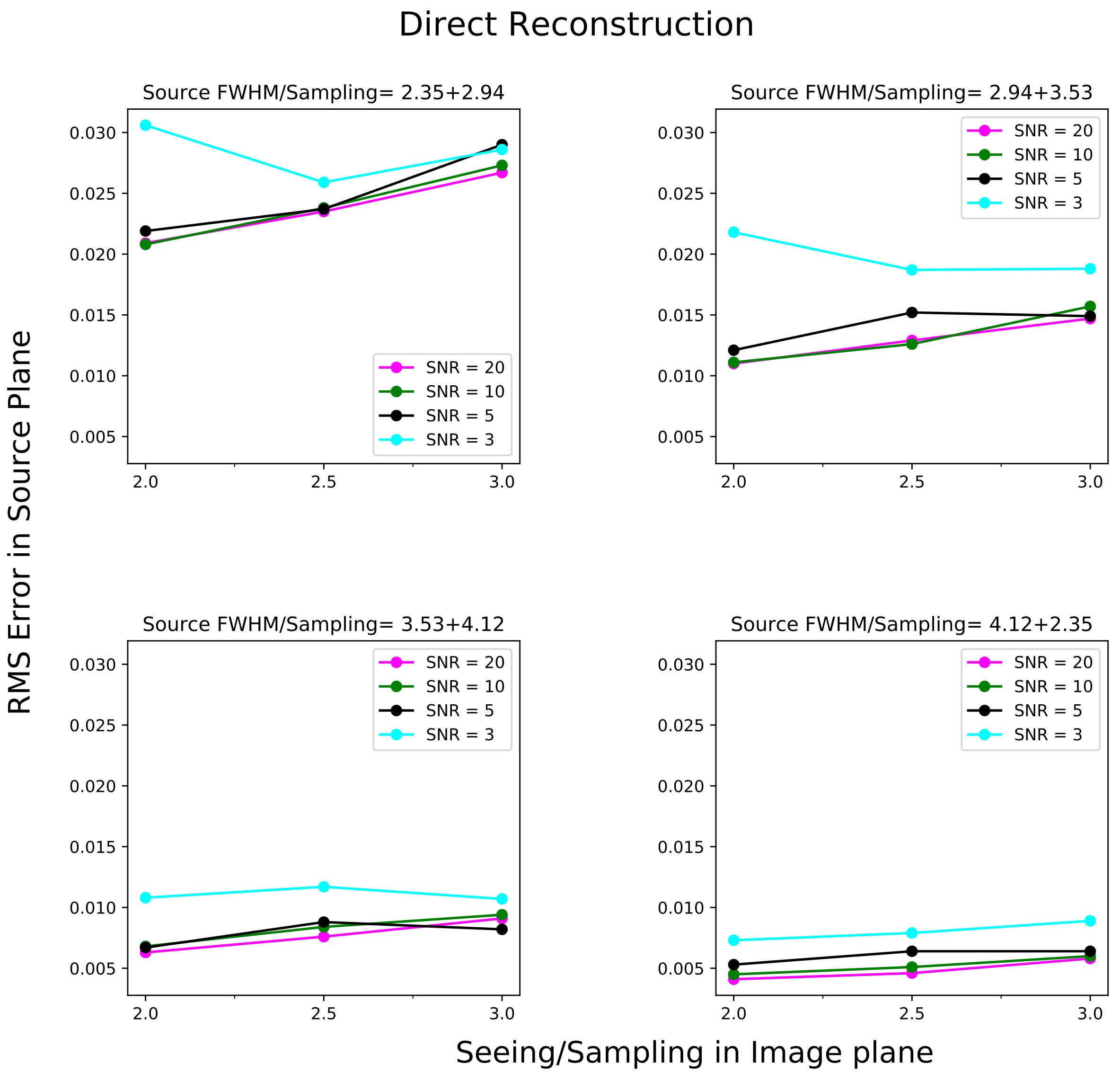

Figure B.6 Source-plane RMS error computed on single Gaussian source profiles reconstructed with direct ray-tracing as a function of the ratio of PSF FWHM to image plane sampling. Different colors represent trends for different values of Peak SNR in the image plane.

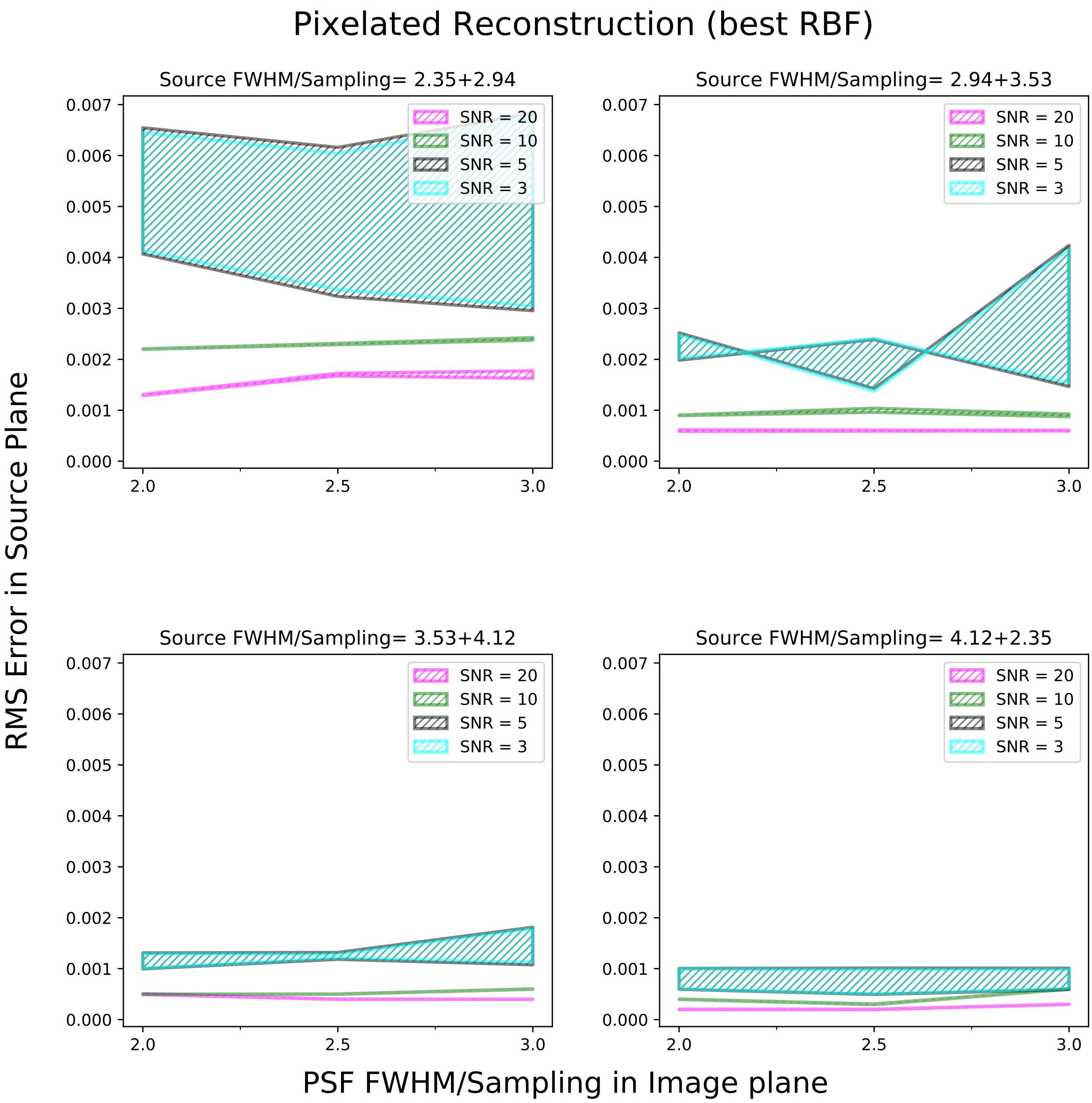

Figure B.7 Source-plane RMS error computed on non-overlapping double Gaussian source profiles reconstructed with pixelated modelling technique as a function of the ratio of PSF FWHM to image plane sampling at the "best" RBF size. FWHM of "best" Gaussian RBF for every test case is chosen such that the image plane $\chi 2$ for that RBF value is minimum during Bayesian optimization. Different colors represent trends for different values of Peak SNR in the image plane. Shaded regions show 1 σ error bars in the source plane RMS error calculated by repeating a single simulation 20 times.

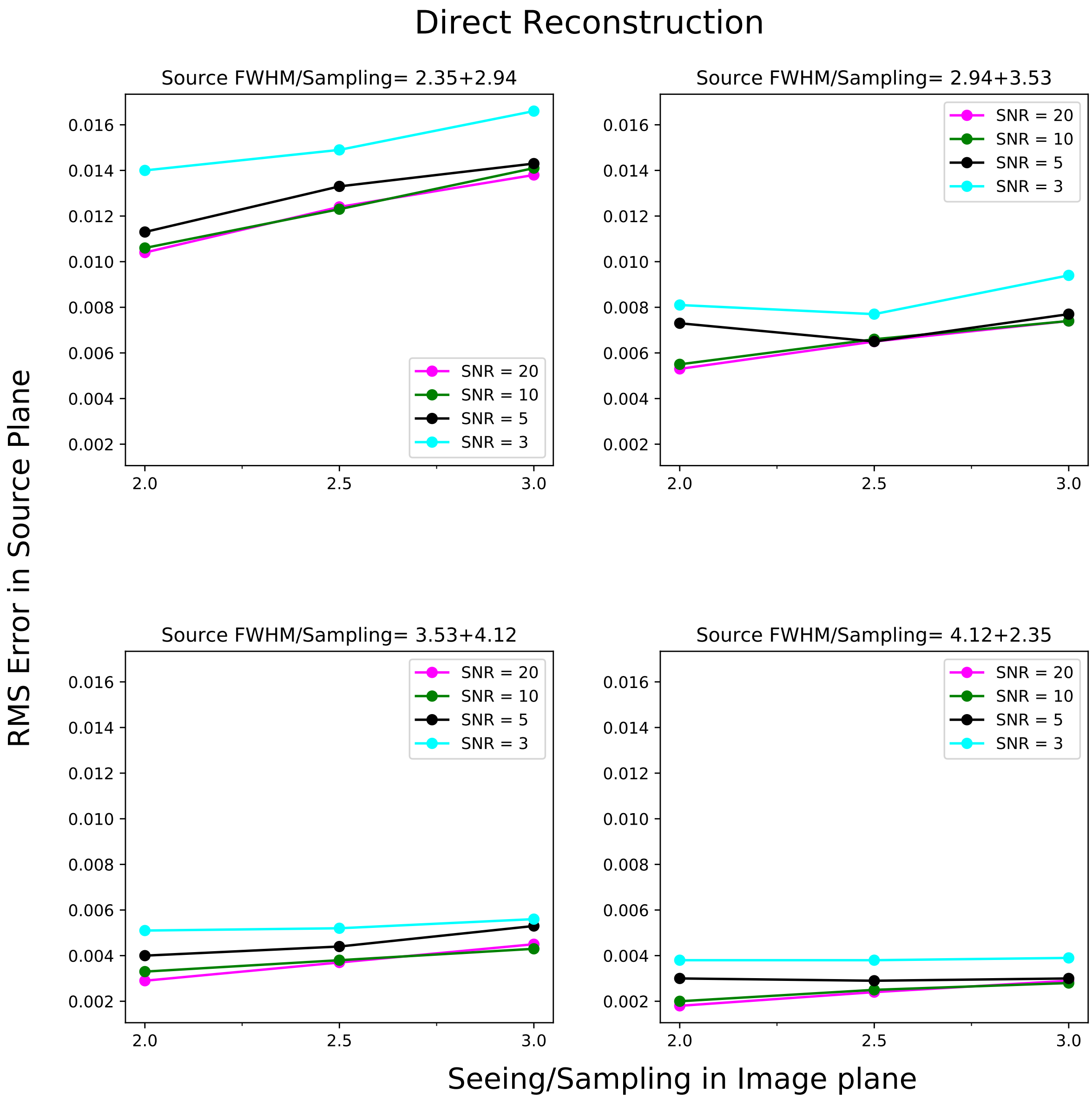

Figure B.8 Source-plane RMS error computed on non-overlapping double Gaussian source profiles reconstructed with direct ray-tracing as a function of the ratio of PSF FWHM to image plane sampling. Different colors represent trends for different values of Peak SNR in the image plane..